

**Geometric, Electronic and Optical Properties of Organic Charge Transfer
Systems: Photovoltaic Blends and Donor-Acceptor Co-crystals**

A Dissertation
Presented to
The Academic Faculty

by

Ajith Ashokan

In Partial Fulfillment
of the Requirements for the Degree
Doctor of Philosophy in the
School of Chemistry and Biochemistry

Georgia Institute of Technology
May 2020

COPYRIGHT © 2020 BY AJITH ASHOKAN

**Geometric, Electronic and Optical Properties of Organic Charge Transfer
Systems: Photovoltaic Blends and Donor-Acceptor Co-crystals**

Approved by:

Dr. Jean-Luc Brédas, Advisor
School of Chemistry and Biochemistry
Georgia Institute of Technology

Dr. Elsa Reichmanis
School of Chemical and Biomolecular
Engineering
Georgia Institute of Technology

Dr. David Sherrill
School of Chemistry and Biochemistry
Georgia Institute of Technology

Dr. Carlos Silva
School of Physics
Georgia Institute of Technology

Dr. John Reynolds
School of Chemistry and Biochemistry
Georgia Institute of Technology

Date Approved: [11/25/2019]

This Thesis is dedicated to my dear wife

Divya Vijay Kumar

without whose love, support, belief and encouragement

none of this would have been possible.

ACKNOWLEDGEMENTS

First and foremost, I would like to thank my Ph.D. advisor, Prof. Jean-Luc Brédas for his gracious support, guidance and mentorship over the last 5 years. He has been a role model for me on both personal and professional fronts. I am deeply indebted to Prof. Brédas for accepting me into his group at KAUST, and then at Georgia Tech, giving me a chance to pursue my dreams.

I would like to thank the distinguished academics who agreed to be on my Ph.D. defense committee members and for their guidance and valuable advice: Prof. C. David Sherrill, Prof. John Reynolds, Prof. Elsa Reichmanis and Prof. Carlos Silva.

I would like to express my deepest admiration for the group of talented individuals, my colleagues at the Brédas research group; professional journey with them was enjoyed and cherished every moment. I would like to especially thank Dr. Tonghui Wang and Dr. Veaceslav Coropceanu, two outstanding individuals who were like co-mentors to me for the last 3 years. I have always revered the technical knowledge, clarity of thoughts and the passion for research of these two distinguished colleagues. I have learned a lot from you both.

I appreciate the company of good friends who were also my colleagues at KAUST and Georgia Tech. Dr. Simil Thomas and Dr. Mahesh Kumar Ravva, two of my good friends with whom I started my research journey at KAUST. I thank you both for all the help given to me to acquire technical skills in computational chemistry. I gratefully acknowledge the friendship with Dr. Saju Joseph, Dr. Pralok Kumar Samantha, Dr. Ajitha Manjaly John, Mrs. Seema Pralok, Mrs. Anita Mahesh, and Dr. Sony Saju at KAUST, a group of individuals because of whom I never felt away from home while in Saudi Arabia. I will always cherish all those wonderful days spent together.

I would like to thank my chemistry teacher Smt. Mini. K. Nair, at P.E.S. Vidyalaya, Payyanur for implanting the passion for Chemistry that I have today. I will always remember you with admiration for your constant support and encouragement during school days.

I would like to thank and express my deepest admiration for my teacher at Govt. Brennen College, Thalasseri, Prof. P. N. Sathyanathan, for his guidance, constant support, belief in my abilities and encouragement to pursue research. Your inspiring words and blessings give me strength to work towards my goal even to this day. Also, I gratefully acknowledge my teachers at Govt. Brennen College: Prof. P. Govindan, Prof. Prameela, and (Late) Prof. Prabhakaran.

Finally, I express my deepest gratitude and appreciation for the love and support my family gave in this endeavor. To my parents, Mrs. P.M. Vijayalakshmi and Mr. P.K. Ashokan, for giving me the wings to pursue my dream. You gave us the best of everything, and I would be eternally grateful to both of you. To my brother Mr. Arjun Ashokan, for your love and companionship all these years. To my wife's parents, Smt. Geetha. V and Mr. Kesavan Vijay Kumar, for your love, belief and support. To my sister-in-law, Mrs. Dhanya. V and brother-law Mr. J. Joshiva, for your love and support. To my grandparents (Late) Sri. Govindan and (Late) Smt. Sreedevi Amma, I miss you both so much. Above all, to my dear wife, Mrs. Divya Vijay Kumar for always being there, for your love, generosity, understanding, support and constant encouragement, without which none of this would have been possible.

TABLE OF CONTENTS

ACKNOWLEDGEMENTS	iv
LIST OF TABLES	ix
LIST OF FIGURES	xii
LIST OF SYMBOLS AND ABBREVIATIONS	xvi
SUMMARY	xix
CHAPTER 1. INTRODUCTION	1
1.1. Overview	1
1.2. Motivation	3
1.2.1. The need for Organic Photovoltaics	3
1.2.2. OFET's	6
1.3. Materials and their combinations for organic electronic devices	7
1.4. Key processes in OPV and OFET devices	12
1.5. Morphology, its impact on transport parameters and disorder	14
1.6. Thesis objective and outline	17
1.7. References	19
CHAPTER 2. THEORETICAL METHODOLOGY	23
2.1. Introduction	23
2.2. The Schrödinger Equation	23
2.2.1. Hartree-Fock Theory	25
2.2.2. Density Functional Theory	28
2.2.2.1. The Hohenberg-Kohn Theorems	28
2.2.2.2. Kohn-Sham Theory	29
2.2.2.3. Approximate exchange-correlation functionals	31
2.2.2.3.1. Local density approximation	31
2.2.2.3.2. Generalized Gradient Approximations	32
2.2.2.3.3. Hybrid functionals	32
2.2.2.3.4. Long-range corrected functionals	33
2.2.2.4. Non-empirical tuning of the range-separated functionals	34
2.2.2.5. Band Structure and Tight-Binding Model	35
2.2.2.6. Effective Masses	37
2.2.2.7. Transfer Integrals	38
2.3. Atomistic Molecular Dynamics	40
2.3.1. Force fields	41
2.3.2. Performing MD simulations	42
2.4. Codes Used	43
2.5. References	44

CHAPTER 3. IMPACT OF SOLUTION TEMPERATURE-DEPENDENT AGGREGATION ON THE SOLID-STATE PACKING AND ELECTRONIC PROPERTIES OF POLYMERS FOR ORGANIC PHOTOVOLTAICS 46

3.1.	Introduction	46
3.2.	Methodology	49
3.2.1.	Molecular Dynamics Simulations	49
3.2.2.	Density Functional Theory Calculations	51
3.3.	Results and Discussion	51
3.3.1.	Morphology of the Polymers in Solution	51
3.3.2.	Distribution of Dihedral Angles along the Polymer Chains and Assessment of Co-Planarity.	55
3.3.3.	Interaction Energies and Their Effect on Morphology	64
3.3.4.	Electronic coupling	66
3.4.	Conclusions	69
3.5.	References	70

CHAPTER 4. BULK-HETEROJUNCTION SOLAR CELLS: UNDERSTANDING THE INTERMOLECULAR PACKING AND ELECTRONIC PROPERTIES IN POLYMER-SMALL-MOLECULE ACCEPTOR BLENDS 73

4.1.	Introduction	73
4.2.	Methodology	77
4.2.1.	Molecular Dynamics Simulations	77
4.2.2.	Density Functional Theory Calculations	78
4.3.	Results and Discussion	79
4.3.1.	Intermolecular packing and interactions	79
4.3.2.	Intermolecular packing patterns	81
4.3.3.	Intermolecular electron-transfer rates among adjacent SMAs	87
4.3.4.	Interfacial charge-transfer states and non-radiative recombination rates	89
4.4.	Conclusions	93
4.5.	References	95

CHAPTER 5. ELECTRONIC AND CHARGE-TRANSPORT PROPERTIES OF F₆TNAP-BASED CHARGE-TRANSFER COCRYSTALS 99

5.1.	Introduction	99
5.2.	Methodology	102
5.2.1.	Density Functional Theory Calculations	102
5.2.2.	Experimental	105
5.3.	Results and Discussion	106
5.3.1.	Electronic structure, Band-Structure, and Electronic Couplings	106
5.3.2.	Electrical properties	114
5.3.3.	Degree of charge transfer	118
5.4.	Conclusions	122

5.5. References	123
------------------------	------------

CHAPTER 6. ELECTRONIC, VIBRATIONAL AND CHARGE-TRANSPORT PROPERTIES OF di-C_nBTBT-F_mTCNQ CO-CRYSTALS: IMPACT OF ALKYL CHAINS AND FLUORINATION **127**

6.1. Introduction	127
6.2. Methodology	129
6.3. Results and Discussion	131
6.3.1. Electronic Structure and Electronic Couplings	131
6.3.2. Superexchange Couplings: Electron hole Asymmetry	140
6.3.3. Low-energy CT Optical Transitions	143
6.3.4. Degree of charge transfer	147
6.4. Conclusions	150
6.5. References	152

CHAPTER 7. CONCLUSIONS AND OUTLOOK **154**

7.1. Organic Photovoltaics	155
7.2. Organic CT Co-crystals	158

APPENDIX A. LIST OF PUBLICATIONS **161**

LIST OF TABLES

	Page
Table 3.1. Binding energies between two perfectly stacked dimer units, as calculated at the ω B97XD/6-31G** level of theory.	64
Table 3.2. Binding energies between two adjacent polymer chains, as calculated at the ω B97XD/6-31G** level of theory.	65
Table 4.1. Average interaction energies (and their standard deviations) among PTFB-O, ITIC-Th, and IEIC-Th pairs and dimers.	81
Table 4.2. Average interaction energies (and their standard deviations) for PTFB-O- A /SMA- A and PTFB-O- D /SMA- A pairs extracted from the MD-simulated PTFB-O:ITIC-Th and PTFB-O:IEIC-Th blends.	85
Table 4.3. Average electronic couplings (V_{L-L}) and the standard deviations between the LUMOs of SMA/SMA dimers extracted from the MD-simulated PTFB-O:ITIC-Th and PTFB-O:IEIC-Th blends.	87
Table 4.4. Proportions of SMA/SMA dimers corresponding to different orders of magnitude in electron-transfer rates and experimentally measured electron mobilities for the blends of PTFB-O:ITIC-Th and PTFB-O:IEIC-Th.	89
Table 4.5. Standard deviations of the energetic distributions of the CT states, corresponding to total, dynamic, and static disorders for the PTFB-O:ITIC-Th and PTFB-O:IEIC-Th blends.	91
Table 4.6. Average CT-state energy; standard deviation; V_{OC} loss due to interfacial disorder; effective CT-state energy, and experimentally measured V_{OC} , for the cases of PTFB-O:ITIC-Th and PTFB-O:IEIC-Th.	93
Table 5.1. Electrochemical potentials (as measured in the Marder group) and B3LYP/6-31G-calculated orbital energies, adiabatic	106

ionization energy (IE) and electron affinity values (EA) for the donor and acceptor molecules.

Table 5.2.	B3LYP/6-31G conduction and valence bandwidths (in meV) along with the lowest two effective masses	108
Table 5.3.	B3LYP/6-31G estimates of ΔE_{DA} , t_{DA} , and super-exchange couplings for holes and electrons.	109
Table 5.4.	Hole and electron effective masses, m (in units of the free electron mass at rest, m_0).	113
Table 5.5.	Summary of the electrical properties evaluated from the SCLC and OFET measurements conducted in the Jurchescu group.	116
Table 5.6.	Highest nitrile stretching frequencies (cm^{-1}) for F_6TNAP , cocrystals, and $\text{F}_6\text{TNAP}^{\bullet-}$, ν_0 , ν_{CT} , and ν_1 , respectively, and along with estimated degree of charge transfer (ρ) for cocrystals.	119
Table 5.7.	Degree of charge transfer in the co-crystals based on Mulliken charges.	121
Table 6.1.	B3LYP/6-31G (d, p) conduction and valence bandwidths (in meV) along with the lowest two effective masses (in units of electron mass in vacuum, m_0).	134
Table 6.2.	Hole and electron effective masses, m (in units of the free electron mass at rest, m_0).	138
Table 6.3.	B3LYP/6-31G (d,p) estimates of t_{AA} , t_{DD} , and t_{DA} , and super-exchange couplings for holes (t_h^{eff}) and electrons (t_e^{eff}).	139
Table 6.4.	B3LYP/6-31G (d,p) estimates of $t_{(H)D-(L)A}$ (meV) and $t_{(H-1)D-LA}$.	143
Table 6.5.	Singlet excited-state energies of co-crystals calculated by TDDFT at the B3LYP/6-31G(d,p) level.	144

Table 6.6. Degree of charge transfer in the co-crystals based on Mulliken charges.

150

LIST OF FIGURES

	Page	
Figure 1.1	Illustration of the chemical structures of representative small-molecule semiconductors.	7
Figure 1.2	Illustration of the chemical structures of representative polymers functioning as p-type semiconductors.	8
Figure 1.3.	Illustration of the chemical structures of representative acceptor molecules functioning as n-type semiconductors.	9
Figure 3.1.	Illustration of the chemical structures of the PBT4T-2OD and PffBT4T-2OD polymers with their chemical differences highlighted in blue and red.	48
Figure 3.2.	Illustration of the representative initial model used for the MD simulations.	50
Figure 3.3.	Snapshots from the MD simulations showing the extent of disaggregation of the six polymer chains present in the simulation box.	54
Figure 3.4.	Illustration of the three dihedrals considered to analyze the distribution of dihedral angles.	56
Figure 3.5.	Distribution of the dihedral angles along the PBT4T-2OD and PffBT4T-2OD chains after MD simulations of the respective polymer stacks in solution at 25°C.	57
Figure 3.6.	Distribution of the dihedral angles along the PBT4T-2OD and PffBT4T-2OD chains after MD simulations of the respective polymer stacks in solution at 40°C.	58
Figure 3.7.	Distribution of the dihedral angles along the PBT4T-2OD and PffBT4T-2OD chains after MD simulations of the respective polymer stacks in solution at 60°C.	59
Figure 3.8.	Distribution of the dihedral angles along the PBT4T-2OD and PffBT4T-2OD chains after MD simulations of the respective polymer stacks in solution at 80°C.	60

Figure 3.9.	Distribution of the dihedral angles along the PBT4T-2OD and PffBT4T-2OD chains after MD simulations of the respective polymer stacks in solution at 100°C.	61
Figure 3.10.	Distribution of dihedral angles along the PBT4T-2OD and PffBT4T-2OD chains after MD simulations of single polymer chains in o-DCB solution at 25°C.	63
Figure 3.11.	HOMOs of PBT4T-2OD and PffBT4T-2OD, as calculated at the ω B97XD/6-31G** level of theory.	66
Figure 3.12.	Illustration of (a) the cut of a polymer chain with six repeat units into segments of two repeat units each, (b) the protocol for the calculation of the electronic couplings between adjacent chains.	67
Figure 3.13.	Electronic couplings between segments of the PBT4T-2OD and PffBT4T-2OD chains at 25°C, 40°C, 60°C and 80°C.	68
Figure 4.1.	Chemical structures of PTFB-O, ITIC-Th, and IEIC-Th. The groups circled in red represents the electron-poor (A) moiety and those circled in blue represents the electron-rich (D) moiety.	76
Figure 4.2.	Radial distribution functions between PTFB-O backbones and SMAs in the PTFB-O:ITIC-Th and PTFB-O:IEIC-Th blends.	80
Figure 4.3.	RDFs for: (a) interaction between the PTFB-O polymer backbone and the D moiety or A moiety of ITIC-Th acceptors, (b) interaction between the PTFB-O polymer backbone and the D moiety or A moiety of IEIC-Th acceptors.	82
Figure 4.4.	RDFs for: (a) interactions between the D moiety or A moiety of PTFB-O polymer and the A moiety of ITIC-Th acceptor, (b) interactions between D moiety or A moiety of PTFB-O polymer and the A moiety of IEIC-Th acceptor	84
Figure 4.5.	RDFs for the SMA- D /SMA- D , SMA- D /SMA- A , and SMA- A /SMA- A interactions in (a) PTFB-O:ITIC-Th and (b) PTFB-O:IEIC-Th.	86
Figure 4.6.	Distributions for the electronic couplings between the LUMOs of SMAs all the SMA/SMA dimers extracted from the MD-simulated PTFB-O:ITIC-Th and PTFB-O:IEIC-Th blends.	88

Figure 4.7.	Energetic distribution of the CT states in MD-simulated blends of PTFB-O:ITIC-Th and PTFB-O:IEIC-Th.	90
Figure 4.8.	Non-radiative recombination rates as a function of the quantum component of reorganization energy.	92
Figure 5.1.	Chemical structures of the F ₆ TNAP acceptor and the TP, BTBT, BDT, PY, ANT, and CBZ donors.	101
Figure 5.2.	Illustration of the energy-splitting estimates of the transfer integrals along the stacking direction for (a) holes and (b) electrons of Pentacene dimer and (c) holes and (d) electrons of DMQ _t T-F ₄ TCNQ co-crystal.	103
Figure 5.3.	Electronic band structure and density of states of the (a) TP:F ₆ TNAP, (b) BTBT:F ₆ TNAP, (c) BDT:F ₆ TNAP, (d) PY:F ₆ TNAP, (e) ANT:F ₆ TNAP, and (f) CBZ:F ₆ TNAP co-crystals.	107
Figure 5.4.	Illustrations of the largest transfer integrals and smallest effective masses for holes and electrons in: (a) TP:F ₆ TNAP, (b) BTBT:F ₆ TNAP, (c) BDT:F ₆ TNAP, (d) PY:F ₆ TNAP; (e) ANT:F ₆ TNAP, and (f) CBZ:F ₆ TNAP.	111-112
Figure 5.5.	SCLC measurements for the representative examples of the (a) BTBT:F ₆ TNAP and (b) CBZ:F ₆ TNAP co-crystals.	115
Figure 5.6.	Evolution of the drain current, I _D as a function of gate-source voltage, V _{GS} (a) at V _{DS} = -60 V, and (b) V _{DS} = 60 V for ANT:F ₆ TNAP and (c) at V _{DS} = -70 V, and (d) V _{DS} = 70 V for PY:F ₆ TNAP. Measurements conducted in the Jurschescu group.	117
Figure 5.7.	IR spectra comparing the nitrile stretching modes of F ₆ TNAP with (a) TP:F ₆ TNAP, BTBT:F ₆ TNAP, ANT:F ₆ TNAP, PY:F ₆ TNAP cocrystals, and (b) CBZ:F ₆ TNAP. Measurements conducted in the Marder group.	118
Figure 5.8.	DFT simulated (IR) vibrational frequencies comparing the C≡N stretching modes of F ₆ TNAP in the charge-transfer complexes, as calculated at the B3LYP/6-31G level.	120
Figure 6.1.	Chemical structures of the BTBT (n=0, R=H), di-C ₈ BTBT (n=8, R=C ₈ H ₁₇), and di-C ₁₂ BTBT (n=12, R=C ₁₂ H ₂₅) donors as well as the TCNQ, F ₂ TCNQ, and F ₄ TCNQ acceptor molecules.	129

Figure 6.2.	Crystal structures of (a) BTBT-TCNQ, (b) BTBT-F ₂ TCNQ, (c) BTBT-F ₄ TCNQ, (d) di-C ₈ BTBT-TCNQ, (e) di-C ₈ BTBT-F ₄ TCNQ, (f) di-C ₁₂ BTBT-TCNQ, and (g) di-C ₁₂ BTBT-F ₄ TCNQ.	132-133
Figure 6.3.	Electronic band structures and densities of states of the: (a) BTBT:TCNQ, (b) BTBT:F ₂ TCNQ, (c) BTBT:F ₄ TCNQ, (d) di-C ₈ BTBT:TCNQ, (e) di-C ₈ BTBT:F ₄ TCNQ, (f) di-C ₁₂ BTBT:TCNQ, and (g) di-C ₁₂ BTBT:F ₄ TCNQ crystals.	135-136
Figure 6.4.	Electronic band structures and densities of states of the: (a) DMQtT:F ₄ TCNQ and (b) DBTTF:F ₄ TCNQ co-crystals.	140
Figure 6.5.	Energy levels of BTBT, TCNQ, F ₂ TCNQ, and F ₄ TCNQ calculated at the B3LYP/6-31G(d, p) level.	142
Figure 6.6.	Natural Transition Orbitals for the lowest excited states calculated at the TDDFT B3LYP/6-31G (d, p) level.	144-146
Figure 6.7.	B3LYP/6-31G (d, p) IR vibrational frequencies comparing: (a) the charge sensitive bands in the 1200-1700 cm ⁻¹ region, and, (b) the C≡N stretching modes of F _m TCNQ (m=0, 2, 4) in the charge-transfer complexes.	148

LIST OF SYMBOLS AND ABBREVIATIONS

OPV	Organic Photovoltaics
OFET	Organic Field-Effect Transistors
OLED	Organic Light Emitting Diode
PCE	Power Conversion Efficiency
PV	Photovoltaics
TFT	Thin Film Transistor
BHJ	Bulk-Heterojunction
NFA	Non-Fullerene Acceptor
NIR	Near-InfraRed
IE	Ionization Energy
EA	Electron Affinity
CT	Charge-Transfer
AFM	Atomic Force Microscopy
GIWAXS	Grazing-Incidence Wide-Angle X-Ray Scattering
DSC	Differential Scanning Calorimetry
TEM	Transmission Electron Microscopy
XRD	X-Ray Diffraction
CV	Cyclic Voltammetry
CG	Coarse-Grained
MD	Molecular Dynamics
RDF or $g(r)$	Radial Distribution Function
DFT	Density Functional Theory

HF	Hartree Fock
SCF	Self-Consistent Field
LCAO	Linear Combination of Atomic Orbitals
LDA	Local Density Approximation
XC	Exchange-Correlation
GGA	Generalized Gradient Approximation
LYP	Lee, Yang and Par
HOMO	Highest Occupied Molecular Orbital
LUMO	Lowest Unoccupied Molecular Orbital
OPLS-AA	Optimized Potential for Liquid Simulations- All Atom
TDA	Temperature-dependent Aggregation
OSC	Organic Solar Cells
SMA	Small Molecule Acceptors
PPPM	Particle Particle Particle Mesh
BSSE	Basis-set Superposition Error
TD-DFT	Time-dependent Density Functional Theory
PCM	Polarizable Continuum Model
V _{oc}	Open-Circuit Voltage
J _{sc}	Short-Circuit Current
SCXRD	Single Crystal X-Ray Diffraction
SCLC	Space-Charge Limited Current
CCDC	Cambridge Crystallographic Data Center
CB	Conduction Band
VB	Valence Band
t^{eff}	Effective Electronic Coupling

m_0	Rest electron mass in vacuum
μ	Charge-carrier mobility
NTO	Natural Transition Orbital
IR	Infra-Red
FF	Fill Factor
KMC	Kinetic Monte Carlo
NPT	Constant Number of atoms, pressure and temperature
B3LYP	Becke 3-Parameter, Lee-Yang-Parr Hybrid Functional
ω B97X-D	Long-Range Corrected Hybrid Functional with Becke97 Exchange-Correlation Functional and Grimme's D2 Dispersion Model

SUMMARY

Over the past two decades, π -conjugated organic molecules have found applications in the active layer of different types of organic electronic devices. To optimize and improve the performance of each of these devices, it is important to establish clear connections between chemical-structure, intermolecular packing and their impact on the electronic and charge transport properties in these systems. In this Thesis, we focus on two-component organic material systems – one acting as a π -electron donor (D) and the other as a π -electron acceptor (A) for applications in organic photovoltaics (OPV) and organic field-effect transistors (OFETs).

On the OPV side (Chapters 3 & 4), initially, we investigate the solution temperature-dependent aggregation property of a few polymers in their pure phases, which has been recently established as a potential method for morphology control in high-performing OSC devices. We then explore the intermolecular packing properties in the binary blends of polymer and two small molecule acceptors, which in their binary as well as ternary combinations exhibit high power conversion efficiencies. We elucidate clear connections between the molecular scale features that impact the device parameters in both the binary blends. We also obtain useful trends to explain the linear evolution of device parameters in the ternary blends.

On the OFET side (Chapters 5 & 6), our focus is on DA charge-transfer co-crystals, which possess potential applications as active layer components in OFET devices. Initially, we investigate the effect of packing on electronic properties of co-crystals based on F₆TNAP acceptor and a series of donor molecules. Further, we focus on understanding the evolution in electronic, vibrational and charge-transport properties with sequential addition of alkyl chains on the donor and fluorine atoms on the acceptor on co-crystals based on BTBT-F_mTCNQ (m=0, 2, 4) and di-

C_n BTBT- F_m TCNQ ($n=8, 12$; $m=0, 4$) series. Finally, we explore the degree of charge-transfer in these systems using an approach based on Mulliken charges. While these results are limited to the systems under consideration, our simulations provide a reliable, molecular-level understanding to systematically improve the morphological characteristics that impact the device performances in organic electronic devices.

CHAPTER 1

INTRODUCTION

1.1 Overview

The field of organic electronics has registered a remarkable growth over the past two decades. Novel properties of organic materials have invoked extensive research interest to explore its potential applications in multiple areas of electronics. Consequently, consumer electronic products with displays and chemical sensors based on organic materials are available in the market.

With the advent of efficient methods for device fabrication like the “printed electronics” technology, it became clear that semiconducting materials based on inorganic silicon and the like are not the only path forward. To suite a number of requirements in the electronics industry, it is imperative to develop alternative materials with tunable properties. Organic materials display several key advantages including flexibility, chemical tunability and easy solution processing at room temperature.¹⁻⁵ Although conducting polymers were discovered as early as the 1970’s,⁶ efforts to apply these materials for consumer electronics developed mainly from the early 1990’s. We note that an early commercial application of organic polymers was as photoconductors for the xerox industry.⁷⁻⁹

Nowadays, the versatility of organic materials is clearly in display, with applications over a wide range of fields- from energy to electronics, bio-integrated wearable materials to robotics and prosthetics. Efforts are currently in progress to effectively maximize their potential for large-scale consumer applications. It should be borne in mind that organic electronics is not a technology

envisioned to replace inorganic silicon-based electronics. Instead, it is to be seen as a parallel stream of prospects, working next to existing technologies as well as newer materials development initiatives like perovskites and covalent organic frameworks/metal-organic frameworks etc., for novel types of applications.

Recently, notable progress has been made in materials development for three major areas - organic photovoltaics (OPV), organic light-emitting diodes (OLED) and organic field effect transistors (OFET). For instance, as a result of the rapid progress made in the last few years, power conversion efficiencies (PCEs) of laboratory scale OPV devices now reach up to an impressive 16%.¹⁰ In comparison, laboratory scale PV cells made of crystalline silicon exhibit PCEs of the order of slightly higher than 26% for mono-crystalline cells¹¹ and *ca.* 20% for polycrystalline cells,¹² while commercial modules show PCEs in the range 17-21%.^{13, 14} In terms of OLEDs, significant progress has been made since the first efforts of Tang and VanSlyke,¹⁵ resulting in the most successful functional device applications. Consumer electronics giants like Apple, LG, Samsung Corporation etc., have already brought smart watches, televisions and mobile devices based on OLED materials into the market. Also, in the case of OFET's, new and diverse material combinations are now available which exhibits preferential n-type, p-type or ambipolar charge-transport characteristics. The mobility values of the champion devices using organic semiconductors are increasingly surpassing those exhibited by amorphous silicon-based field effect transistors.

These developments were in part facilitated by concerted efforts in the theoretical and experimental understanding of the processes taking place on an atomistic scale and the subsequent

tuning of the characteristics of these materials. However, important developments in material and device stability as well as improvements in efficiencies and device lifetime are still desirable. Thus, further investigations are required to keep improving the properties of these materials and ensure broader commercialization.

With this aim in mind, in this Thesis, we focus on understanding the impact of packing, morphology, and molecular-scale interactions on device performance and on the charge-transport properties of materials used in organic electronic devices. We consider specifically materials applicable to two key areas of organic electronics – organic photovoltaics (OPV) and organic field effect transistors (OFET). In the next section, first we detail our motivation to delve into these two major areas. Next, we discuss the material combinations relevant to the functioning of these devices and provide a brief overview of the major processes taking place in a device architecture along with key loss mechanisms hindering performance. We then summarize our current understanding of the strong connection among morphology, electronic properties and device performance. We also describe the effects of energetic disorder on the charge-transport properties in the active layer. Finally, we explain our rationale to study structure-property relationships and discuss how an improved description of molecular-scale parameters derived from our study can be useful to improving device performance.

1.2 Motivation

1.2.1 The need for Organic Photovoltaics

An increased supply of energy is paramount to keep up the fast pace of development of human life. Over the last century, increased demands due to increasing world population and lifestyle

changes have demanded excessive utilization of carbon-based energy sources like coal, oil and natural gas. Unfortunately, this has resulted in larger concentration of greenhouse gases in the atmosphere leading to significant climate change and global warming. Recent estimates based on the fifth assessment report of the Inter-governmental panel for climate change (IPCC) reveals that industrial activities have raised the atmospheric CO₂ content from 280 parts per million to 407 parts per million over the last 150 years.¹⁶ Moreover, pollution of the atmosphere from various industrial emissions/greenhouse gases and other human activities is shifting climate patterns to an extent dangerous to the existence of human and other forms of life on Earth. Efficient strategies need to be devised to counter the problem of climate change which is affecting the geo-political stability as well as the habitability of planet earth.

In order to curb these destabilizing effects on our environment, efforts are focused to identify and use alternative “clean” sources of energy. This is imperative for two main reasons; (1) to meet the energy needs of the planet and to keep the pace of progress made through technological advancement, and (2) to keep the environment habitable for future generations. With the current global energy requirements reaching tens of terawatt ranges, alternative sources of energy must address the following aspects:

- They should be abundantly available.
- They should be cost-effective and be able to contribute to terawatt capacity requirements.
- They should be a non-polluting source of energy – for the environment and without harmful effects to human or other forms of life.

- They should be easily stored and transformable into multiple forms of energy to meet varied requirements.

Although there exist multiple sources of “clean” energy like wind, hydroelectric power, nuclear power etc., which satisfy one or more of the requirements listed above, solar energy has the potential to fulfill all the requirements. Earth receives more energy from the sun in an hour than it needs to meet its energy requirements for an entire year. In recent years, solar modules are increasingly deployed across the world, and reduces our dependency on carbon-based sources for energy. Currently, 2.6% of global electricity requirements (~505 GW) is produced from solar PV modules. Seeing the enormous potential of solar energy as a “clean” source of power, many countries have pledged to increase the contribution of solar power in their energy budget under the Paris Climate Agreement.¹⁷

At present, around 85-90% of the solar PV modules on the market are various forms of crystalline silicon. While the levelized cost of energy using silicon modules has gone down by over 80% between 2010 and 2018,¹⁴ there remains a need for new materials for PV applications, which could require less processing, be easy to handle and altogether have the potential for large-scale commercialization. Here, organic materials appear as a viable class with a number of advantageous functionalities. Steady improvements in device power conversion efficiencies and stability have been obtained over the last few years.^{10, 18-20} In addition, the capability of organic materials to be printable on a large area, in high throughput roll-to-roll fashion, allows easier integration into electronic materials platforms. Thus, organic photovoltaics is a strong contender that displays promising prospects to satisfy the needs of future technological advancements.

1.2.2 OFET's

Field-effect transistors (FET) are now ubiquitous in electronics industry. Primarily, the FETs are electronic devices used to control the flow of current. Depending on the material used as the semiconductor/substrate different types of inorganic FETs exists, with applications ranging from displays to sensors, imaging and logic applications.

Rising cost of materials and high-temperature processing requirements have initiated efforts to identify materials that could be manufactured from relatively low-cost processing techniques. Also, FETs are normally fabricated on silicon-based substrates. However, for newer commercial applications like radio-frequency identification (RFID) tags or card readers, semiconducting materials are required which can be fabricated on plastic substrates. Here, organic-FETs, utilizing the semiconducting properties of organic materials, form an attractive prospect. Organic materials can be deposited on different types of substrates and do not need epitaxial templating for use in device configurations. Additionally, the performance of OFETs in thin-film transistor (TFT) configurations is now comparable to those obtained using amorphous silicon-based transistors. OTFTs exhibiting mobility values greater than $10 \text{ cm}^2/\text{Vs}$ are already reported.²¹ There is a strong interest to develop new materials and efforts are in progress to utilize these materials for applications for which inorganic FET's are less adequate.²² This area is also destined to witness a large expansion in market penetration in the form of wearable plastic devices for consumer applications.

1.3 Materials and their combinations for organic electronic devices

Organic materials used for optoelectronic applications are broadly categorized into three types – small molecules, oligomers and polymers. The π -conjugation is a key aspect responsible for most of the relevant properties in these materials, which can be tuned by varying their conjugation length. Another important aspect is the nature of packing of these materials in their bulk phases, as packing strongly influences intermolecular interactions and the electronic properties.^{1, 23-25}

The tunability of properties is achieved by tailoring the backbones through chemical substitutions²⁻⁵ or modulating the side-chain patterns,^{1, 26, 27} among others. Representative examples of small-molecule semiconductors are aromatic hydrocarbons including anthracene, pentacene, fullerenes and their derivatives, porphyrins or oligothiophenes, etc. (see **Figure 1.1**).

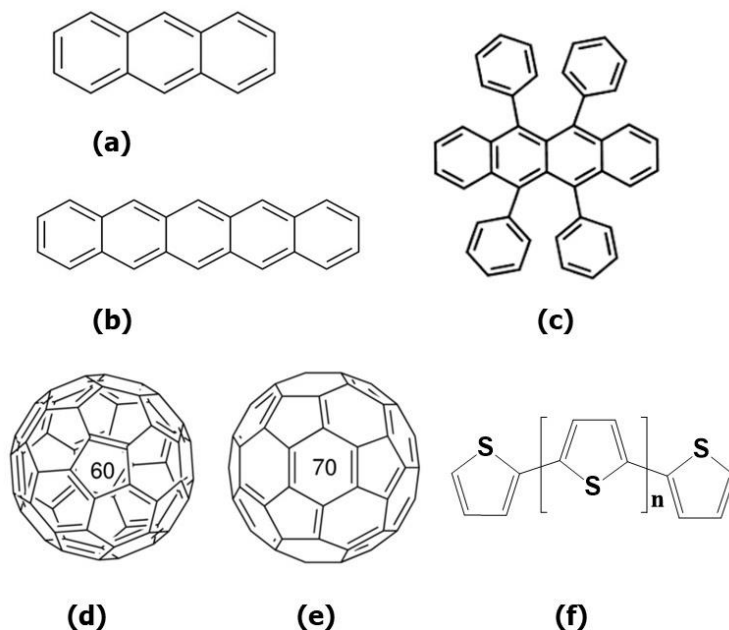


Figure 1.1 Illustration of the chemical structures of representative small-molecule semiconductors: (a) anthracene, (b) pentacene, (c) rubrene, (d) fullerene-C₆₀, (e) fullerene-C₇₀, (f) oligothiophenes.

On the application side, initially, linear conjugated polymers gained importance not only as conducting materials but also as semiconductors with possible applications in OPV's and OLED's. These polymers are made conducting by chemical or electrochemical doping. Representative examples for linear π -conjugated polymers include poly-para-phenylenes and their derivatives, polythiophenes with varied alkyl substitution on the backbone, and polyanilines (see **Figure 1.2**), to name but a few.

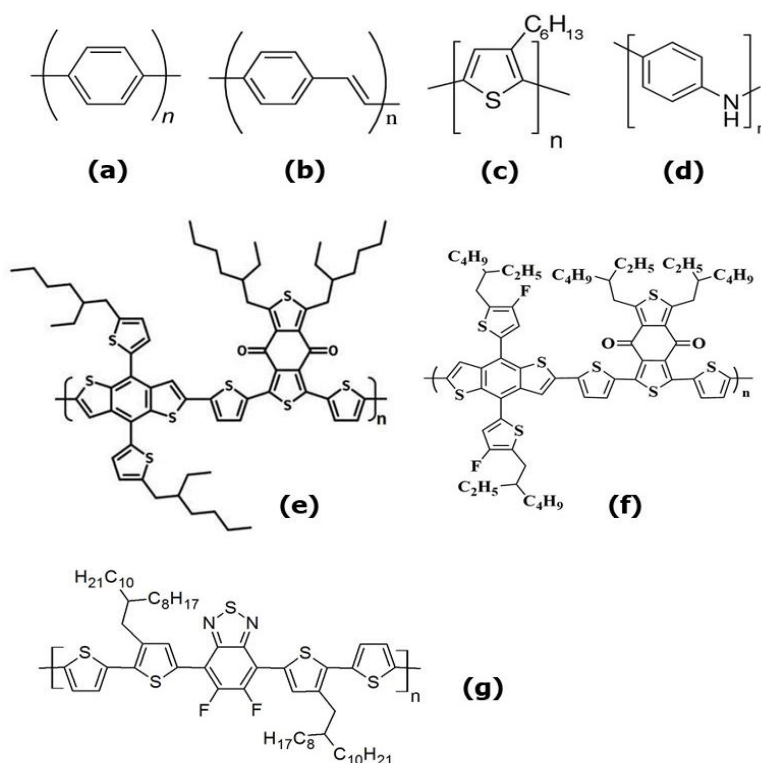


Figure 1.2. Illustration of the chemical structures of representative polymers functioning as p-type semiconductors - (a) poly-p-phenylene (PPP), (b) poly-p-phenylene vinylene (PPV), (c) poly-3-hexyl-thiophene (P3HT), (d) poly-aniline, (e) poly[[4,8-bis[5-(2-ethylhexyl)-2-thienyl]benzo[1,2-b:4,5-b']dithiophene-2,6-diyl]-2,5-thiophenediyl[5,7-bis(2-ethylhexyl)-4,8-dioxo-4H,8H-benzo[1,2-c:4,5-c']dithiophene-1,3-diyl]] (PBDB-T), (f) 1-(5-(4,8-bis(5-(2-ethylhexyl)-4-fluorothiophen-2-yl)-6-methylbenzo[1,2-b:4,5-b']dithiophen-2-yl)thiophen-2-yl)-5,7-bis(2-ethylhexyl)-3-(5-methylthiophen-2-yl)-benzo[1,2-c:4,5-c']dithiophene-4,8-dione (PM6), (g) poly[(5,6-difluoro-2,1,3-benzothiadiazol-4,7-diyl)-alt-(3,3''-di(2-octyldodecyl)-2,2';5',2'';5'',2'''-quaterthiophen-5,5'''-diyl)] (PffBT4T-2OD).

Interestingly, materials development with specific applications for OPV and OFETs were closely related to the processes taking place in their device operation. For OPV materials, a critical function in operation is the dissociation of excitons (coulombically bound electron-hole pair) and transport of separated charges to the electrodes. To achieve efficient exciton dissociation, the active layer requires the presence of two components- one acting as electron donor and the other as electron-acceptor.^{28, 29} The electron donor functions as a p-type semiconductor and transports holes to the hole-collecting electrode while the electron acceptor functions as an n-type semiconductor and transports electrons to the electron collecting electrode. Up to recently, conjugated polymers and small molecules like fullerenes and their derivatives have been utilized as electron donor and electron acceptor (see **Figures 1.2 & 1.3**), respectively, in OPV devices.³⁰ Over the past three years, a new generation of small-molecule acceptors, not based on fullerenes, has appeared (see **Figure 1.3**).

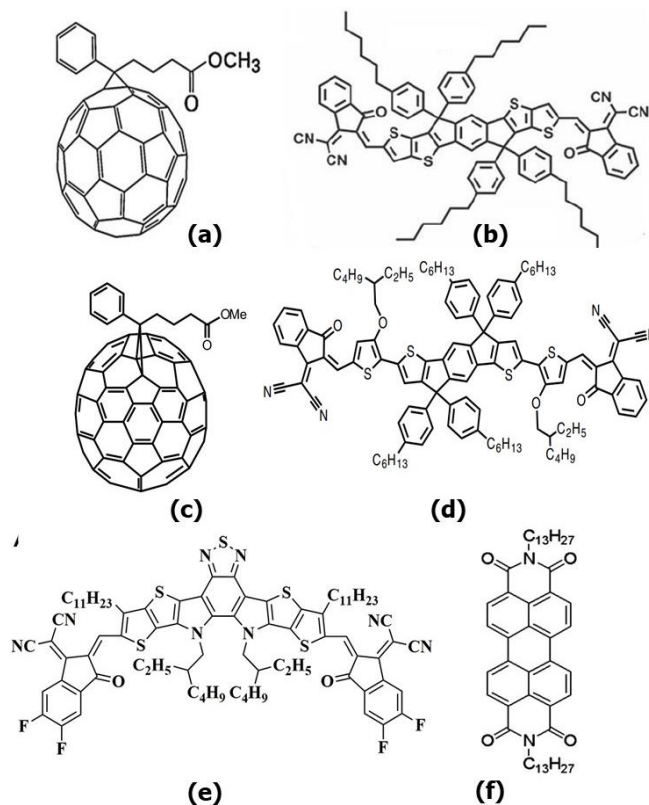


Figure 1.3. Illustration of the chemical structures of representative acceptor molecules functioning as n-type semiconductors - (a) phenyl-C61-butyric acid methyl ester (PC₆₁BM), (b) 3,9-bis(2-methylene-(3-(1,1-dicyanomethylene)-indanone))-5,5,11,11-tetrakis(4-hexylphenyl)-dithieno [2,3-d:2',3'-d']-s-indaceno [1,2-b:5,6-b'] dithiophene (ITIC), (c) phenyl-C71-butyric acid methyl ester (PC₇₁BM), (d) 2,2'-((2Z,2'Z)-((5,5'-(4,4,9,9-tetrakis(4-hexylphenyl)-4,9-dihydro-s-indaceno[1,2-b:5,6-b']dithiophene-2,7-diyl)bis(4-((2-ethylhexyl)-oxy)thiophene-5,2-diyl))bis(methanylylidene))bis(3-oxo-2,3-di-hydro-1H-indene-2,1-diylidene))dimalononitrile (IEICO), (e) (2,20-((2Z,20Z)-((12,13-bis(2-ethylhexyl)-3,9-diundecyl-12,13-dihydro-[1,2,5]thiadiazolo[3,4-e]thieno[2,"30':4',50]thieno[20,30:4,5]pyrrolo[3,2-g]thieno[20,30:4,5]thieno[3,2-b]indole-2,10-diyl)bis(me-thanylylidene))bis(5,6-difluoro-3-oxo-2,3-dihydro-1H-indene-2,1-diylidene))dimalononitrile) (Y6), (f) N,N'-ditridecylperylene-3',4,9,10-tetracarboxylic di-imide (PTCDI-C13).

At this stage, it is important to discuss the nature of the two-component systems in the active layer of the OPV device. The first configuration constructed was that of a “bi-layer”, prepared by placing a thin layer of acceptor material over a thin layer of donor material or vice-versa. In this architecture, however, many excitons decay back to the ground state before reaching the donor/acceptor interfaces. To solve this issue, another architecture, referred to as a “bulk-heterojunction” (BHJ) structure has been introduced; here, the active layer consists of a blend of donor and acceptor components. Therefore, the interfacial area is significantly increased, which allows excitons easier access to the interface and separation into free charges.

For polymer-fullerene based BHJ OPV devices, the improvement in efficiencies was mainly realized via structural modification of the polymer donors. To increase the photon utilization at the near IR region of the solar spectrum, low optical-gap polymer donors that contain alternating electron-rich and electron-poor moieties have been commonly used. Recent developments in non-fullerene acceptors (NFAs) have provided effective ways to overcome some of the fundamental limitations of fullerene-based acceptors. NFAs present distinctive advantages, such as tunable bandgap which can broaden absorption in the NIR region, tunable planarity and crystallinity,

which controls the active-layer morphology or adjustable energy level alignments to achieve suitable ionization energy (IE)/ electron affinity (EA) offsets, which can lead to a higher charge-transfer (CT) state energy and lower voltage loss (see **Figure 1.3** for representative examples). Consequently, power conversion efficiencies now reach over 16% for single-junction organic solar cell devices¹⁰ and 17.3% for tandem devices.¹⁹

Materials development for OFET devices has closely followed the developments on the OPV side. A large library of crystalline small molecules for n-channel and p-channel conduction has been generated, which show mobility values superior to those exhibited by amorphous silicon. A newer class of two-component materials that exhibit n-channel, p-channel and ambipolar transport characteristics with potential applications in OFET devices are donor-acceptor co-crystals. These are synthesized via a co-crystallization process and exhibit well-defined packing in the crystalline regime. In 1:1 stoichiometry, typically, two types of packing configurations are identified. In the first type, known as the “segregated” type, the donor and acceptor molecules align themselves in separate ordered stacks. The second type involves an alternating arrangement of donor and acceptor molecules along the stacking directions and are known as the “mixed” type of co-crystals. When free of disorder or other instabilities, the segregated type can exhibit metallic-like conductivities.³¹ However, the mixed type co-crystals are generally semiconductors or insulators.³²⁻³⁴

1.4 Key processes in OPV and OFET devices

We now provide a brief description of the main electronic processes in OPV and OFET devices. Here, we briefly note that the operation of OLED devices roughly follows a reverse order to that in OPV devices, but since OLEDs are not the focus of this Thesis, we do not discuss these devices here in detail.

The main processes in the functioning of an OPV device takes place in the active layer and at the interfaces between active layer and electrodes. They can be summarized as follows. First, (i) photon absorption takes place in the π -conjugated materials in the active layer. Electrons are excited in the electron donor or acceptor component leading to formation of coulombically bound electron-hole pairs referred to as “excitons”. Excitons are neutral species; (ii) they diffuse and reach the donor-acceptor interface, where (iii) they can dissociate via electron or hole transfer from electron donor component to electron acceptor component or vice versa, leading to formation of charge-transfer (CT) excitons. The electron on the acceptor site and the hole on the donor site in a CT state are still coulombically bound. Finally, (iv) the CT states dissociate to form charge-separated (CS) states in which the charges move away from one another to their respective electrodes.^{35, 36}

We note that each of these processes have an accompanying energy-loss pathway associated with them, which directly impacts the device efficiency. Importantly, here the process of charge-recombination that can be either radiative or non-radiative requires special attention. First of all, excitons, especially in bilayer devices, can decay back to ground state before reaching the interface due to a large distance to the interface and limited diffusion length. The bulk-heterojunction

architecture marginalized this form of loss by allowing the formation of excitons close to the interface. However, we note that in BHJ blends, two major loss mechanisms through charge-recombination exists during solar-cell operation. In the first type, known as “geminate recombination”, the CT states recombine to the ground state before dissociation into free charges. In the second mechanism referred to as non-geminate recombination, during migration of charges to their respective electrodes, a hole and electron may find one another and reform a CT state that could decay to the ground state or a low-energy triplet state.

The morphology of the active layer plays a determining role in efficient solar-cell operation. While a highly intermixed nature of the blend in the BHJ active layer can lead to a higher magnitude of non-geminate recombination, a lower intermixing of the blend can lead to limited exciton dissociation. In this context, it has been shown that domain sizes on the order of ~20-40 nm in the active layer are crucial for optimum performance of OPV devices.¹⁸ While improvement in crystallinity of the domains will have a positive effect on charge transport, higher crystallinity can result in larger domain sizes, which negatively affects device performance.³⁷ Domain sizes larger than the exciton diffusion lengths indeed lead to exciton trapping and a larger extent of geminate recombination in the active layer. In addition, disorder effects, grain boundary effects, the processing method or the substrates can also impact the morphology and the molecular packing in the active layer. It is hence worth noting that subtle interplays among many different parameters determine the performance. Altogether, optimizing the morphology of the active layer remains a key aspect in optimizing solar-cell performance.

OFET devices contain three terminals (electrodes) - source, drain and gate. The main components of an OFET device are the organic semiconducting layer, a dielectric layer and the electrodes. While the organic layer provides the conducting channel for the charges, the dielectric layer is used to capacitively induce charges in the organic semiconducting layer using an applied field to the gate electrode. The gate electrode is kept close to the conducting channel to control the flow of charge carriers. Conduction occurs from source to drain. Inorganic materials like SiO₂, Al₂O₃ or non-conjugated materials like polystyrene, poly(vinyl phenol) etc., are used as dielectric materials. The gate electrodes can be metals like Au or conducting polymers like polyaniline. Depending on the material properties of the organic semiconductor, n-channel (electron) or p-channel (hole) conduction is displayed.³⁸ In the case of co-crystals, charge-transfer is controlled by the intermolecular interactions between the donor and acceptor components, leading to a ground state with (partial) CT character. A molecular-scale understanding is important to identify the impact of packing and donor-acceptor interactions on the charge-transport properties, which can lead to the design of organic semiconductors with improved charge transport.

1.5 Morphology, its impact on transport parameters and disorder

Until now, we have highlighted the various aspects of operation of organic electronic devices and the loss pathways inhibiting their performance. It is well documented that the active-layer morphology plays a crucial role in determining device performance. At this stage, it is useful to express the active layer morphology of a bulk-heterojunction in terms of “global” and “local” features. While the global morphology refers to the extent of phase separation, crystallinity, and purity of the domains, the local morphology features the local intermolecular packing (i.e., donor-donor, donor-acceptor, and acceptor-acceptor packing).³⁹

Experimentally, the BHJ layers are analyzed using various techniques like atomic force microscopy (AFM), grazing induced wide angle x-ray spectroscopy (GIWAXS), polarized-soft x-ray scattering (p-SoXS), differential scanning calorimetry (DSC), transmission electron microscopy (TEM), x-ray diffraction (XRD) studies, and cyclic voltammetry (CV) etc., to name a few. A number of details including miscibility, domain size, packing, crystallinity, phase separation etc., can be extracted from the data coming from such techniques. Using some of these experimental techniques, it has already been demonstrated that in the P3HT/PC₇₀BM BHJ, the active layer consists of a three-phase arrangement of domains, *i.e.*, mixed regions as well as pure regions of both donor and acceptor (macro) molecules.⁴⁰ The active layers of polymer non-fullerene acceptor systems are expected to follow the same trend. Computationally, approaches like coarse-grain (CG) simulations are used to investigate the global morphology. The local morphology can be assessed from a combination of atomistic molecular dynamics (MD) simulations and quantum-chemical calculations.

The local packing strongly determines the interactions between the donor and acceptor components and hence has significant effects on the formation of interfacial charge-transfer (CT) electronic states. As we have mentioned earlier, the CT states act as a mediator to the exciton-dissociation, charge-recombination and charge-separation processes. It has been recently reported that, while minor variations of the polymer backbone in terms of the presence or absence of fluorine atoms can increase the mean CT-state energy, the addition of electronically irrelevant alkyl groups can in fact increase the width of the CT-state energy distribution.³⁹ A linear correlation between CT-state energy and open-circuit voltage has also been well demonstrated.⁴¹

In this context, it is important to connect the current understanding of solid-state packing in the active layer to the voltage-loss mechanisms and energetic disorder in the blend systems. In amorphous blends, there are two contributions to energetic disorder.⁴²⁻⁴⁴ The first is related to the time-dependent distribution of the CT-state energies due to the electron-vibration interactions in the blend. This is known as the “dynamic” component of energetic disorder. The second contribution, referred to as “static” disorder is due to the variation in donor and acceptor positions in the blend, which produces a time-independent distribution of CT-state energies. We note that an understanding of how to reduce both these disorder contributions is important in the quest for more efficient OPV devices. While amorphous blends include energetic disorder in both dynamic and static forms, in donor-acceptor co-crystals, the energetic disorder is mostly dynamic in nature. It can also arise from the co-existence of multiple polymorphs, which can lead to lattice dislocations.

Altogether, it is now clear that variations in packing configurations bring differences in intermolecular interactions in organic materials. Our aim in this Thesis is to investigate this critical aspect in two different material combinations of the active layer for organic electronic devices – the bulk-heterojunction (BHJ) configuration in OPV applications and donor-acceptor co-crystals in OFET applications. For the BHJ blends, while the nature of global morphology is available from various experimental techniques, access to local features is scarce. In the case of donor-acceptor co-crystals, segregated and mixed types of packing of donor and acceptor molecules can result in major differences in electronic and charge-transport properties. To evaluate these properties, computational techniques can be valuable, as they not only provide details of structure-property relationship on a local scale, but also provide insight to rationalize the variability in device

parameters. An in-depth understanding on the molecular-scale aspects gained from our investigations will contribute to design more efficient OPV and OFET devices.

1.6. Thesis objective and outline

In this Thesis, our investigations focus on two combinations of donor-acceptor materials – polymer/non-fullerene combinations for bulk-heterojunctions and donor-acceptor co-crystals.

With this work, we aim:

1. To gain a better understanding of the influence of packing and local interactions in pure and mixed regions of donor-acceptor BHJ blends on their electronic and charge-transport properties.
2. To assess the nature and influence of local packing and electron-phonon interactions on the electronic, charge-transport and vibrational properties in donor-acceptor co-crystals.

To do so, we seek to provide descriptions of structure-morphology-property relationships in various material combinations. After a brief overview of our computational methodologies in Chapter-2, the results of our investigations are organized as follows:

- In Chapters 3 & 4, we discuss our results on materials used in bulk-heterojunction active layers. In Chapter 3, we analyze the impact of molecular-scale interactions responsible for a temperature dependent aggregation of pure polymer donors in solution on eventual power conversion efficiencies. In Chapter 4, we investigate the effect of local interactions in the mixed phase of polymer donor non-fullerene small molecule acceptor blends on the

photovoltaic parameters. Also, we collect some useful trends obtained from our investigations on binary blends, to rationalize the photovoltaic properties of ternary blends.

- In Chapters 5, & 6, we discuss our investigation of the electronic, vibrational and charge-transport properties of various co-crystals systems. In Chapter 5, we focus on the co-crystals made of the F6TNAP acceptor and a variety of donor molecules. Here, we are able to correlate our observations with experimental investigations and explain the trends observed in their electronic and charge-transport properties. In Chapter 6, we focus on C_nBTBT-F_mTCNQ co-crystals. Our aim is to understand the impact of alkyl chain length on the donor and of fluorination of the acceptor on the co-crystal properties. Further we quantify the ground-state charge-transfer using an approach based on Mulliken charges.

1.7. References

1. Graham, K. R.; Cabanetos, C.; Jahnke, J. P.; Idso, M. N.; El Labban, A.; Ngongang Ndjawa, G. O.; Heumueller, T.; Vandewal, K.; Salleo, A.; Chmelka, B. F.; Amassian, A.; Beaujuge, P. M.; McGehee, M. D., Importance of the Donor:Fullerene Intermolecular Arrangement for High-Efficiency Organic Photovoltaics. *Journal of the American Chemical Society* **2014**, *136* (27), 9608-9618.
2. Li, Z.; Jiang, K.; Yang, G.; Lai, J. Y. L.; Ma, T.; Zhao, J.; Ma, W.; Yan, H., Donor polymer design enables efficient non-fullerene organic solar cells. *Nature Communications* **2016**, *7*, 13094.
3. Li, Z.; Tsang, S.-W.; Du, X.; Scoles, L.; Robertson, G.; Zhang, Y.; Toll, F.; Tao, Y.; Lu, J.; Ding, J., Alternating Copolymers of Cyclopenta[2,1-b;3,4-b']dithiophene and Thieno[3,4-c]pyrrole-4,6-dione for High-Performance Polymer Solar Cells. *Advanced Functional Materials* **2011**, *21* (17), 3331-3336.
4. Piliago, C.; Holcombe, T. W.; Douglas, J. D.; Woo, C. H.; Beaujuge, P. M.; Fréchet, J. M. J., Synthetic Control of Structural Order in N-Alkylthieno[3,4-c]pyrrole-4,6-dione-Based Polymers for Efficient Solar Cells. *Journal of the American Chemical Society* **2010**, *132* (22), 7595-7597.
5. Stuart, A. C.; Tumbleston, J. R.; Zhou, H.; Li, W.; Liu, S.; Ade, H.; You, W., Fluorine Substituents Reduce Charge Recombination and Drive Structure and Morphology Development in Polymer Solar Cells. *Journal of the American Chemical Society* **2013**, *135* (5), 1806-1815.
6. Shirakawa, H.; Louis, E. J.; MacDiarmid, A. G.; Chiang, C. K.; Heeger, A. J., Synthesis of electrically conducting organic polymers: halogen derivatives of polyacetylene, (CH). *Journal of the Chemical Society, Chemical Communications* **1977**, (16), 578-580.
7. Popovic, Z. D.; Hor, A.-m.; Loutfy, R. O., A study of carrier generation mechanism in benzimidazole perylene/tetraphenyldiamine thin film structures. *Chemical Physics* **1988**, *127* (1), 451-457.
8. Shattuck, M. D.; Vahtra, U., Organic photoconductive compositions and their use in electrophotographic processes. *U.S. PATENT*, 3,484,237 **1969**.
9. Umeda, M.; Niimi, T.; Hashimoto, M., Photocarrier Generation in a Layered Organic Photoreceptor Containing Azo Pigment. *Japanese Journal of Applied Physics* **1990**, *29* (Part 1, No. 12), 2746-2750.
10. Cui, Y.; Yao, H.; Zhang, J.; Zhang, T.; Wang, Y.; Hong, L.; Xian, K.; Xu, B.; Zhang, S.; Peng, J.; Wei, Z.; Gao, F.; Hou, J., Over 16% efficiency organic photovoltaic cells enabled by a chlorinated acceptor with increased open-circuit voltages. *Nature Communications* **2019**, *10* (1), 2515.
11. Yoshikawa, K.; Kawasaki, H.; Yoshida, W.; Irie, T.; Konishi, K.; Nakano, K.; Uto, T.; Adachi, D.; Kanematsu, M.; Uzu, H.; Yamamoto, K., Silicon heterojunction solar cell with interdigitated back contacts for a photoconversion efficiency over 26%. *Nature Energy* **2017**, *2*, 17032.
12. Saga, T., Advances in crystalline silicon solar cell technology for industrial mass production. *Npg Asia Materials* **2010**, *2*, 96.
13. Fraunhofer institute for Solar Energy Systems, I., Photovoltaics-Report - <https://www.ise.fraunhofer.de/en/publications/studies/photovoltaics-report.html>. **2019**.

14. Fu, R.; Feldman, D.; Margolis, R., U.S. Solar photovoltaic system cost benchmark: Q1 2018. **2018**.
15. Tang, C. W.; VanSlyke, S. A., Organic electroluminescent diodes. *Applied Physics Letters* **1987**, *51* (12), 913-915.
16. Edenhofer, O., R.; Pichs-Madruga, Y. S., E. Farahani, S. Kadner, K. Seyboth, A. Adler, I. Baum, S. Brunner, P. Eickemeier, B. Kriemann, J.; Savolainen, S. S., C. von Stechow, T. Zwickel and J.C. Minx Climate Change 2014: Mitigation of Climate Change. Contribution of Working Group III to the Fifth Assessment Report of the Intergovernmental Panel on Climate Change. *IPCC, 2014: Summary for Policymakers* **2014**.
17. Paris Agreement - United Nations. **2016**.
18. Liu, Y.; Zhao, J.; Li, Z.; Mu, C.; Ma, W.; Hu, H.; Jiang, K.; Lin, H.; Ade, H.; Yan, H., Aggregation and morphology control enables multiple cases of high-efficiency polymer solar cells. *Nature Communications* **2014**, *5*, 5293.
19. Meng, L.; Zhang, Y.; Wan, X.; Li, C.; Zhang, X.; Wang, Y.; Ke, X.; Xiao, Z.; Ding, L.; Xia, R.; Yip, H.-L.; Cao, Y.; Chen, Y., Organic and solution-processed tandem solar cells with 17.3% efficiency. *Science* **2018**, *361* (6407), 1094.
20. Yuan, J.; Zhang, Y.; Zhou, L.; Zhang, G.; Yip, H.-L.; Lau, T.-K.; Lu, X.; Zhu, C.; Peng, H.; Johnson, P. A.; Leclerc, M.; Cao, Y.; Ulanski, J.; Li, Y.; Zou, Y., Single-Junction Organic Solar Cell with over 15% Efficiency Using Fused-Ring Acceptor with Electron-Deficient Core. *Joule* **2019**, *3* (4), 1140-1151.
21. Liu, C.; Liu, X.; Minari, T.; Kanehara, M.; Noh, Y.-Y., Organic thin-film transistors with over 10 cm²/Vs mobility through low-temperature solution coating. *Journal of Information Display* **2018**, *19* (2), 71-80.
22. Sirringhaus, H., Device Physics of Solution-Processed Organic Field-Effect Transistors. *Advanced Materials* **2005**, *17* (20), 2411-2425.
23. Chen, X.-K.; Ravva, M. K.; Li, H.; Ryno, S. M.; Brédas, J.-L., Effect of Molecular Packing and Charge Delocalization on the Nonradiative Recombination of Charge-Transfer States in Organic Solar Cells. *Advanced Energy Materials* **2016**, *6* (24), 1601325.
24. Xie, Y.; Ge, Y.; Peng, Q.; Li, C.; Li, Q.; Li, Z., How the Molecular Packing Affects the Room Temperature Phosphorescence in Pure Organic Compounds: Ingenious Molecular Design, Detailed Crystal Analysis, and Rational Theoretical Calculations. *Advanced Materials* **2017**, *29* (17), 1606829.
25. Zhang, X.; Richter, L. J.; DeLongchamp, D. M.; Kline, R. J.; Hammond, M. R.; McCulloch, I.; Heeney, M.; Ashraf, R. S.; Smith, J. N.; Anthopoulos, T. D.; Schroeder, B.; Geerts, Y. H.; Fischer, D. A.; Toney, M. F., Molecular Packing of High-Mobility Diketo Pyrrolo-Pyrrole Polymer Semiconductors with Branched Alkyl Side Chains. *Journal of the American Chemical Society* **2011**, *133* (38), 15073-15084.
26. Liang, Y.; Feng, D.; Wu, Y.; Tsai, S.-T.; Li, G.; Ray, C.; Yu, L., Highly Efficient Solar Cell Polymers Developed via Fine-Tuning of Structural and Electronic Properties. *Journal of the American Chemical Society* **2009**, *131* (22), 7792-7799.
27. Subramaniyan, S.; Xin, H.; Kim, F. S.; Shoaee, S.; Durrant, J. R.; Jenekhe, S. A., Effects of Side Chains on Thiazolothiazole-Based Copolymer Semiconductors for High Performance Solar Cells. *Advanced Energy Materials* **2011**, *1* (5), 854-860.
28. Yu, G.; Gao, J.; Hummelen, J. C.; Wudl, F.; Heeger, A. J., Polymer Photovoltaic Cells: Enhanced Efficiencies via a Network of Internal Donor-Acceptor Heterojunctions. *Science* **1995**, *270* (5243), 1789.

29. Halls, J. J. M.; Walsh, C. A.; Greenham, N. C.; Marseglia, E. A.; Friend, R. H.; Moratti, S. C.; Holmes, A. B., Efficient photodiodes from interpenetrating polymer networks. *Nature* **1995**, *376* (6540), 498-500.
30. Shirota, Y.; Kageyama, H., Small molecular weight materials for (opto)electronic applications: overview. In *Handbook of Organic Materials for Optical and (Opto)electronic Devices*, Ostroverkhova, O., Ed. Woodhead Publishing: 2013; pp 3-82.
31. Ferraris, J. P.; Poehler, T. O.; Bloch, A. N.; Cowan, D. O., Synthesis of the highly conducting organic salt: tetramethyltetrathiofulvalenium - tetracyano-p-quinodimethane. *Tetrahedron Letters* **1973**, *14* (27), 2553-2556.
32. Emge, T. J.; Wiygul, F. M.; Chappell, J. S.; Bloch, A. N.; Ferraris, J. P.; Cowan, D. O.; Kistenmacher, T. J., Crystal Structures for the Electron Donor Dibenzotetrathiafulvalene, DBTTF, and Its Mixed-stack Charge-transfer Salts with the Electron Acceptors 7,7,8,8-tetracyano-p-quinodimethane, TCNQ, and 2,5-difluoro-7,7,8,8-tetracyano-p-quinodimethane, 2,5-TCNQF2. *Molecular Crystals and Liquid Crystals* **1982**, *87* (1-2), 137-161.
33. Kobayashi, H.; Nakayama, J., The Crystal Structure of the Charge-transfer Complex of Dibenzotetrathiafulvalene-Tetracyanoquinodimethane, DBTTF-TCNQ. *Bulletin of the Chemical Society of Japan* **1981**, *54* (8), 2408-2411.
34. Torrance, J. B.; Mayerle, J. J.; Bechgaard, K.; Silverman, B. D.; Tomkiewicz, Y., Comparison of two isostructural organic compounds, one metallic and the other insulating. *Physical Review B* **1980**, *22* (10), 4960-4965.
35. Brédas, J.-L.; Norton, J. E.; Cornil, J.; Coropceanu, V., Molecular Understanding of Organic Solar Cells: The Challenges. *Accounts of Chemical Research* **2009**, *42* (11), 1691-1699.
36. Kippelen, B.; Brédas, J.-L., Organic photovoltaics. *Energy & Environmental Science* **2009**, *2* (3), 251-261.
37. Yang, G.; Li, Z.; Jiang, K.; Zhang, J.; Chen, J.; Zhang, G.; Huang, F.; Ma, W.; Yan, H., Optimal extent of fluorination enabling strong temperature-dependent aggregation, favorable blend morphology and high-efficiency polymer solar cells. *Science China Chemistry* **2017**, *60* (4), 545-551.
38. Brédas, J.-L.; Marder, S. R., *The WSPC Reference on Organic Electronics: Organic Semiconductors*. WORLD SCIENTIFIC: 2015; Vol. Volume 7, p 896.
39. Wang, T.; Chen, X.-K.; Ashokan, A.; Zheng, Z.; Ravva, M. K.; Brédas, J.-L., Bulk Heterojunction Solar Cells: Impact of Minor Structural Modifications to the Polymer Backbone on the Polymer-Fullerene Mixing and Packing and on the Fullerene-Fullerene Connecting Network. *Advanced Functional Materials* **2018**, *28* (14), 1705868.
40. Sweetnam, S.; Graham, K. R.; Ngongang Ndjawa, G. O.; Heumüller, T.; Bartelt, J. A.; Burke, T. M.; Li, W.; You, W.; Amassian, A.; McGehee, M. D., Characterization of the Polymer Energy Landscape in Polymer:Fullerene Bulk Heterojunctions with Pure and Mixed Phases. *Journal of the American Chemical Society* **2014**, *136* (40), 14078-14088.
41. Burke, T. M.; Sweetnam, S.; Vandewal, K.; McGehee, M. D., Beyond Langevin Recombination: How Equilibrium Between Free Carriers and Charge Transfer States Determines the Open-Circuit Voltage of Organic Solar Cells. *Advanced Energy Materials* **2015**, *5* (11), 1500123.
42. Zheng, Z.; Tummala, N. R.; Wang, T.; Coropceanu, V.; Brédas, J.-L., Charge-Transfer States at Organic-Organic Interfaces: Impact of Static and Dynamic Disorders. *Advanced Energy Materials* **2019**, *9* (14), 1803926.

43. Tummala, N. R.; Zheng, Z.; Aziz, S. G.; Coropceanu, V.; Brédas, J.-L., Static and Dynamic Energetic Disorders in the C60, PC61BM, C70, and PC71BM Fullerenes. *The Journal of Physical Chemistry Letters* **2015**, *6* (18), 3657-3662.
44. Coropceanu, V.; Chen, X.-K.; Wang, T.; Zheng, Z.; Brédas, J.-L., Charge-transfer electronic states in organic solar cells. *Nature Reviews Materials* **2019**.

CHAPTER 2

THEORETICAL METHODOLOGY

2.1 Introduction

In this Chapter, we give a brief review of the theoretical methods applied in this Thesis. We mainly employed a combination of molecular dynamics (MD) simulations and density functional theory (DFT) calculations for examining the morphology and electronic properties of different amorphous material systems in Chapters 3 & 4. Also, we have employed band-structure calculations, effective mass calculations, and electronic coupling calculations based on density functional theory to investigate the electronic and charge-transport properties of donor-acceptor co-crystal materials in Chapters 5 & 6. Here, we start by discussing the theoretical foundations and approximations used in electronic-structure theory. Then, we describe the origins of DFT and discuss its varied levels of complexity. We also briefly discuss the band structure, effective mass, and electronic coupling concepts and the application of these concepts to treat the electronic structure of crystalline systems. Finally, we review atomistic MD simulations, discuss the parameterization of the OPLS-AA (optimized potentials for liquid simulations-all atom) force-field, and provide a brief description of MD simulations applied to materials systems.

2.2. The Schrödinger Equation

All the properties of a stationary quantum-mechanical system containing N electrons and M nuclei can be derived from the eigenfunctions, ψ_i , and the eigenvalues, E_i , of the system's Hamiltonian operator, \hat{H} . The ψ_i and E_i values are obtained by solving the many-body, time-independent Schrödinger equation:

$$\hat{H}|\psi_i\rangle = E_i|\psi_i\rangle \quad (2.1)$$

In the absence of relativistic effects, the Hamiltonian operator is given by the sum of the kinetic and potential energy operators of all particles associated with the system. In the case of a many-body system, this includes all the nuclear-nuclear, nuclear-electron, and electron-electron interactions, and is given by:

$$\hat{H} = -\frac{1}{2}\sum_{i=1}^N \nabla_i^2 - \frac{1}{2}\sum_{A=1}^M \frac{1}{M_A} \nabla_A^2 - \sum_{i=1}^N \sum_{A=1}^M \frac{Z_A}{r_{iA}} + \sum_{i=1}^N \sum_{j>i}^N \frac{1}{r_{ij}} + \sum_{A=1}^M \sum_{B>A}^M \frac{Z_A Z_B}{r_{AB}} \quad (2.2)$$

where ∇_i^2 and ∇_A^2 are the Laplacians corresponding to second-order partial derivatives with respect to the coordinates of the i^{th} electron and A^{th} nucleus, respectively. M_A and Z_A represent the mass and (positive) charge of the A^{th} nucleus, respectively; $r_{ij}=|\mathbf{r}_i-\mathbf{r}_j|$ corresponds to the distance between the i^{th} and j^{th} electrons, $r_{iA}=|\mathbf{r}_i-\mathbf{r}_A|$, the distance between i^{th} electron and A^{th} nucleus, and $r_{AB}=|\mathbf{r}_A-\mathbf{r}_B|$, the distance between A^{th} and B^{th} nucleus, respectively. The first two terms to the right of Equation (2.2) denote the kinetic energy operators for the electrons and nuclei in the system, respectively. The third term to the right represents the electron-nuclear attraction; the fourth term the electron-electron interactions; and the last term, the nuclear-nuclear interactions.

Born-Oppenheimer approximation

Solving the Schrödinger equation provides an exact solution only for hydrogen-like atoms; in all the other cases, because of the presence of multiple nuclear-nuclear, electron-electron and nuclear-electron many-body interactions, several approximations have to be introduced. The first approximation involves separating the nuclear and electronic coordinates. This is known as the *Born-Oppenheimer approximation* and primarily arises from the large difference in masses of electron and nucleus; the mass of a proton (1.6726×10^{-27} kg), or of a neutron (1.6749×10^{-27} kg) is approximately 2000 times the electron mass (9.1093×10^{-31} kg). Within the Born-Oppenheimer

approximation, the Schrödinger equation is solved in two steps. In the first step, electronic motion is approximated to be under the static field of fixed nuclei by neglecting the nuclear dynamics. Then, the Hamiltonian operator simplifies into an electronic Hamiltonian (\hat{H}_{el}) that depends parametrically on the nuclear positions. This leads to the following electronic Schrödinger equation:

$$\hat{H}_{el}(r, R)\psi_{el}(r, R) = E_{el}(R)\psi_{el}(r, R) \quad (2.3)$$

In the second step, R is varied, which gives the wavefunctions $\psi_{el}(r, R)$ and the electronic energies $E_{el}(R)$ referred to as adiabatic potential energies.

2.2.1. Hartree-Fock Theory

Because of the complexity in addressing the (many-body) electron-electron interactions, additional approximations are introduced, the first of which assumes that the electrons do not interact with each other. This approximates the total wavefunction of the system to be a product of independent electron wavefunctions (orbitals). The resulting wavefunction, known as a *Hartree product*, is represented as a product of *spin-orbital* (product of spatial orbital and spin) wavefunctions for each electron:

$$\Psi^{HP}(x_1, x_2, \dots, x_N) = \chi_1(x_1) \chi_2(x_2) \dots \chi_N(x_N) \quad (2.4)$$

where the spin-orbitals are defined as:

$$\chi_i(x) = \begin{cases} \Psi_i(x) \alpha(\omega) \\ \Psi_i(x) \beta(\omega) \end{cases} \quad (2.5)$$

An essential condition in accordance to Pauli's exclusion principle is that the many electron total wavefunction should be antisymmetric with respect to exchange of positions by any two electrons in the system. This is represented as:

$$\Psi(x_1, x_2, \dots, x_i, x_j, \dots, x_N) = -\Psi(x_1, x_2, \dots, x_j, x_i, \dots, x_N) \quad (2.6)$$

Note that Equation (2.4) does not satisfy the Pauli exclusion principle. A simple approach to antisymmetrize the wavefunction of N-electron system is by the use of a single Slater determinant.

The representation of a Slater determinant is done as follows:

$$\psi(x_1, x_2, \dots, x_N) = \frac{1}{\sqrt{N!}} \begin{vmatrix} \chi_i(x_1) & \chi_j(x_1) & \dots & \chi_k(x_1) \\ \chi_i(x_2) & \chi_j(x_2) & \dots & \chi_k(x_2) \\ \vdots & \vdots & \ddots & \vdots \\ \chi_i(x_N) & \chi_j(x_N) & \dots & \chi_k(x_N) \end{vmatrix} \quad (2.7)$$

where $\frac{1}{\sqrt{N!}}$ denotes the normalization factor and $\chi(x)$ are the spin-orbitals. Discarding any electron-electron interaction turns out to be much too crude an approximation. Re-introducing such interactions was done by Hartree and by Fock, by considering that each electron evolves in the mean field due to the other electrons. In the Hartree-Fock approximation, we have:

$$E_{el} = \langle \Psi_{el} | \hat{H}_{el} | \Psi_{el} \rangle$$

$$E_{el} = \sum_i^N \langle i | h | i \rangle + \frac{1}{2} \sum_{ij}^N [ii|jj] - [ij|ji] \quad (2.8)$$

where the first term in Equation (2.8) represents one-electron integrals and includes the contributions of electron kinetic energies and electron-nuclear interactions, which writes;

$$\langle i | h | i \rangle = \int dx_i \chi_i^*(x_1) \left\{ -\frac{1}{2} \nabla^2 - \sum_A^M \frac{z_A}{r_{iA}} \right\} \chi_i(x_1) \quad (2.9)$$

The second term in Equation (2.8) includes the two-electron Coulomb and exchange integrals respectively, which correspond to:

$$[ii|jj] = \int dx_1 dx_2 \chi_i^*(x_1) \chi_i(x_1) \frac{1}{r_{12}} \chi_j^*(x_2) \chi_j(x_2) = J_j(x_1)$$

and

$$[ij|ji] = \int dx_1 dx_2 \chi_i^*(x_1) \chi_j(x_1) \frac{1}{r_{12}} \chi_j^*(x_2) \chi_i(x_2) = K_j(x_1) \chi_j(x_1) \quad (2.10)$$

Thus, the one-electron operator, h , and two-electron operator, v (i, j) are defined as:

$$h(i) = -\frac{1}{2} \nabla_i^2 - \sum_A \frac{Z_A}{r_{iA}}$$

$$v(i, j) = \frac{1}{r_{ij}}. \quad (2.11)$$

The *Hartree-Fock approximation* leads to the ground state of a multi-electron system to be described with a single Slater determinant. An important aspect is that the *variational theorem* can be applied to minimize the total energy of the system and obtain the lowest-energy wavefunction. To apply the variational method, the initial and the final orbitals are restricted to orthonormality using the Lagrange's method of undetermined multipliers. The Hartree-Fock equations then assumes the form:

$$h(x_1) \chi_i(x_1) + \sum_{j \neq i} \left[\int dx_2 |\chi_j(x_2)|^2 r_{12}^{-1} \right] \chi_i(x_1) - \sum_{j \neq i} \left[\int dx_2 \chi_j^*(x_2) \chi_i(x_2) r_{12}^{-1} \right] \chi_j(x_1) = \varepsilon_i \chi_i(x_1) \quad (2.12)$$

Based on the definitions made for Coulomb and exchange integrals in Equation (2.10), a one-electron Hartree-Fock equation could be written as:

$$\left[h(x_1) + \sum_{j \neq i} J_j(x_1) - \sum_{j \neq i} K_j(x_1) \right] \chi_i(x_1) = \varepsilon_i \chi_i(x_1) \quad (2.13)$$

The Hartree-Fock equations can be solved either numerically or by using a set of known basis functions. The equations must be solved iteratively which corresponds to a *self-consistent field (SCF)* approach with the solutions dependent on the initial guess of orbitals. In the latter case, the spin orbitals are defined by a linear combination of atomic orbitals (LCAO approach), which is represented as:

$$\chi_i = \sum_{\mu} C_{\mu}^i \phi_{\mu} \quad (2.14)$$

where C_{μ}^i are the LCAO coefficients and ϕ_{μ} corresponds to the atomic orbitals included in the basis set.

Since Hartree-Fock approach treats the electron-electron interactions in an average way, the total Hartree-Fock energy is an upper bound to the exact total energy, with the difference expressed as the correlation energy. There exist wave-function methods [like CCSD (Coupled cluster singles doubles), CCSD(T) (Coupled cluster singles doubles and perturbative triples) and MP2 (second order Moller-Plesset Perturbation Theory)] that allow the evaluation of the correlation energy. However, for the very large systems we will be investigating density functional theory turns out to be the method of choice. In the next section, we review the origins of density functional theory and the classification of functionals based on their levels of complexity and accuracy.

2.2.2. Density Functional Theory

While high-level wavefunction based methods such as MP2, CCSD(T) and CI (configuration interaction) allow for high-accuracy electronic-structure results, they quickly become computationally prohibitive for the large systems we want to study. Density functional theory (DFT) is then a method of choice to provide a good balance between accuracy and computational time.

2.2.2.1. The Hohenberg-Kohn Theorems

DFT is built on the seminal work of Hohenberg and Kohn.¹ The first Hohenberg-Kohn theorem states that “in a system of interacting particles in an external potential $V_{ext}(r)$, the external

potential $V_{ext}(r)$ is uniquely determined by the ground-state electron density, $\rho_0(r)$ ". This means that all the properties of the system can be determined from the ground-state density. The second theorem states that "for any external potential $V_{ext}(r)$, the exact ground-state energy of the system may be obtained by a variational method and the electron density that minimizes the total energy is the exact ground-state density of the system". The density writes as:

$$\rho(r) = N \int \dots \int |\Psi(x_1, x_2, \dots, x_N)|^2 dx_1 dx_2 \dots dx_N \quad (2.15)$$

With the energy of the ground state a functional of electron density, it can be expressed as:

$$E_0[\rho(r)] = T[\rho] + E_{ee}[\rho] + E_{Ne}[\rho] \quad (2.16)$$

where $T[\rho]$ represents the kinetic energy component of the Hamiltonian; $E_{ee}[\rho]$, the electron-electron repulsion component; and $E_{Ne}[\rho]$, the electron-nuclear attraction component. By separating the classical and non-classical components, Equation (2.16) can be re-written as:

$$E_0[\rho(r)] = T_{cl}[\rho] + J_{cl}[\rho] + E_{ne}[\rho] + E_{ncl}[\rho] \quad (2.17)$$

where $J(\rho)$ represents the classical part of the electron-electron interactions which is known exactly. $E_{ncl}[\rho]$ then represents all the non-classical contributions to the problem, including exchange and electron correlation. Finding the most accurate description of $E_{ncl}[\rho]$ represents the grand challenge in DFT.

2.2.2.2. Kohn-Sham Theory

Kohn and Sham proposed an approach which involves the many-body system being treated effectively as a reference system built from a set of one-electron orbitals in an effective potential.² The effective one-electron orbitals, known as Kohn-Sham orbitals, define a Slater determinant that represents the ground state wavefunction. An important advantage of this approach is that the

major part of kinetic energy can be easily calculated with the remainder merged with the non-classical contributions.

The expression for independent-particle kinetic energy is given by:

$$T_S = -\frac{1}{2} \sum_i^N \langle \varphi_i | \nabla^2 | \varphi_i \rangle \quad (2.18)$$

The corrections to kinetic energy corresponding to the actual system are added to the non-classical contributions. This is included by introducing the following form of the universal functional, $F[\rho]$:

$$F[\rho] = T_S[\rho] + J[\rho] + E_{XC}[\rho] \quad (2.19)$$

where $E_{XC}[\rho]$ represents the exchange-correlation energy that includes the corrections for kinetic energy and the non-classical electron correlation contributions. This is defined as:

$$E_{XC}[\rho] = (T[\rho] - T_S[\rho]) + (E_{ee}[\rho] - J[\rho]) \quad (2.20)$$

In Equation (2.20), the first set of terms within the bracket constitute the kinetic correlation energy and second set of terms are a combination of potential correlation energy and the exchange energy.

The expression of total energy becomes:

$$E[\rho] = T_S[\rho] + J[\rho] + E_{XC}[\rho] + E_{Ne}[\rho] \quad (2.21)$$

The corresponding Schrödinger equation can then be represented as:

$$\left\{ -\frac{1}{2} \nabla^2 + \left[\int \frac{\rho(\vec{r}_2)}{r_{12}} d\vec{r}_2 + V_{XC}(\vec{r}_1) - \sum_A^M \frac{Z_A}{r_{1A}} \right] \right\} \varphi_i = \varepsilon_i \varphi_i \quad (2.22)$$

where the exchange-correlation potential V_{XC} is defined as:

$$V_{XC} = \frac{\delta E_{XC}}{\delta \rho} \quad (2.23)$$

An exact form for the exchange-correlation energy E_{XC} and the corresponding potential V_{XC} is not known yet. The central focus of modern DFT is to find better approximations for these two quantities. As the approximations improve, the accuracy of the description of many-body systems also gets better.

2.2.2.3. Approximate exchange-correlation functionals

Unlike the wave-function based methods, DFT does not contain a systematic method for improving the accuracy of approximate functionals. Based on the complexities of their functional forms, a wide range of functionals have been developed based on different approximations. They are categorized within the concept of “Jacob’s ladder”, introduced by Perdew and Schmidt, into different rungs of the ladder.³ Here, we briefly discuss four of the most common forms of approximations used.

2.2.2.3.1. Local density approximation (LDA)

In the local density approximation, the XC functional depends only on the specific electron density at a given point in space. The exchange-correlation energy is then obtained as an integral over all space and the exchange-correlation energy density at each point is assumed to have the same energy density as that of the homogeneous electron gas. In this approximation, the exchange-correlation energy is represented in the following simple form:

$$E_{XC}^{LDA}[\rho] = \int \rho(\vec{r}) \varepsilon_{XC}(\rho(\vec{r})) d\vec{r} \quad (2.24)$$

The local density approximation allows the splitting of the exchange and correlation energies into separate exchange and correlation contributions:

$$E_{XC}^{LDA}[\rho] = E_X^{LDA}[\rho] + E_C^{LDA}[\rho] \quad (2.25)$$

Here, no explicit expression is available for the correlation part. The correlation energy is normally determined numerically and fitted to analytical expressions based on various parameterization schemes including quantum Monte Carlo simulations of the homogeneous electron gas.⁴ The most widely used LDA functionals include the Perdew and Zunger (PZ) functional⁵ and the Vosko, Wilk and Nusair (VWN)⁶ functional.

2.2.2.3.2. Generalized Gradient Approximations

In order to account for the inhomogeneous nature of the electron density of many-electron systems, especially in molecular systems, the generalized gradient approximations (GGA) includes the gradient of the charge density at a particular point in addition to the charge density at that point. The local density approximation forms the first term of the Taylor expansion of uniform densities; extending the series with the next lowest term of charge density gradient is expected to provide better approximations for the exchange-correlation functional. All the GGA functionals are described by the following functional form:

$$E_{XC}^{GGA}[\rho] = \int \rho(\vec{r}) \varepsilon_{XC}[\rho(\vec{r}), \nabla\rho(\vec{r})] d\vec{r} \quad (2.26)$$

Popular GGA functionals include the Perdew, Burke and Ernzerhof (PBE) functional,⁷ the B88 exchange functional by Becke,⁸ the PW91 functional by Perdew,⁹ or the correlation functional introduced by Lee, Yang and Parr (LYP).¹⁰

2.2.2.3.3. Hybrid functionals

In the exchange-correlation potential, the contribution of the exchange part is found to be much larger than the correlation part. An accurate description of the exchange part is therefore expected to give improved results from the DFT methods. To correctly describe the $1/r$ asymptotic decay of the DFT exchange-correlation functional, Becke proposed the inclusion of some part of exact non-local Hartree-Fock exchange into the DFT exchange.¹¹ This functional form of the exchange-correlation energy can then be represented as:

$$E_{XC} = a_0 E_X^{HF} + (1 - a_0) E_X^{DFT} + E_C^{DFT} \quad (2.27)$$

where α_0 is a constant and can vary between values of 0 and 1. Many hybrid functionals have been developed to include the exact HF exchange with the most popular functional among them being B3LYP.^{10, 12} The explicit functional form of B3LYP is as follows:

$$E_{XC}^{B3LYP} = E_X^{LDA} + a(E_X^{HF} - E_X^{LDA}) + b(E_X^{GGA} - E_X^{LDA}) + E_c^{LDA} + c(E_c^{GGA} - E_c^{VWN}) \quad (2.28)$$

where $a=0.2$, $b=0.72$, and $c=0.81$. Here, the abbreviations LDA in E_X^{LDA} and VWN in E_c^{VWN} represents the exchange energy calculated based on local density approximation and the correlation energy calculated based on the LDA Vosko, Wilk and Nusair functional respectively. The abbreviation E_X^{GGA} denotes the Becke 88 exchange functional and E_c^{GGA} corresponds to the correlation functional introduced by Lee, Yang and Parr (LYP); E_X^{HF} represents the exact exchange energy from Hartree-Fock theory.

2.2.2.3.4. Long-range corrected functionals

Even though the global hybrid functionals have achieved good results for thermochemistry, inaccurate results are observed, for instance, for the calculation of charge-transfer excited states of molecules. This was found to be due to $\sim a/r$ decay of the exchange correlation functional instead of the correct $\sim 1/r$ decay.¹³ To deal with this issue, the Coulomb operator is partitioned into short-range and long-range terms and treated separately. The general functional form of long-range corrected functionals is given by:

$$E_{XC}^{LC-DFT} = E_X^{LR-HF} + E_X^{SR-DFT} + E_C^{DFT} \quad (2.29)$$

The long-range exchange terms are treated exactly using Hartree-Fock, while the short-range exchange terms and correlation terms are approximated using Kohn-Sham DFT. This type of partitioning is achieved using a scheme as below:

$$\frac{1}{r_{12}} = \frac{erf(\omega r_{12})}{r_{12}} + \frac{erfc(\omega r_{12})}{r_{12}} \quad (2.30)$$

In Equation (2.30), the first term to the right depicts the long-range electron-electron interactions treated by Hartree Fock and the second term corresponds to short-range interactions. The parameter ω controls the partitioning of the inter-electronic distance r_{12} .

In this Thesis, we primarily employ the long-range corrected ω B97XD functional, proposed by Chai and Head-Gordon,¹⁴ in Chapters 3 and 4 and the global hybrid B3LYP functional in Chapters 5 and 6, for the evaluation of the electronic properties of different material systems. The functional form of ω B97XD is:

$$E_{XC}^{\omega B97XD} = E_X^{LR-HF} + c_x E_X^{SR-HF} + E_X^{SR-B97} + E_C^{B97} - \sum_{i=1}^{n-1} \sum_{j=i+1}^n \frac{C_6^{ij}}{R_{ij}^6} f_{damp}(R_{ij}) \quad (2.31)$$

where n is the number of atoms in the system, C_6^{ij} is the dispersion coefficient for atom pair ij , and R_{ij} is the interatomic distance. The damping function $f_{damp}(R_{ij})$ enforces the correct asymptotic pairwise van der Waals potentials as well as zero dispersion correction at short interatomic distances. When the interatomic distances are large, the damping function reduces to 1.

2.2.2.4. Non-empirical tuning of the range-separated functionals

Within the premises of closed-shell Hartree-Fock theory, Koopman's theorem states that the first ionization energy of a molecular system is equal to energy of the highest occupied molecular orbital (HOMO).¹⁵ Kohn-Sham DFT also includes its own version of Koopman's theorem, which postulates that the vertical ionization energy of a system of N electrons is mathematically equivalent to the negative of the corresponding Kohn-Sham HOMO energy of the system.¹⁶ In π -conjugated systems, the ω -value of range-separated hybrid functionals is strongly system-dependent. An optimal tuning of the ω -value is shown to improve the descriptions of optical gap in systems showing charge transfer. This is achieved by forcing the functional to satisfy the DFT-

version of the Koopman's theorem. For ω -tuning of donor-acceptor systems both ionization energy and electron affinity of the system are important. According to the "Golden Proportion" method,¹⁷ the vertical electron affinity of n-electron system is approximated as ionization potential of n+1 electron system. The tuning is performed based on the following scheme:

$$J^2 = \sum_{i=0}^1 [\epsilon_H(n+i) + IP(n+i)]^2 \quad (2.32)$$

This scheme is used for tuning the ω -value of systems considered in Chapters 3 and 4. In the next section, we briefly describe the band theory in crystals, based on the density functional theory methods described above but extended to crystals in the solid state. This forms the basis of our evaluations of electronic-structure and charge-transport properties in Chapters 5 & 6.

2.2.2.5. Band Structure and Tight-Binding Model

The bulk electronic properties of a solid-state crystalline materials are described based on the assumption that the whole crystal is formed by translations of a small group of atoms in space. The smallest repeating unit of the crystal, the unit cell, is described by using three linearly independent, non-coplanar vectors, denoted here as \vec{a} , \vec{b} , and \vec{c} . The translation vector within the crystal can be defined as:

$$T_{n_a n_b n_c} = n_a \vec{a} + n_b \vec{b} + n_c \vec{c} \quad (2.33)$$

Although infinite translations of the elementary cell are restricted by boundaries in an actual crystal, nevertheless, such a model forms an excellent starting point in the description of their electronic properties. We start with the description of a 1-D lattice, in which periodicity will lead to identical electronic densities at translationally equivalent points r and $r+ja$, where "a" is the translation vector and j is an integer. The phase relationship among the wavefunctions at periodically related points r and $r+ja$, is given by Bloch's theorem:

$$\Psi_k(r + ja) = e^{ikja}\Psi_k(r) \quad (2.34)$$

where e^{ikja} is referred to as the phase factor and k represents the electron wavevector in reciprocal space. We note that the electron wavevector has direct relation with the crystal momentum, i.e., $\mathbf{p}=\hbar k$. The translational vector ($G_{m_1m_2m_3}$) and lattice vectors ($\mathbf{a}^*, \mathbf{b}^*, \mathbf{c}^*$) in reciprocal space are defined as:

$$G_{m_1m_2m_3} = m_1\mathbf{a}^* + m_2\mathbf{b}^* + m_3\mathbf{c}^* \quad (2.35)$$

$$\mathbf{a}^* = \frac{2\pi(\mathbf{b} \times \mathbf{c})}{a \cdot (\mathbf{b} \times \mathbf{c})}, \mathbf{b}^* = \frac{2\pi(\mathbf{c} \times \mathbf{a})}{b \cdot (\mathbf{c} \times \mathbf{a})}, \mathbf{c}^* = \frac{2\pi(\mathbf{a} \times \mathbf{b})}{c \cdot (\mathbf{a} \times \mathbf{b})} \quad (2.36)$$

Similar to unit cells in a direct lattice, the reciprocal space also includes a primitive cell, referred to as a Wigner-Seitz cell. Within the framework of electronic-structure theory, these primitive cells are more commonly referred to as the first *Brillouin Zone* (BZ).

The crystal wavefunctions can be approximated via a *Tight-binding approach*. Here, the wavefunction is constructed from the superposition of basis set of orbitals occupying each site in the elementary cell (since the wavefunctions describe the properties of tightly bound electrons in the solid state, hence the name “*tight-binding*”). In this context, the electronic Hamiltonian can be represented as:

$$H = \sum_m \varepsilon_m b_m^\dagger b_m + \sum_{m \neq n} t_{mn} b_m^\dagger b_n \quad (2.37)$$

where ε_m corresponds to the electron site energy, t_{mn} represents the transfer integral between sites m and n , b_m^\dagger and b_m are the creation and annihilation operators at site m . We illustrate the application of the tight-binding approximation by considering a one-dimensional (1-D) periodic lattice. With the electronic Hamiltonian of Eq. (2.37) the crystal wavefunction would become:

$$\Psi_k(a) = \frac{1}{\sqrt{N}} \sum_a \phi(r - n_a a) e^{ikn_a a} \quad (2.38)$$

Here, “ a ” corresponds to the lattice spacing. The energetic dispersion in the 1-D case is then given by:

$$E(k)=E_0 - 2t\cos(ka) \quad (2.39)$$

where $E(k)$ represents the energy of a hole/electron with momentum k ; E_0 , the band center; t , the transfer integral between adjacent molecules along the stacking direction; and a , the lattice constant. The band structure represents the energetic dispersion associated with the orbitals as a function of wavevector k . Usually, the band structure in crystals is calculated between high-symmetry points in the first Brillouin zone. The bandwidth corresponds to the energy difference between the highest and lowest energy levels in the band and is related to the electronic coupling between adjacent sites. Within the tight binding model, the bandwidth is given by $W=2zt$, where z is the number of nearest neighbors and t represents the transfer integrals between the sites. In this context, we note that the term “valence band” in a band structure corresponds to the highest band of energy levels occupied by electrons. While the conduction band is formed from the lowest energy levels that are unoccupied.

2.2.2.6. *Effective Masses*

From the band structure, the energies at the highest value in the valence band and lowest value in the conduction band can be approximated as:

$$E(k) = \frac{\hbar^2 k^2}{2m^*} + E_0 \quad (2.40)$$

where the first term to the right in Equation (2.40) corresponds to kinetic energy and second term corresponds to a constant depicting the energy at the edge of that band. In classical terms, in the presence of an external field, the effective mass of a charge carrier is then defined as:

$$\left(\frac{1}{m^*}\right)_{i,j} = \frac{1}{\hbar^2} \frac{\partial^2 E_n(\vec{k})}{\partial k_i \partial k_j}, \quad i,j=x,y,z \quad (2.41)$$

where i and j denote the reciprocal components, m^* is the effective mass of the particle in terms of rest electron mass ($m_0=9.31 \times 10^{-31}\text{kg}$) and $E_n(k)$ represents the energy of the n^{th} band. We note

that the dispersion relation at the maximum or minimum of a band can often be taken as a parabola, which is given by:

$$E_n(\vec{k}) = a_1 k_x^2 + a_2 k_y^2 + a_3 k_z^2 \quad (2.42)$$

The components of the effective mass tensor are then the inverse of the components in front of the quadratic term in Equation (2.42). This is given by:

$$m_{xx}^* = \frac{\hbar}{2a_1}; m_{yy}^* = \frac{\hbar}{2a_2}; m_{zz}^* = \frac{\hbar}{2a_3} \quad (2.43)$$

However, in the case of organic semiconductors, it is not always possible to fit the band structure to the quadratic equation. Hence, in this case, the dispersion relation is analyzed numerically along different directions using the finite difference method. Here, the explicit form of the right side of Equation (2.41) is given by:

$$\frac{\partial^2 E}{\partial k^2} = \begin{pmatrix} \frac{\partial^2 E}{\partial k_x^2} & \frac{\partial^2 E}{\partial k_x k_y} & \frac{\partial^2 E}{\partial k_x k_z} \\ \frac{\partial^2 E}{\partial k_y k_x} & \frac{\partial^2 E}{\partial k_y^2} & \frac{\partial^2 E}{\partial k_y k_z} \\ \frac{\partial^2 E}{\partial k_z k_x} & \frac{\partial^2 E}{\partial k_z k_y} & \frac{\partial^2 E}{\partial k_z^2} \end{pmatrix} \quad (2.44)$$

In Equation (2.44), the second and mixed derivatives are evaluated on a five-point stencil method. To illustrate an example, in the case of a one-dimensional periodic lattice, the effective mass at the band edge is given by :

$$m^* = \frac{\hbar^2}{2ta^2} \quad (2.45)$$

2.2.2.7. Transfer Integrals (Electronic Couplings)

The transfer integrals (electronic couplings) are important parameters for describing the charge-transport properties in both the band regime and hopping regime. Based on the energy splitting in dimer (ESD) approach, the interaction between highest occupied molecular orbitals (HOMO's)

of monomers results in splitting of the order of twice the transfer integral ($2t_{AB}$) in a dimer AB, where A and B correspond to monomers and t_{AB} represents the transfer integral. Based on the one-electron approximation, for two monomers treated in an orthonormal basis, the transfer integrals are calculated as :

$$t = \frac{E_{H[L+1]} - E_{H-1[L]}}{2} \quad (2.46)$$

where $E_{H[L+1]}$ represents HUMO [LUMO+1] energies and $E_{H-1[L]}$ represents the HOMO-1[LUMO] energies of the corresponding monomers.¹⁵ To depict the cases where monomer orbitals are non-orthogonal, we apply the procedure described by Valeev et. al.¹⁸ Here, the orbital energies of the dimer are described by a secular equation:

$$\mathbf{HC} - \mathbf{ESC} = 0 \quad (2.47)$$

where H and S are the system Hamiltonian and overlap matrices, respectively. An essential component of this approximation is that the dimer HOMO and HOMO-1 are presumed to be formed only by the interaction of monomer HOMO's. Here, H and S are given by the matrices:

$$\mathbf{H} = \begin{pmatrix} e_1 & J_{12} \\ J_{12} & e_2 \end{pmatrix}, \text{ and,} \quad (2.48)$$

$$\mathbf{S} = \begin{pmatrix} 1 & S_{12} \\ S_{12} & 1 \end{pmatrix} \quad (2.49)$$

The matrix elements in Equation (2.48) are described by $e_i = \langle \Psi_i | \hat{H} | \Psi_i \rangle$ and $J_{ij} = \langle \Psi_i | \hat{H} | \Psi_j \rangle$. Valeev et. al.¹⁸ further applied Löwdin's symmetric transformation to convert the non-orthonormal monomer basis to an orthonormal basis.¹⁹ Equation (2.48) is then represented as:

$$H^{eff} = \begin{pmatrix} e_1^{eff} & J_{12}^{eff} \\ J_{12}^{eff} & e_2^{eff} \end{pmatrix} \quad (2.50)$$

where the matrix elements are obtained as:

$$e_{1(2)}^{eff} = \frac{1}{2} \frac{(e_1 + e_2) - 2J_{12}S_{12} \pm (e_1 - e_2)\sqrt{1 - S_{12}^2}}{1 - S_{12}^2} \text{ and} \quad (2.51)$$

$$J_{12}^{eff} = \frac{J_{12} - \frac{1}{2}(e_1 + e_2)S_{12}}{1 - S_{12}^2} \quad (2.52)$$

Based on this approach, the matrix elements $e_{1(2)}^{eff}$ and J_{12}^{eff} in Equations (2.51) and (2.52) have the same physical meaning as ε_m and t_{mn} in Equation (2.37). The resulting energetic splitting between the dimer HOMO and HOMO-1 can be expressed as:

$$\Delta E_{12} = \sqrt{(e_1^{eff} - e_2^{eff})^2 + (2J_{12}^{eff})^2} \quad (2.53)$$

This model can also be applied to systems where HOMO and LUMO energies are energetically well separated from HOMO-1 and LUMO+1, respectively.

2.3. Atomistic Molecular Dynamics

The morphological properties of materials systems based on polymers, small molecules, and their blends are of crucial importance to determine the charge and energy transport in organic electronic devices. In order to understand the impact of morphology formed by a large number of molecules, it is imperative to drastically reduce the number of electronic degrees of freedom. In this context, approximate methods like atomistic molecular dynamics (MD) simulations can be used to access realistic morphologies of large ensembles of molecules for pre-defined thermodynamic conditions. MD simulations employ force-fields to reproduce the molecular geometries and the molecules follow Newtonian dynamics for motion. Here, only the atomic nuclei are explicitly modelled as a series of points (atoms) connected by strings (bonds), and all the electronic parameters are contained implicitly within the force field. The final molecular organizations are then determined by following the trajectory of all atoms in time.

2.3.1. Force fields

Force fields represent the sum of equations with parameter sets that are used to calculate the potential energy of the system under consideration. Depending on the properties calculated, force fields are parameterized to replicate some experimental results. This is often done by performing quantum-chemical calculations of constituent molecules and by using empirical terms and fitting them to the functional form of the force field. The force field contains energy terms for both bonded and non-bonded interactions. In Chapters 3 and 4, we employ the OPLS-AA (optimized potential for liquid simulations- all atom) force field developed by Jorgensen and coworkers,²⁰ to simulate the bulk properties of materials. As in other force fields, OPLS-AA also includes terms for harmonic bond-stretching and angle bending, Fourier series terms for each torsional angle, and Coulomb and Lennard-Jones terms for intermolecular and intramolecular non-bonded interactions. The complete analytical form of the OPLS-AA force field is as below:

$$\begin{aligned}
 E_{\text{total}} &= E_{\text{bonds}} + E_{\text{angles}} + E_{\text{torsions}} + E_{\text{nonbonded}} \\
 E_{\text{bonds}} &= \sum_{\text{bonds}} K_r (r - r_{\text{eq}})^2 \\
 E_{\text{angles}} &= \sum_{\text{angles}} K_{\theta} (\theta - \theta_{\text{eq}})^2 \\
 E_{\text{torsions}} &= \sum_i \left\{ V_{0,i} + \frac{V_{1,i}}{2} (1 + \cos\phi_i) + \frac{V_{2,i}}{2} (1 - \cos 2\phi_i) + \frac{V_{3,i}}{2} (1 + \cos 3\phi_i) \right\} \\
 E_{\text{non-bonded}} &= \sum_i \sum_j \left\{ \frac{q_i q_j e^2}{r_{ij}} + 4\epsilon_{ij} \left[\left(\frac{\sigma_{ij}}{r_{ij}} \right)^{12} - \left(\frac{\sigma_{ij}}{r_{ij}} \right)^6 \right] \right\} \quad (2.54)
 \end{aligned}$$

To update the force field parameters for specific (macro) molecules, we performed DFT calculations at the ω B97XD/6-31G** level of theory. The bonds and angles were directly taken from the optimized structures. The dihedral parameters corresponding to inter-ring dihedrals were obtained by fitting the converged torsion profile calculated at the ω B97XD/6-31G** level of

theory. Unless otherwise noted, the partial atomic charges were obtained using the CHelpG method implemented in Gaussian 09.D01, which produces charges by fitting the electrostatic potential at points selected according to CHelpG scheme.²¹

2.3.2. Performing MD simulations

To run MD simulations, every system is initially described by a set of coordinates and momenta. As mentioned above, the dynamics of each particle is described by Newton's second law of motion:

$$\frac{\partial H}{\partial r} = \frac{\partial U}{\partial r} = -m \frac{\partial^2 r}{\partial t^2} \quad (2.55)$$

Equation (2.55) is integrated to compute positional coordinates, angular coordinates, and velocities of all atoms as a function of time, thereby generating the full trajectory of the system in phase space. The integration is performed along discrete time steps, which starts from initial positions and velocities for every particle at time t and finding the positions and velocities at an incremented time of $(t + \Delta t)$. Normally, this is carried out by using a Taylor expansion, where the new positions are described as;

$$r(t + \Delta t) = r(t) + \frac{\partial r}{\partial t} (\Delta t) + \frac{1}{2} \frac{\partial^2 r}{\partial t^2} (\Delta t)^2 + \dots \quad (2.56)$$

There are multiple algorithms that can perform this integration of Newton's equation of motion. In this work, we have used the Verlet algorithm to perform this crucial task, which performs the Taylor expansion with minimum of truncation error.²² This is achieved by carrying out the Taylor expansion in positive and negative increments of time steps and adding them together to obtain the new position. Since velocities are not explicitly calculated to find the new positions, they are approximated in this method. The time step for the Verlet integrator is kept sufficiently low to the order of ~ 1 fs in order to capture the vibrational motions of the bonds. The MD simulations we

have carried out are performed in the NPT ensemble (constant number of particles, N ; constant pressure, P ; and constant temperature, T), where the temperature and pressure controls were achieved using the Nosè-Hoover thermostat/barostat.²³⁻²⁶ A cut-off distance of 12 Å was used for summation of the van der Waals interactions and the particle-particle particle-mesh (PPPM) method²⁷ was used to calculate long-range Coulomb interactions.

The final output of MD simulations is the full trajectory of the system. Observable properties can then be reproduced or predicted from the average values at equilibrium of properties like densities, distributions of bonds, angles and dihedrals, or radial distribution functions, in the form of a time average from configurations along the overall simulation time. We note that while atomistic MD simulations can provide a good insight on the “local” morphology (as described in Chapter 1), methods like coarse-grain simulations are to be applied in order to investigate the “global” morphology within a device active layer. Since coarse-grain simulations do not form the focus of our work, we do not discuss this approach here.

2.4. Codes Used

All electronic-structure calculations within this dissertation are performed using the Gaussian 09.D01 software package.²⁸ All crystal structures were obtained from the Cambridge Crystallographic Database. The calculations of band structures and effective masses were performed, based on the experimental crystal structures with the Crystal 14²⁹ and Crystal 17³⁰ codes. Molecular Dynamics simulations were carried out with the LAMMPS package³¹ and OPLS-AA force-field.²⁰

2.5. References

1. Hohenberg, P.; Kohn, W., Inhomogeneous Electron Gas. *Physical Review* **1964**, *136* (3B), B864-B871.
2. Kohn, W.; Sham, L. J., Self-Consistent Equations Including Exchange and Correlation Effects. *Physical Review* **1965**, *140* (4A), A1133-A1138.
3. Perdew, J. P.; Schmidt, K., Jacob's ladder of density functional approximations for the exchange-correlation energy. *AIP Conference Proceedings* **2001**, *577* (1), 1-20.
4. Ceperley, D. M.; Alder, B. J., The low density phases of the electron gas. *J. Phys. Colloques* **1980**, *41* (C7), C7-295-C7-298.
5. Perdew, J. P.; Zunger, A., Self-interaction correction to density-functional approximations for many-electron systems. *Physical Review B* **1981**, *23* (10), 5048-5079.
6. Vosko, S. H.; Wilk, L.; Nusair, M., Accurate spin-dependent electron liquid correlation energies for local spin density calculations: a critical analysis. *Canadian Journal of Physics* **1980**, *58* (8), 1200-1211.
7. Perdew, J. P.; Burke, K.; Ernzerhof, M., Generalized Gradient Approximation Made Simple. *Physical Review Letters* **1996**, *77* (18), 3865-3868.
8. Becke, A. D., Density-functional exchange-energy approximation with correct asymptotic behavior. *Physical Review A* **1988**, *38* (6), 3098-3100.
9. Perdew, J. P.; Wang, Y., Accurate and simple analytic representation of the electron-gas correlation energy. *Physical Review B* **1992**, *45* (23), 13244-13249.
10. Lee, C.; Yang, W.; Parr, R. G., Development of the Colle-Salvetti correlation-energy formula into a functional of the electron density. *Physical Review B* **1988**, *37* (2), 785-789.
11. Becke, A. D., A new mixing of Hartree-Fock and local density-functional theories. *The Journal of Chemical Physics* **1993**, *98* (2), 1372-1377.
12. Becke, A. D., Density-functional thermochemistry. III. The role of exact exchange. *The Journal of Chemical Physics* **1993**, *98* (7), 5648-5652.
13. Chai, J.-D.; Head-Gordon, M., Systematic optimization of long-range corrected hybrid density functionals. *The Journal of Chemical Physics* **2008**, *128* (8), 084106.
14. Chai, J.-D.; Head-Gordon, M., Long-range corrected hybrid density functionals with damped atom-atom dispersion corrections. *Physical Chemistry Chemical Physics* **2008**, *10* (44), 6615-6620.
15. Koopmans, T., About the assignment of wave functions and eigenvalues to the individual electrons of an atom. *Physica* **1934**, *1* (1), 104-113.
16. Janak, J. F., Proof that $\partial E/\partial n = \epsilon$ in density-functional theory. *Physical Review B* **1978**, *18* (12), 7165-7168.
17. Sun, H.; Zhong, C.; Brédas, J.-L., Reliable Prediction with Tuned Range-Separated Functionals of the Singlet-Triplet Gap in Organic Emitters for Thermally Activated Delayed Fluorescence. *Journal of Chemical Theory and Computation* **2015**, *11* (8), 3851-3858.
18. Valeev, E. F.; Coropceanu, V.; da Silva Filho, D. A.; Salman, S.; Brédas, J.-L., Effect of Electronic Polarization on Charge-Transport Parameters in Molecular Organic Semiconductors. *Journal of the American Chemical Society* **2006**, *128* (30), 9882-9886.
19. Löwdin, P. O., On the Non-Orthogonality Problem Connected with the Use of Atomic Wave Functions in the Theory of Molecules and Crystals. *The Journal of Chemical Physics* **1950**, *18* (3), 365-375.

20. Jorgensen, W. L.; Maxwell, D. S.; Tirado-Rives, J., Development and Testing of the OPLS All-Atom Force Field on Conformational Energetics and Properties of Organic Liquids. *Journal of the American Chemical Society* **1996**, *118* (45), 11225-11236.
21. Breneman, C. M.; Wiberg, K. B., Determining atom-centered monopoles from molecular electrostatic potentials. The need for high sampling density in formamide conformational analysis. *Journal of Computational Chemistry* **1990**, *11* (3), 361-373.
22. Verlet, L., Computer "Experiments" on Classical Fluids. I. Thermodynamical Properties of Lennard-Jones Molecules. *Physical Review* **1967**, *159* (1), 98-103.
23. Hoover, W. G., Canonical dynamics: Equilibrium phase-space distributions. *Physical Review A* **1985**, *31* (3), 1695-1697.
24. Hoover, W. G., Constant-pressure equations of motion. *Physical Review A* **1986**, *34* (3), 2499-2500.
25. Nosé, S., A unified formulation of the constant temperature molecular dynamics methods. *The Journal of Chemical Physics* **1984**, *81* (1), 511-519.
26. Nosé, S., A molecular dynamics method for simulations in the canonical ensemble. *Molecular Physics* **1984**, *52* (2), 255-268.
27. Hockney, R. W.; Eastwood, J. W., *Computer simulation using particles*. Taylor & Francis, Inc.: **1988**; p 564.
28. Frisch, M. J.; Trucks, G. W.; Schlegel, H. B.; Scuseria, G. E.; Robb, M. A.; Cheeseman, J. R.; Scalmani, G.; Barone, V.; Mennucci, B.; Petersson, G. A.; Nakatsuji, H.; Caricato, M.; Li, X.; Hratchian, H. P.; Izmaylov, A. F.; Bloino, J.; Zheng, G.; Sonnenberg, J. L.; Hada, M.; Ehara, M.; Toyota, K.; Fukuda, R.; Hasegawa, J.; Ishida, M.; Nakajima, T.; Honda, Y.; Kitao, O.; Nakai, H.; Vreven, T.; Montgomery Jr., J. A.; Peralta, J. E.; Ogliaro, F.; Bearpark, M. J.; Heyd, J.; Brothers, E. N.; Kudin, K. N.; Staroverov, V. N.; Kobayashi, R.; Normand, J.; Raghavachari, K.; Rendell, A. P.; Burant, J. C.; Iyengar, S. S.; Tomasi, J.; Cossi, M.; Rega, N.; Millam, N. J.; Klene, M.; Knox, J. E.; Cross, J. B.; Bakken, V.; Adamo, C.; Jaramillo, J.; Gomperts, R.; Stratmann, R. E.; Yazyev, O.; Austin, A. J.; Cammi, R.; Pomelli, C.; Ochterski, J. W.; Martin, R. L.; Morokuma, K.; Zakrzewski, V. G.; Voth, G. A.; Salvador, P.; Dannenberg, J. J.; Dapprich, S.; Daniels, A. D.; Farkas, Ö.; Foresman, J. B.; Ortiz, J. V.; Cioslowski, J.; Fox, D. J., Gaussian 09, Revision D. 01, Gaussian, Inc.: Wallingford, CT **2009**.
29. Dovesi, R.; Orlando, R.; Erba, A.; Zicovich-Wilson, C. M.; Civalleri, B.; Casassa, S.; Maschio, L.; Ferrabone, M.; De La Pierre, M.; D'Arco, P.; Noël, Y.; Causà, M.; Rérat, M.; Kirtman, B., CRYSTAL14: A program for the ab initio investigation of crystalline solids. *International Journal of Quantum Chemistry* **2014**, *114* (19), 1287-1317.
30. Dovesi, R.; Erba, A.; Orlando, R.; Zicovich-Wilson, C. M.; Civalleri, B.; Maschio, L.; Rérat, M.; Casassa, S.; Baima, J.; Salustro, S.; Kirtman, B., Quantum-mechanical condensed matter simulations with CRYSTAL. *Wiley Interdisciplinary Reviews: Computational Molecular Science* **2018**, *8* (4), e1360.
31. Plimpton, S., Fast Parallel Algorithms for Short-Range Molecular Dynamics. *Journal of Computational Physics* **1995**, *117* (1), 1-19.

Chapter-3

Impact of solution temperature-dependent aggregation on the solid-state packing and electronic properties of polymers for organic photovoltaics

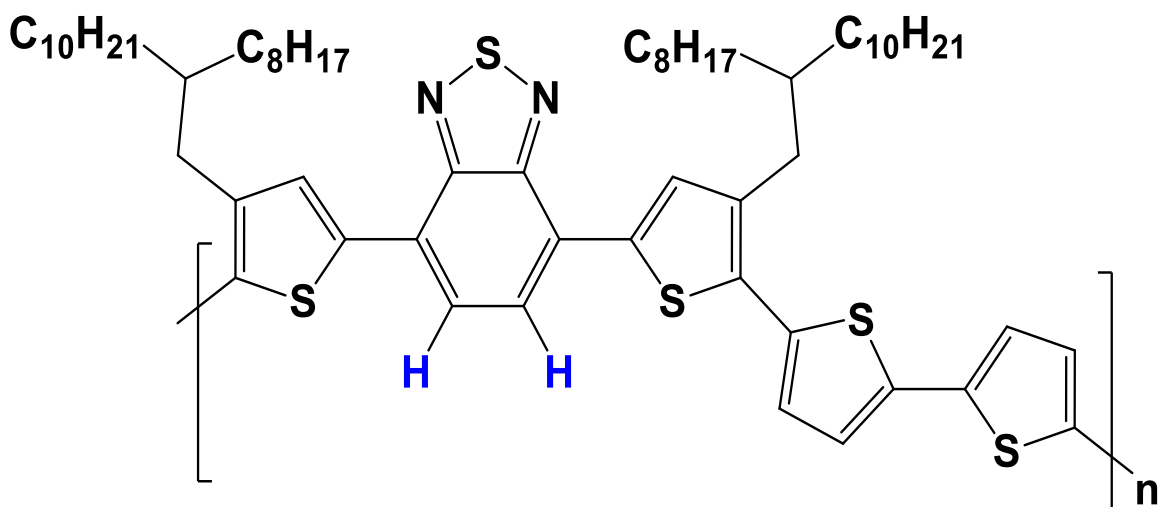
3.1 Introduction

As discussed in Chapter 1, improving the morphology characteristics of the active layer of an organic solar cell remains a crucial factor for obtaining higher device efficiencies. Significant efforts have been devoted experimentally to try and control the active-layer morphology via techniques including thermal or solvent annealing,¹⁻⁵ chemical substitution of the polymer donor and/or acceptor,³⁻¹³ using solvent additives,^{4, 5, 7, 14} and/or varying the donor:acceptor ratio in the active layer. Recently, Yan and co-workers demonstrated the successful exploitation of the solution temperature-dependent aggregation properties (TDA) of a series of polymers in achieving efficient morphology control.^{10, 11, 13} Temperature-dependent aggregation can be used to direct the polymers to form domains with optimal sizes of 20-40 nm, which is conducive to high device performance.

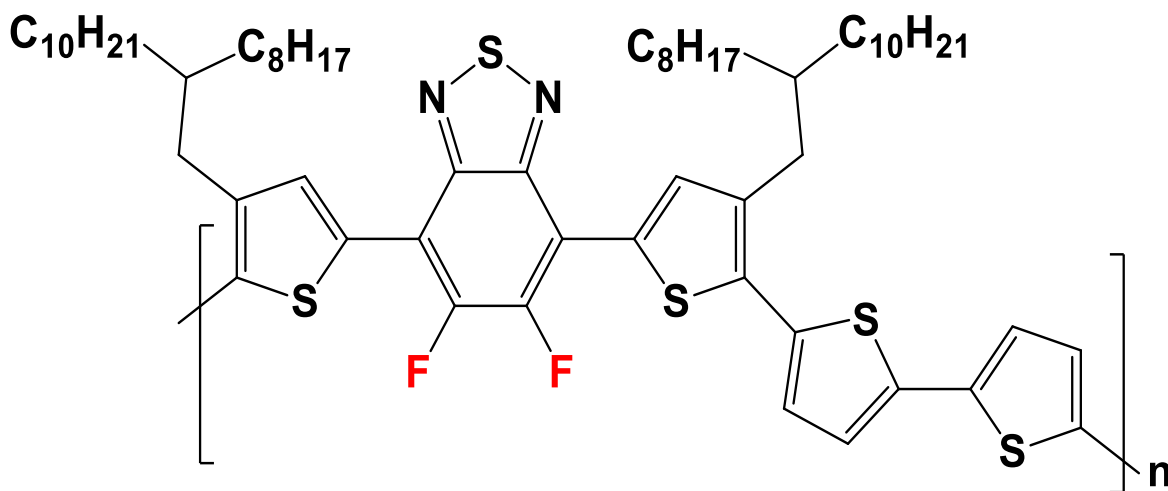
We note that most of the polymers displaying temperature-dependent aggregation properties have fluorine atoms along the polymer backbone.^{10, 11, 13} Interestingly, after removing these fluorine atoms, the TDA properties tend to disappear and, in this context, lower device efficiencies are observed. In some instances, the domain sizes for the non-fluorinated polymers in the active layer were found to be very large (up to ~100 nm). Also, up to four-fold differences in device efficiencies were observed between polymers with and without TDA properties. For example, in the cases of blends of PBT4T-2OD (poly[(2,1,3-benzothiadiazole-4,7-diyl)-*alt*-(3,3''-di(2-octyldodecyl)-

2,2';5',2'';5'',2'''-quarterthiophen-5,5'''-diyl)]) and PffBT4T-2OD (poly[(5,6-difluoro-2,1,3-benzothiadiazol-4,7-diyl)-*alt*-(3,3'''-di(2-octyldodecyl)-2,2';5',2'';5'',2'''-quarterthiophen-5,5'''-diyl)]) with phenyl-C71-butyric acid methyl ester (PC₇₁BM), the device efficiencies were measured to be 2.6% and 10.5%, respectively.^{11, 13} Thus, in order to gain a better understanding of the relationship between the active-layer morphology and efficiency, it is useful to connect the TDA properties of the polymer donors with the fluorination of the backbone, as well as to consider the impact of the TDA properties on the inter-chain packing at the molecular level.

In this context, we use a combination of molecular dynamics (MD) simulations and density functional theory (DFT) calculations to investigate the TDA properties of representative polymer donors and their impact on the formation of efficient morphologies and the nature of inter-chain packing. We choose the non-fluorinated polymer PBT4T-2OD and its difluorinated counterpart PffBT4T-2OD as model systems, see **Figure 3.1**. We start by discussing the results of MD simulations for the pure polymers in 1,2-dichlorobenzene solution at five different temperatures and characterize the differences in their extent of aggregation. We then rationalize these differences by analyzing the planarity of the PBT4T-2OD and PffBT4T-2OD backbones. Finally, we evaluate the impact of the temperature-dependent aggregation properties on the solid-state packing and electronic properties of the two polymers. This work has been published in *Journal of Materials Chemistry C*, **2018**, 6, 13162-13170.¹⁵



PBT4T-2OD



PffBT4T-2OD

Figure 3.1. Illustration of the chemical structures of the PBT4T-2OD and PffBT4T-2OD polymers with their chemical differences highlighted in blue and red.

3.2. Methodology

3.2.1. Molecular Dynamics Simulations

The MD simulations were performed¹⁶ with the LAMMPS package¹⁷ and based on the Optimized Potential for Liquid Simulations – All Atom (OPLS-AA) force field.¹⁸⁻²² The OPLS-AA force field, as described in detail in Chapter 2, was parameterized with bond lengths, bond angles, torsion angles, and atomic charges coming from PBT4T-2OD and PffBT4T-2OD oligomers optimized at the ω B97XD/6-31G(d,p) level of theory. The torsion potentials for specific dihedral angles were calculated on oligomers of increasing size until convergence was achieved. We note that the atomic partial charges were evaluated using the restricted electrostatic potential fitting scheme (RESP) at the ω B97XD/cc-PVTZ level of theory. We obtained good fitting of the force-field with the updated parameters, as described in our previous work.²³ Here, the RESP calculations were carried out with the Red software.²⁴

The initial models for the MD simulations were built by constructing polymer stacks (consisting of six polymer chains perfectly packed on top of each other) for both PBT4T-2OD and PffBT4T-2OD; each polymer chain has 6 repeat units (see representative example in **Figure 3.2**). The simulation boxes consisted of 152,448 atoms in total, including 12,226 1,2-dichlorobenzene (o-DCB) molecules. Here, the MD simulations were performed for both polymers at 100°C (for 50 ns), 80°C (for 80 ns), 60°C (for 120 ns), 40°C (for 200 ns) and 25°C (for 200 ns); in the latter case, the time scale of 200 ns represents the limit of our MD simulations while at 100°C, 80°C, and 60°C, the stacks nearly disaggregate into individual chains after 50 ns, 80 ns, and 120 ns, respectively.

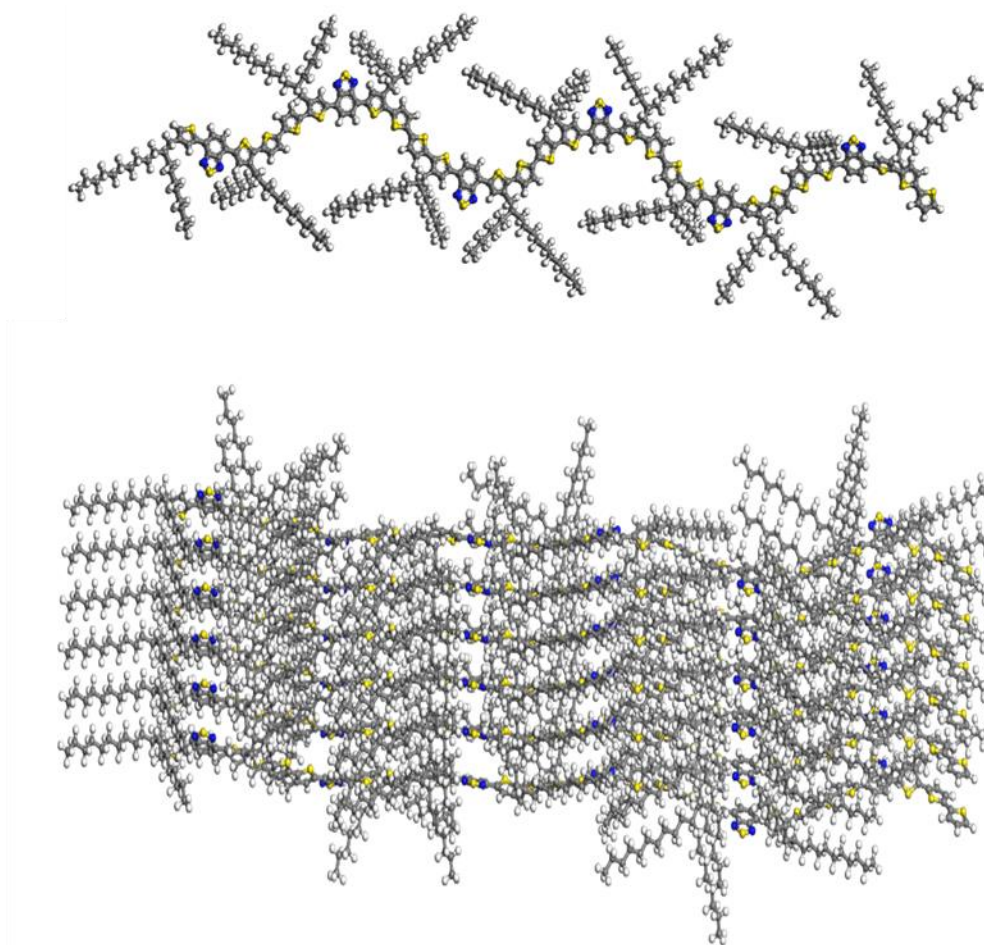


Figure 3.2. Illustration of the representative initial model used for the MD simulations: Top: A single polymer chain of PBT4T-2OD consisting of 6 repeat units. Bottom: A polymer stack made of 6 polymer chains perfectly packed on top of each other.

To examine more closely the planarity of individual chains, MD simulations were also carried out on single chains. The simulation box for the PBT4T-2OD polymer consisted of 87,440 atoms (one chain of PBT4T-2OD and 7,207 molecules of *o*-DCB) while that for the PffBT4T-2OD polymer contained 89,600 atoms (one chain of PffBT4T-2OD and 7,387 molecules of *o*-DCB). Here, the simulations were carried out at 25°C for 10 ns.

3.2.2. Density Functional Theory Calculations

All the DFT calculations were performed at the ω B97XD/6-31G(d,p) level of theory. In the framework of semi-classical Marcus theory, the electronic couplings (transfer integrals) among neighboring chains are a relevant figure of merit to describe at least qualitatively the charge-transport properties of the active layer.²⁵ The transfer integrals among sets of neighboring chains, *i.e.*, dimers extracted from MD simulation snapshots at different temperatures were calculated using a fragment orbital approach²⁶ combined with a basis set orthogonalization procedure. These calculations were performed with the Gaussian 09-D01 package.²⁷

Another useful parameter in determining the strength of interaction among polymer chains is their binding energy. A higher binding energy between specific chain segments implies a higher probability of presence of such interacting segments in the bulk phase of the active layer. In the evaluation of the binding energies, in order to prevent basis set superposition errors (BSSE), the counterpoise correction method proposed by Boys and Bernardi was applied.²⁸

3.3. Results and Discussion

3.3.1 Morphology of the Polymers in Solution

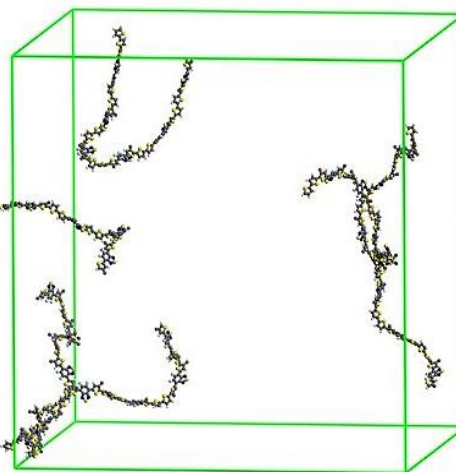
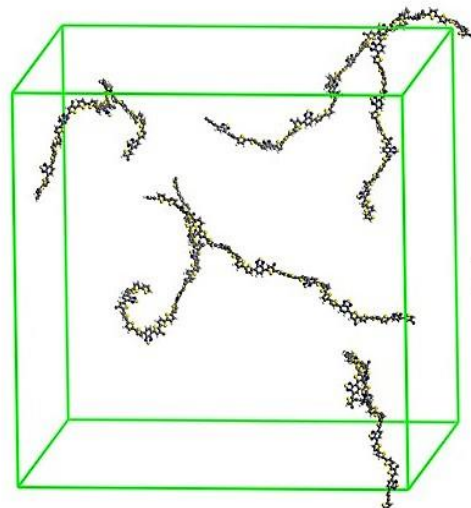
We first focus on the disaggregation of the polymer stacks as a function of time at five different temperatures representative of those used experimentally. The main results are as follows:

- For the PffBT4T-2OD and PBT4T-2OD stacks in solution at 100°C and 80°C disaggregation into individual chains takes place after 50 ns and 80 ns, respectively (see **Figure 3.3**).

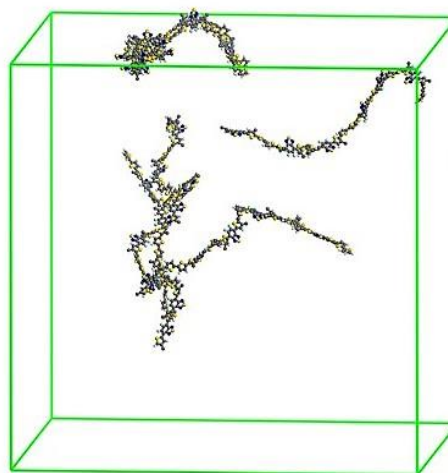
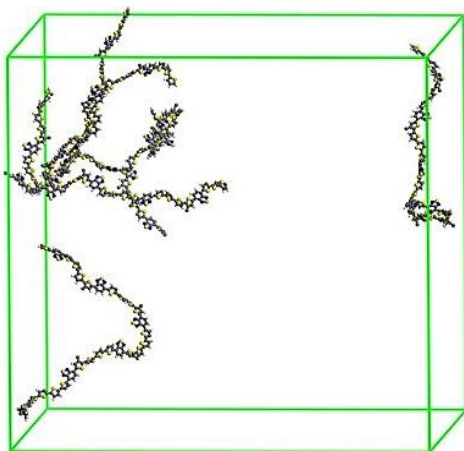
- At 60°C, while the PBT4T-2OD stack disaggregates into isolated polymer chains after 120 ns, the PffBT4T-2OD stack separates into a smaller stack containing 3 interacting chains and into three separated chains; interestingly, the smaller 3-chain PffBT4T-2OD stack keeps long-range order.
- At 40°C, the PBT4T-2OD stack starts to disaggregate along several sections after 200 ns; in contrast, the PffBT4T-2OD 6-chain stack begins to separate into two 4-chain and 2-chain stacks that clearly maintain overall shape and long-range order compared to the PBT4T-2OD case.
- The simulations at 25°C show trends similar to those at 40°C in both cases; after 200 ns, the PffBT4T-2OD stack has separated into two smaller 3-chain stacks that keep their pattern and long-range order, while the PBT4T-2OD stack is seen to disaggregate along several sections.

PBT4T-2OD

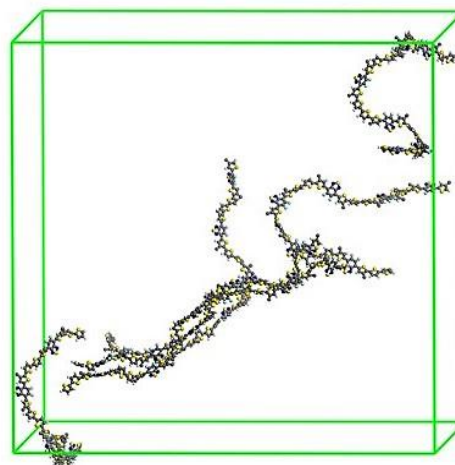
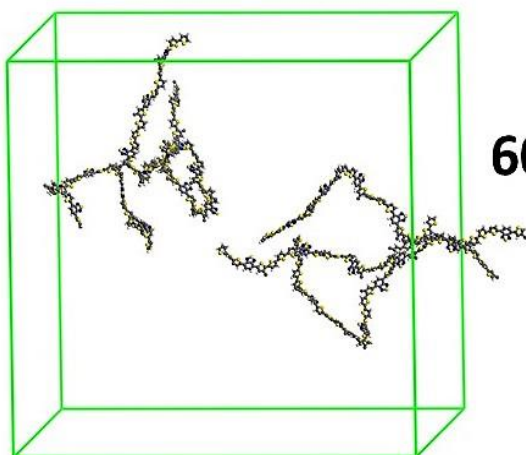
PffBT4T-2OD



100°C



80°C



60°C

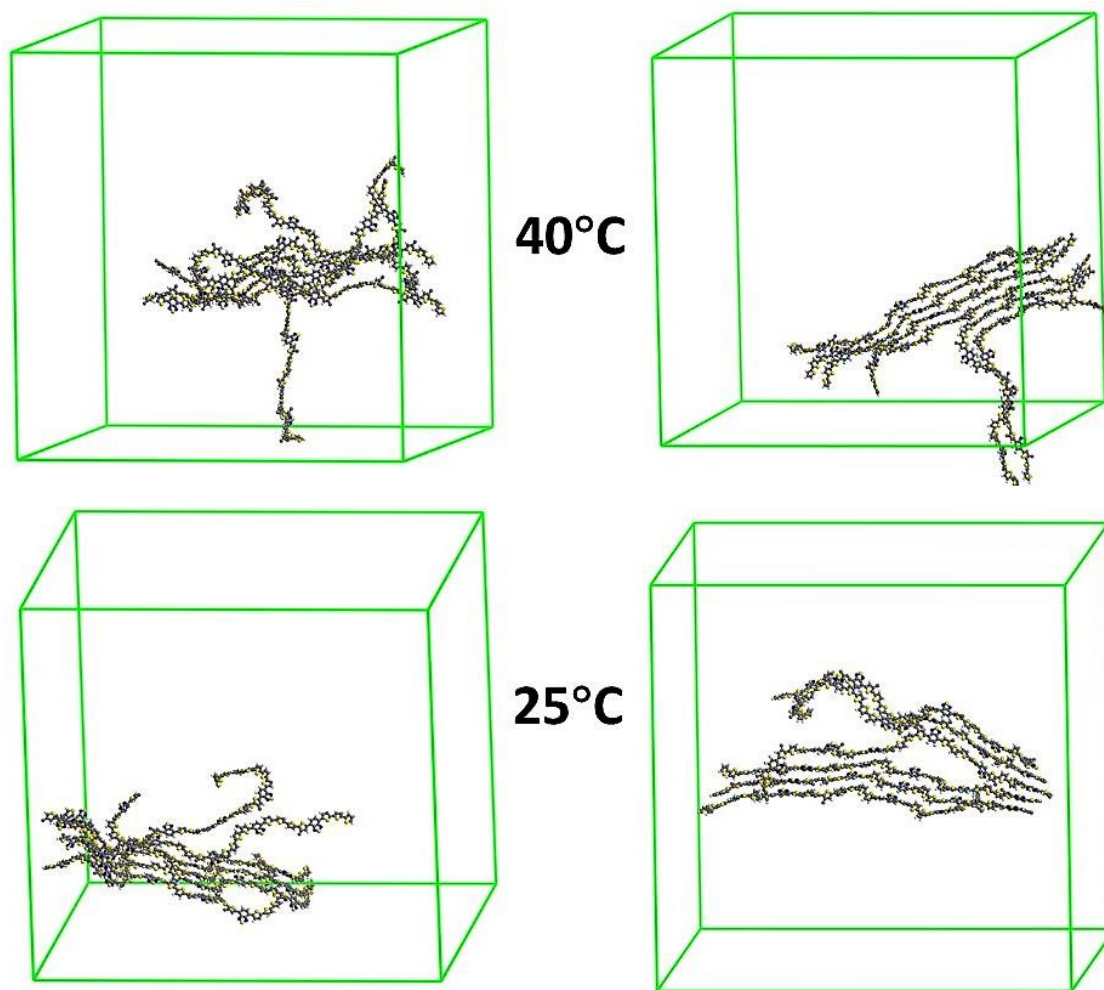


Figure 3.3. Snapshots from the MD simulations showing the extent of disaggregation of the six polymer chains present in the simulation box. The snapshots on the left and right correspond to PBT4T-2OD and PffBT4T-2OD, respectively; they are taken from simulations at 100°C (after 50 ns), 80°C (after 80 ns), 60°C (after 120 ns), 40°C (after 200 ns) and 25°C (after 200 ns).

The MD results are fully consistent with the experimental observations. Yan and co-workers indeed reported that PffBT4T-2OD chains aggregate when the solution is cooled down from 85°C to room temperature, while PBT4T-2OD chains do not present any aggregation under the same conditions.^{11, 13} The ability of the PffBT4T-2OD chains to stack at 25°C and 40°C can be attributed to an efficient chain packing in the aggregated state. This can be correlated with multiple observations that fluorination of the polymer backbone leads to more efficient π - π stacking in the

solid state.^{6, 8, 9, 12, 13, 29} We note that inter-chain H-F interactions could be a major driving force that leads to this effect in the PffBT4T-2OD polymer.³⁰ Since the PBT4T-2OD chains do not maintain any stacking configuration, be it at high or low solution temperatures, fluorination of the polymer backbone is confirmed as a crucial factor directing chain aggregation at low temperature.

The simulations at 25°C, 40°C, and 60°C reveal another major difference in the conformational behavior of the polymers. Unlike the PBT4T-2OD chains, the PffBT4T-2OD chains maintain long-range order throughout the simulations. Upon separation from the stack in solution, a PBT4T-2OD chain tends to bend, twist, and assume random conformations. Therefore, upon film casting during the evaporation of the solvent molecules, the PBT4T-2OD chains are expected to remain in their disordered conformations; this, in turn, will lead to the formation of large, uncontrolled amorphous domains that can limit charge separation and thus result in lower device performance. On the contrary, the fact that the PffBT4T-2OD chains can maintain packing and long-range order in solution, can translate into ordered domains in the solid state. Also, the low-temperature pre-aggregation of PffBT4T-2OD chains in solution allows the control of the eventual domain sizes in the solid state, via tuning of the solution temperature.

3.3.2 Distribution of Dihedral Angles along the Polymer Chains and Assessment of Co-Planarity

To compare the relative planarity between the PBT4T-2OD and PffBT4T-2OD chains, we analyzed the distributions of dihedral angles present along the polymer backbones. We evaluated these distributions based on 2,000 snapshots extracted from the final 10 nanoseconds of the MD simulations at each temperature.

We first discuss the dihedral-angle distributions for the polymer stacks in solution. Since the distributions turn out to be similar at the five temperatures, we only discuss the results obtained at 25°C. Three dihedral angles, depicted in **Figure 3.4**, have been chosen for this analysis. Dihedral **1** represents the torsion angle between the benzothiadiazole unit of the PBT4T-2OD polymer or di-fluoro-benzothiadiazole unit of the PffBT4T-2OD polymer and the thiophene unit on its right side. Dihedrals **2** and **3** represent the torsion angles between the two central and two external thiophenes of the quarterthiophene moieties.

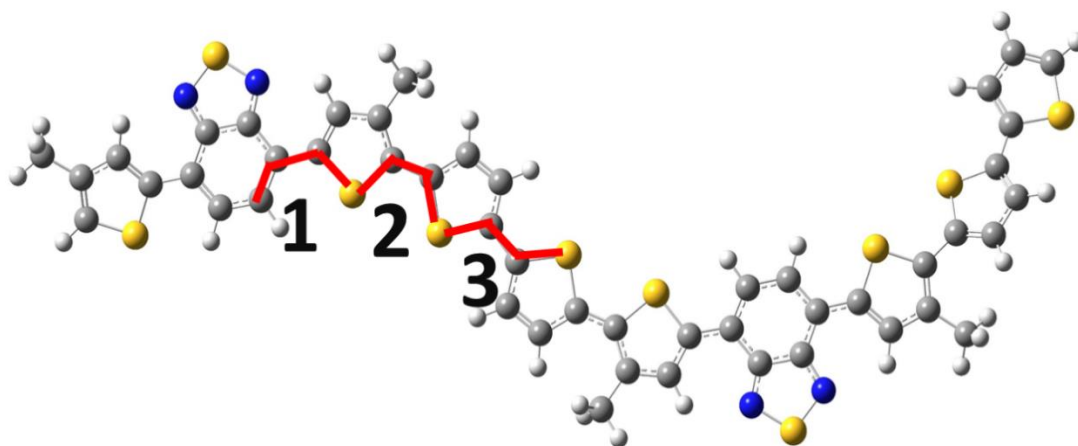
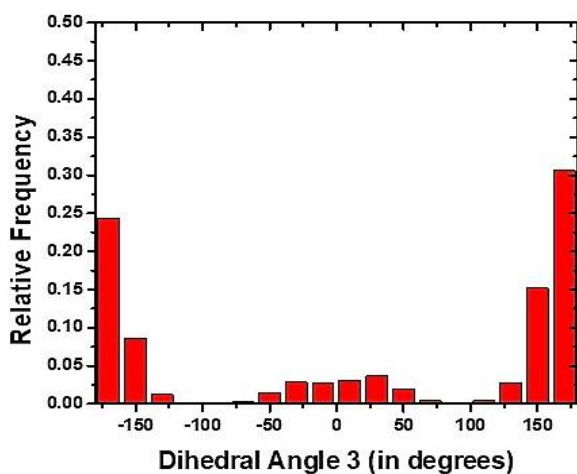
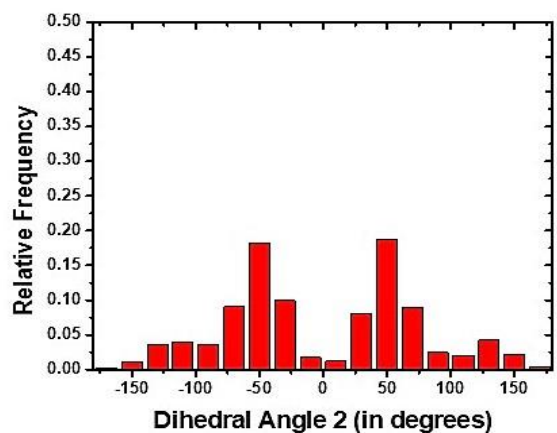
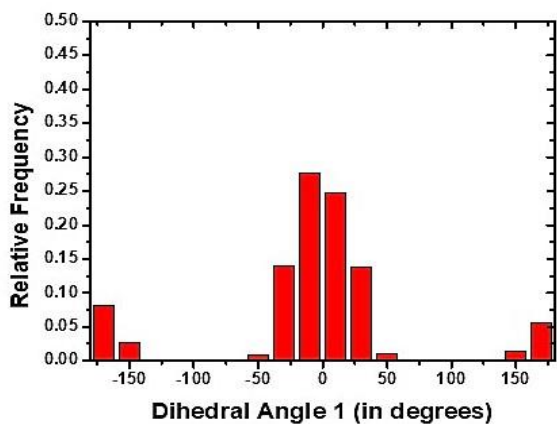


Figure 3.4. Illustration of the three dihedrals considered to analyze the distribution of dihedral angles.

A comparison of the dihedral distributions of both polymers reveals that, for dihedral angle **1**, there is a substantially higher relative frequency distribution of dihedral angles around $0^\circ \pm 50^\circ$ for PffBT4T-2OD as compared to PBT4T-2OD (see **Figure 3.5**). For dihedral angle **3**, PffBT4T-2OD has a strong distribution around $180^\circ \pm 50^\circ$ and a very limited distribution around $0^\circ \pm 50^\circ$, while PBT4T-2OD has a much narrower distribution around $+180^\circ$ and a broad distribution around $0^\circ \pm 50^\circ$. For dihedral angle **2**, largely similar distributions are found for both polymers.

PBT4T-2OD



PffBT4T-2OD

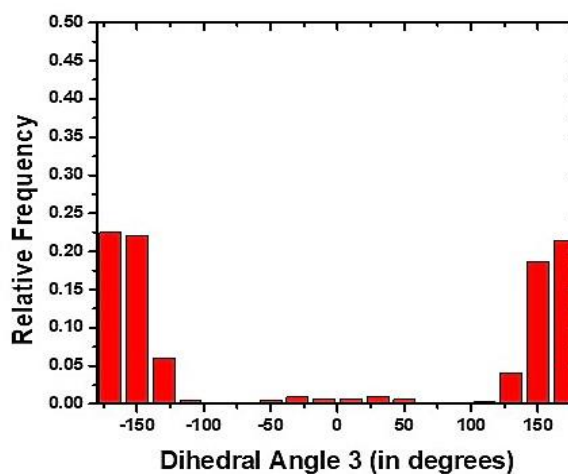
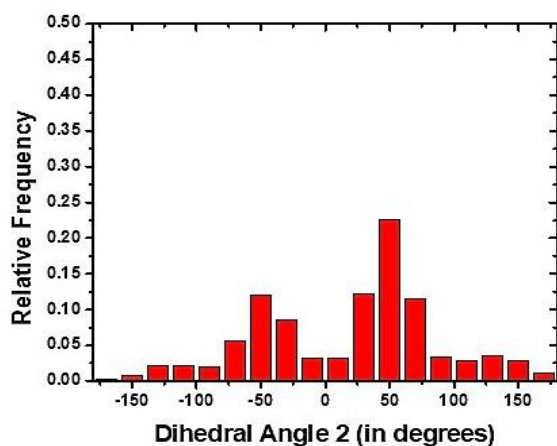
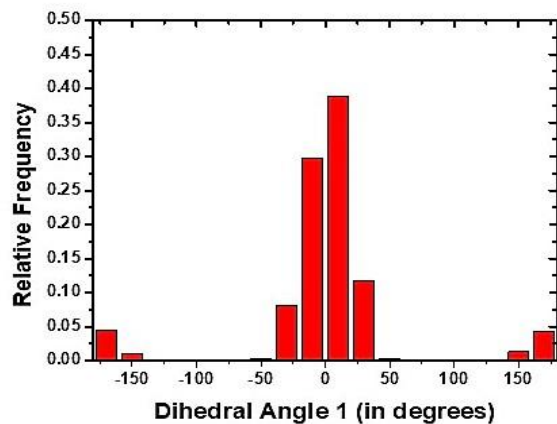
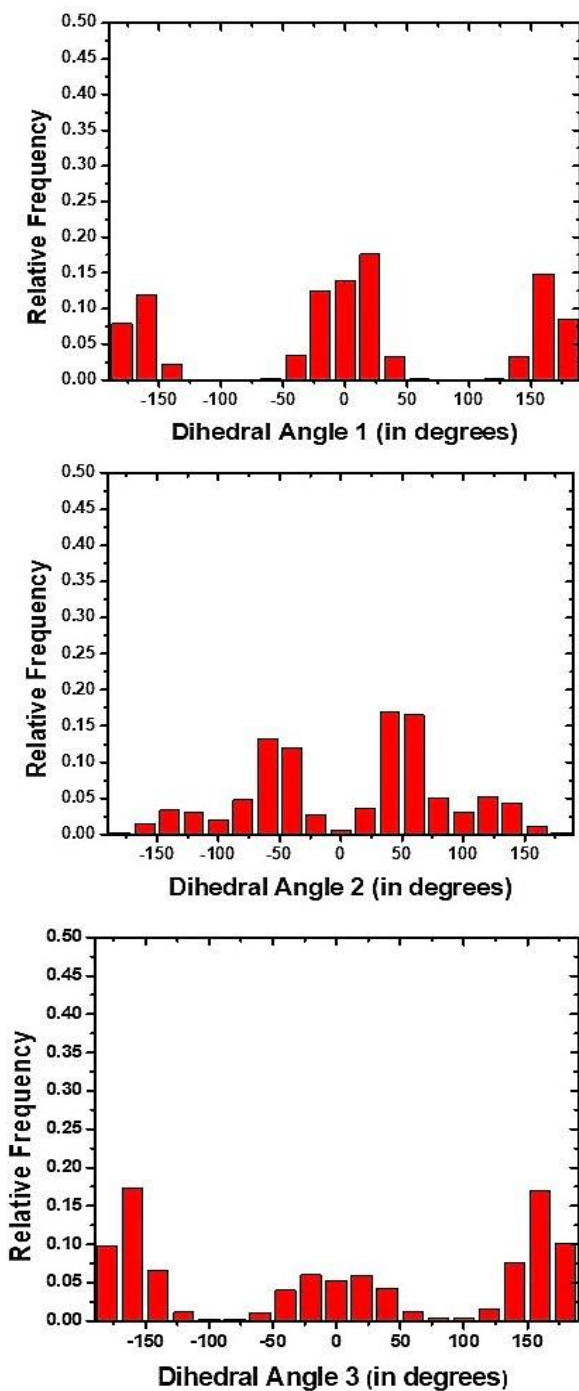


Figure 3.5. Distribution of dihedral angles along the PBT4T-2OD (left) and PffBT4T-2OD (right) chains after MD simulations of the respective polymer stacks in solution at 25°C.

PBT4T-2OD



PffBT4T-2OD

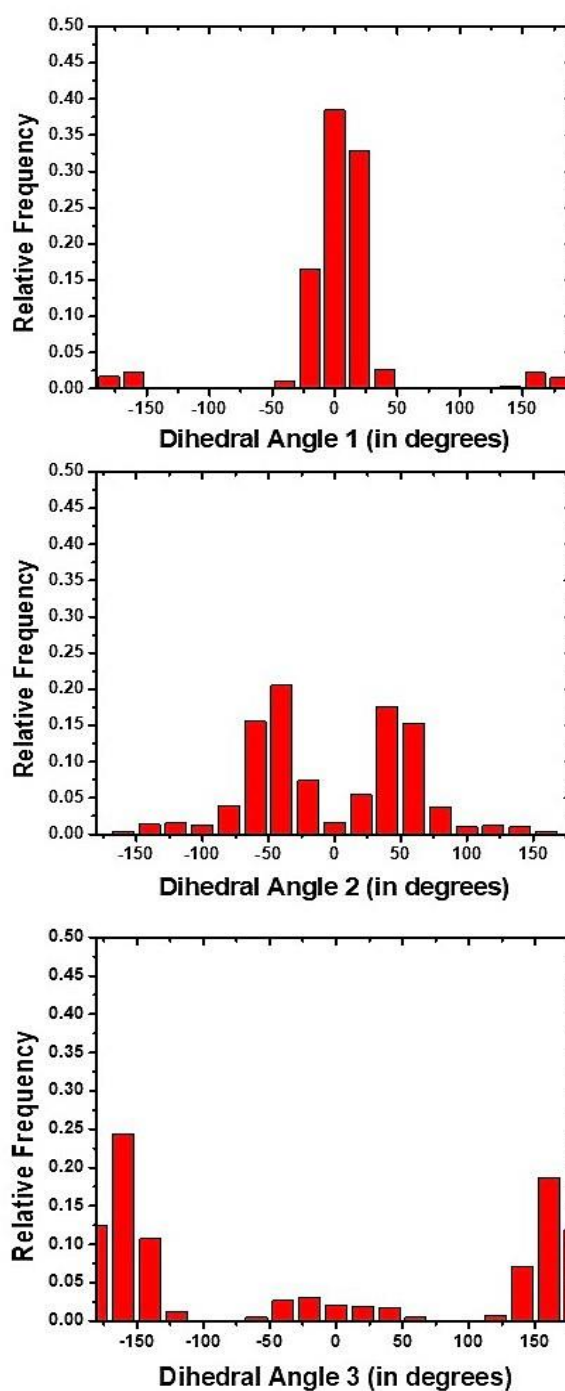
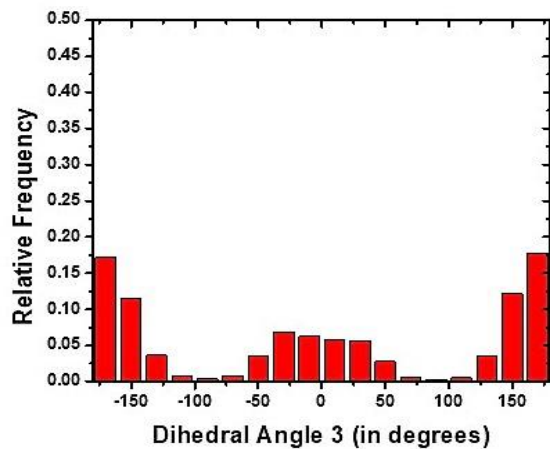
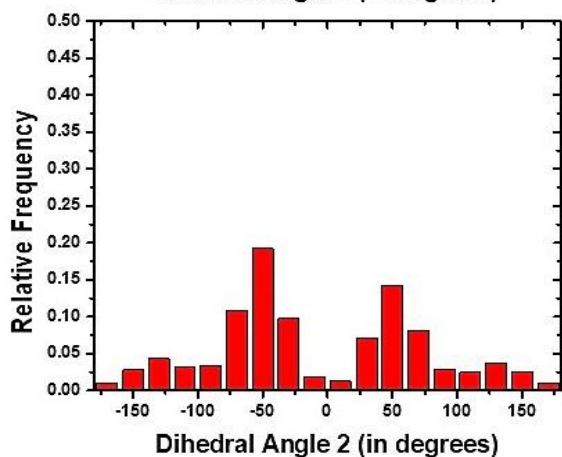
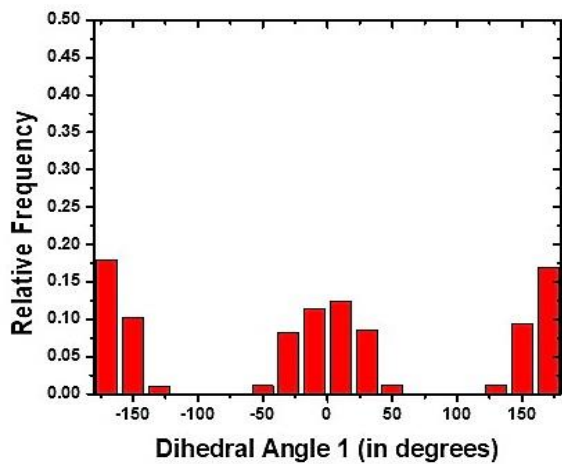


Figure 3.6. Distribution of the dihedral angles along the PBT4T-2OD (left) and PffBT4T-2OD (right) chains after MD simulations of the respective polymer stacks in solution at 40°C.

PBT4T-2OD



PffBT4T-2OD

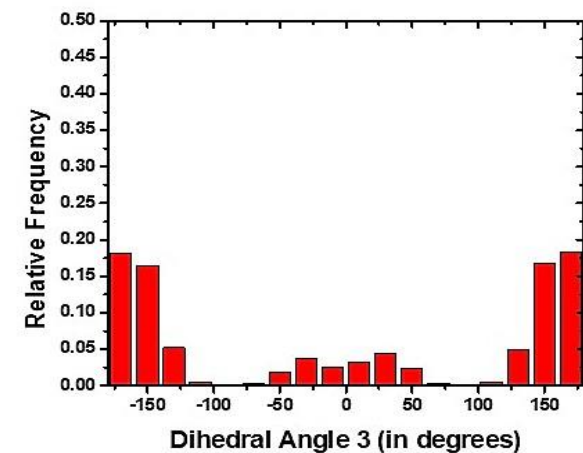
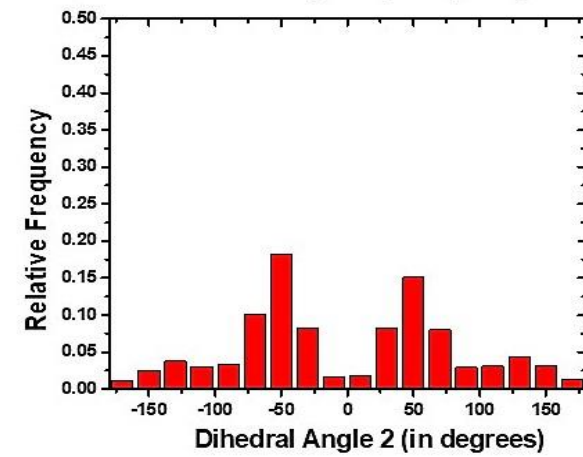
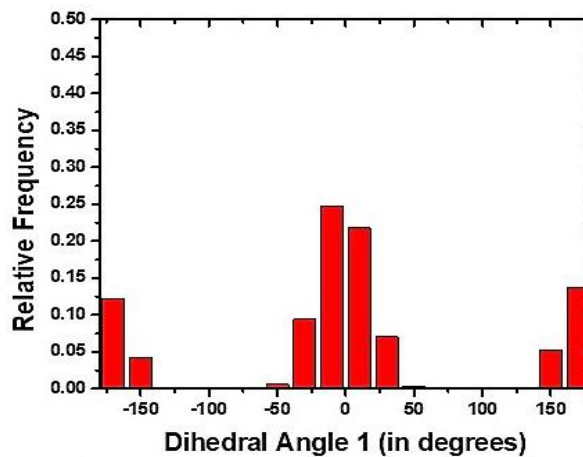
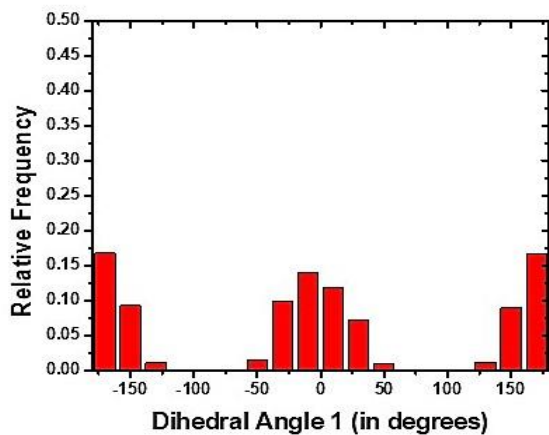


Figure 3.7. Distribution of the dihedral angles along the PBT4T-2OD (left) and PffBT4T-2OD (right) chains after MD simulations of the respective polymer stacks in solution at 60°C.

PBT4T-2OD



PffBT4T-2OD

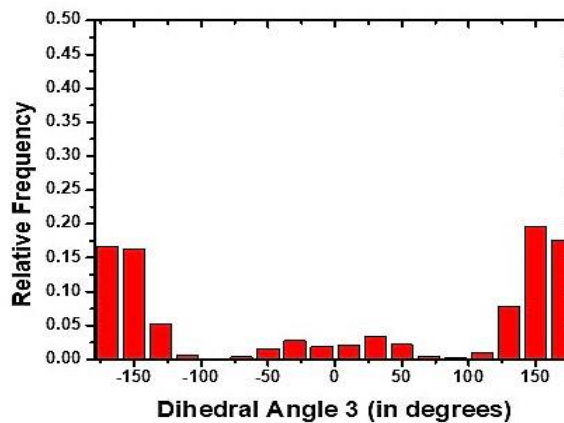
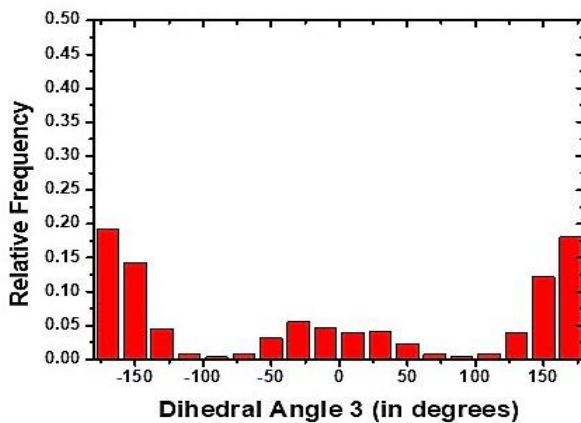
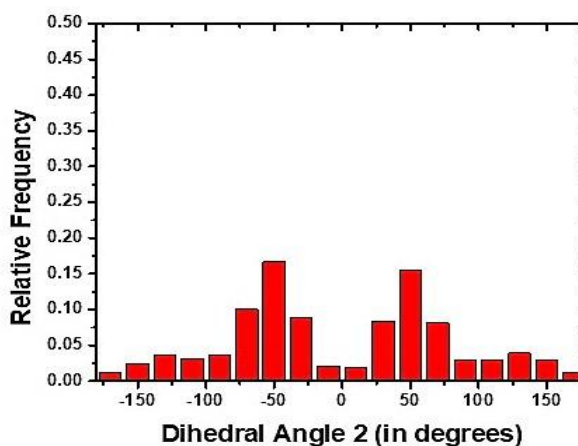
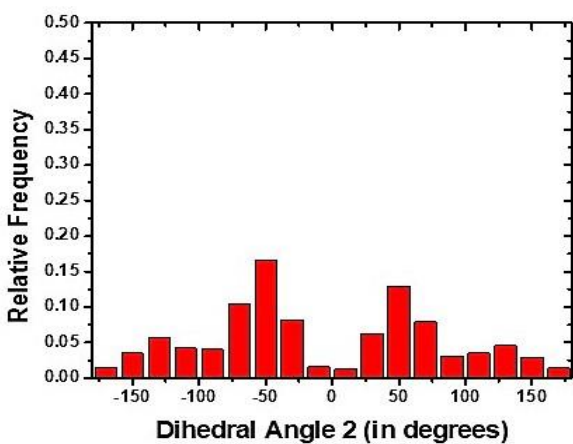
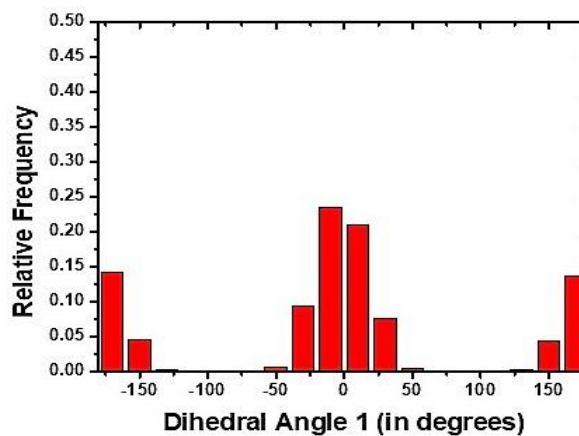
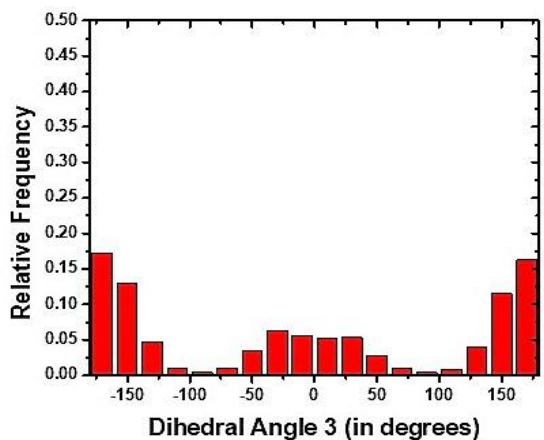
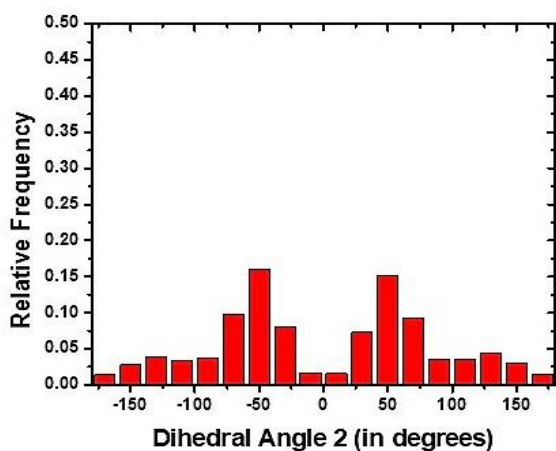
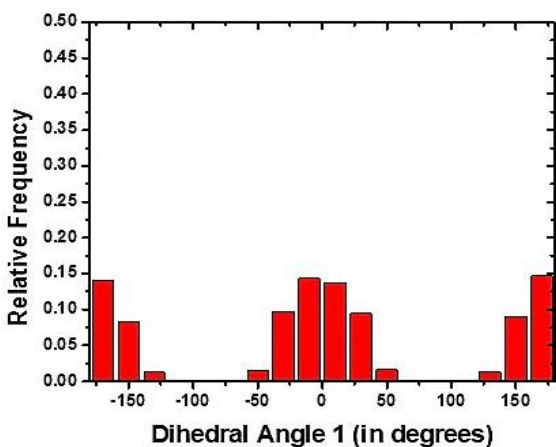


Figure 3.8. Distribution of the dihedral angles along the PBT4T-2OD (left) and PffBT4T-2OD (right) chains after MD simulations of the respective polymer stacks in solution at 80°C.

PBT4T-2OD



PffBT4T-2OD

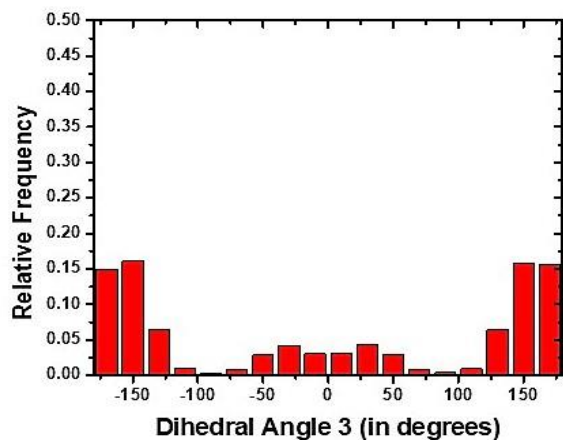
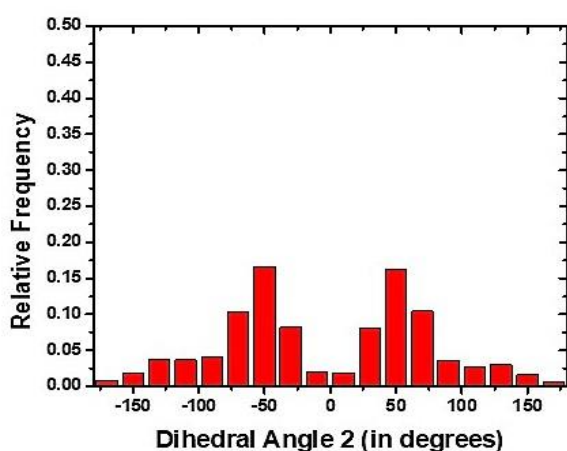
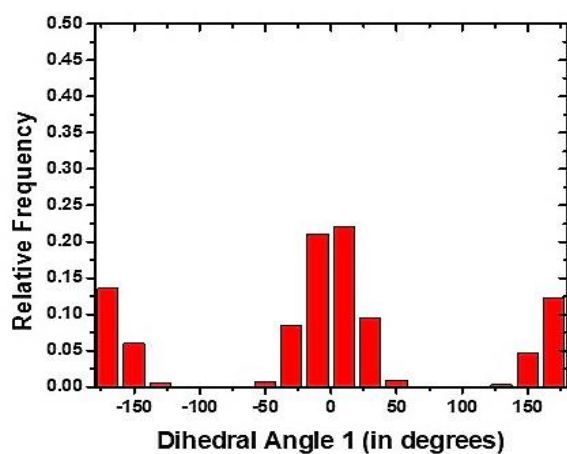
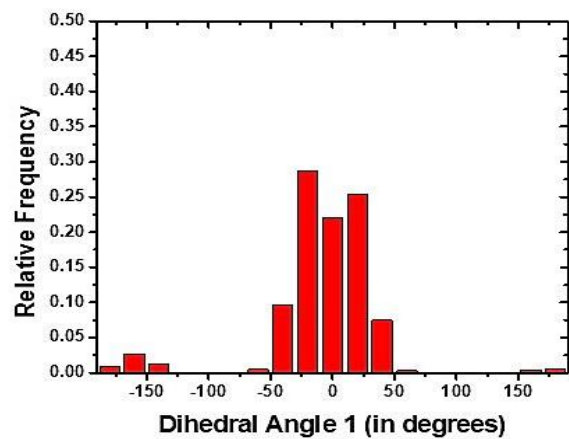


Figure 3.9. Distribution of the dihedral angles along the PBT4T-2OD (left) and PffBT4T-2OD (right) chains after MD simulations of the respective polymer stacks in solution at 100°C.

The results for dihedral angles **1** and **3** confirm that the PffBT4T-2OD polymer chains tend to be more planar as compared to the PBT4T-2OD polymer. As shown in **Figures 3.6-3.9**, these trends in dihedral-angle distributions are found to be similar at all the other temperatures. Since the side chains are the same on both polymers, their impact in determining the final stable conformations of both polymer chains is expected to be nearly identical.²³ With the only difference between the two polymers being the presence or absence of fluorine atoms in the polymer backbone, it is clear that the tendency of PffBT4T-2OD to remain more co-planar can be mainly ascribed to the backbone fluorination itself.

We also evaluated the dihedral-angle distributions of single polymer chains in o-DCB solution. Here, a single PBT4T-2OD/PffBT4T-2OD chain consisting of 6 repeat units was placed in solution; the simulations ran for 10 ns. Interestingly, we find similar trends for the distributions of all three dihedral angles, see **Figure 3.10**. This result underlines that neither the solvent nor the effect of inter-chain interactions plays a significant role in determining the planarity of the PffBT4T-2OD chains. Thus, it is an intrinsic property of the PffBT4T-2OD chains to remain more co-planar in comparison to PBT4T-2OD chains.

PBT4T-2OD



PffBT4T-2OD

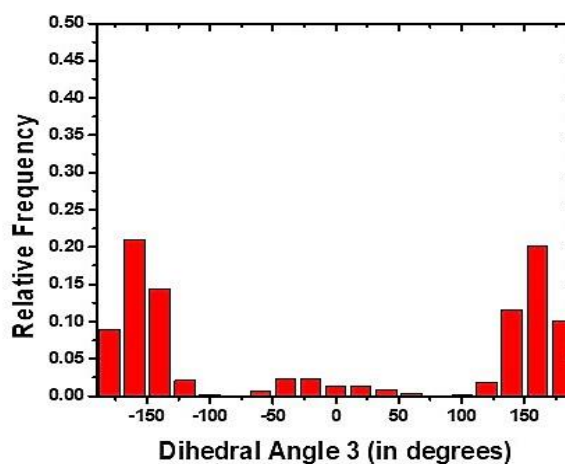
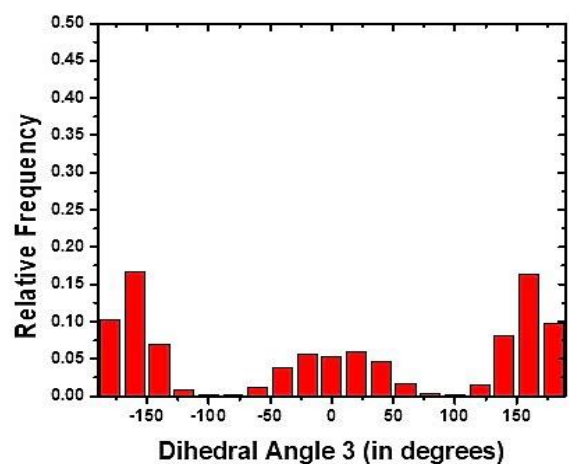
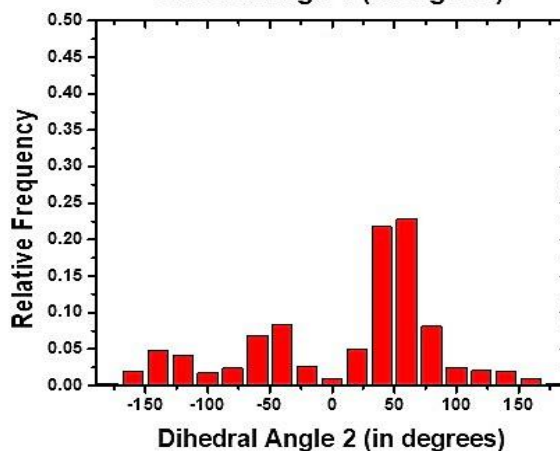
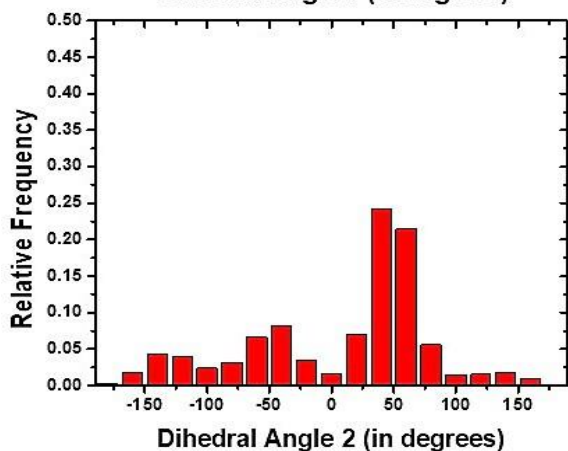
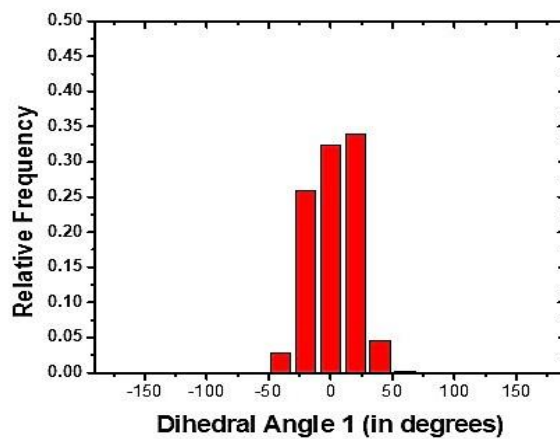


Figure 3.10. Distribution of dihedral angles along the PBT4T-2OD (left) and PffBT4T-2OD (right) chains after MD simulations of single polymer chains in *o*-DCB solution at 25°C.

3.3.3. Interaction Energies and Their Effect on Morphology

A way to quantify the strength of the inter-chain interactions is to consider the binding energies (interaction energies). We first evaluated the inter-chain binding energies for DFT-optimized PBT4T-2OD and PffBT4T-2OD dimers, where a dimer consists of two well-packed polymer chains with each chain containing two repeat units (see **Table 3.1**). A difference of *ca.* 2 kcal/mol is calculated between the PffBT4T-2OD and PBT4T-2OD cases, which thus translates into *ca.* 1 kcal/mol per repeat unit.

Table 3.1: Binding energies between two perfectly stacked dimer units, as calculated at the ω B97XD/6-31G** level of theory. A negative value indicates an attractive interaction.

Polymer	Binding Energy (in kcal/mol)
PBT4T-2OD	-56.7
PffBT4T-2OD	-58.6

We then estimated the binding energies between adjacent polymer chains extracted from the MD simulations of the polymer stacks in solution. Two chains in close proximity, consisting each of six repeat units, are taken as a dimer; thus overall, given six polymer chains, a maximum of five dimers can be present at any temperature. We note that at the higher temperatures of 80°C and 100°C, for which the polymer stacks disaggregate into individual chains, only the binding energies between chains that are somewhat close ($<5\text{\AA}$) are evaluated.

The binding energies between PffBT4T-2OD chains are found to be significantly larger than those between PBT4T-2OD chains (see **Table 3.2**). This is consistent with the fact that the simulations at lower temperatures, *e.g.*, at 25°C and 40°C, indicate that the PffBT4T-2OD chains remains better

packed with longer-range order as compared to the PBT4T-2OD chains. Thus, adjacent PffBT4T-2OD chains have a longer interaction length. Considering the small difference in binding energy per repeat unit that we found between PffBT4T-2OD and PBT4T-2OD dimers, it is the longer interaction length between the PffBT4T-2OD chains, and not the fluorination-induced increase in binding energy, that is mainly responsible for the significantly higher binding energies. Also, we note that the highest magnitude of binding energy for the PffBT4T-2OD chains is obtained at 25°C, which correlates well with the largest extent of aggregation observed at that temperature.

Table 3.2: Binding energies between two adjacent polymer chains, as calculated at the ω B97XD/6-31G** level of theory. A negative value indicates an attractive interaction.

Polymer	Dimer	Binding Energy (kcal/mol)				
		25 °C	40 °C	60 °C	80 °C	100 °C
PBT4T-2OD	1	-99.7	-62.7	-25.4	-49.9	0
	2	-63.8	-49.0	0	0	0
	3	-50.6	-41.5	0	0	0
	4	-40.8	-23.1	-	-	-
	5	-	-18.2	-	-	-
PffBT4T-2OD	1	-120.5	-100.1	-87.9	-81.3	0
	2	-64.7	-89.3	0.0	-33.4	0
	3	-54.5	-87.9	0.0	0	0
	4	-2.2	-75.1	-	-	-
	5	-	-23.9	-	-	-

3.3.4. Electronic coupling

The electronic couplings (transfer integrals) are important parameters in the description of the charge-transport characteristics. As discussed above, the fact that the aggregation behavior and long-range packing order found in solution are expected to maintain in the solid state, means that the electronic couplings for the chains in solution will be representative of the situation in the active layer.

Thus, we have evaluated the electronic couplings between adjacent PBT4T-2OD chains and PffBT4T-2OD chains extracted from the MD simulations of the polymer stacks in solution. The DFT calculations show that the highest occupied molecular orbitals (HOMOs) of both polymers delocalize across about two repeat units along the polymer backbone. (see **Figure 3.11**)

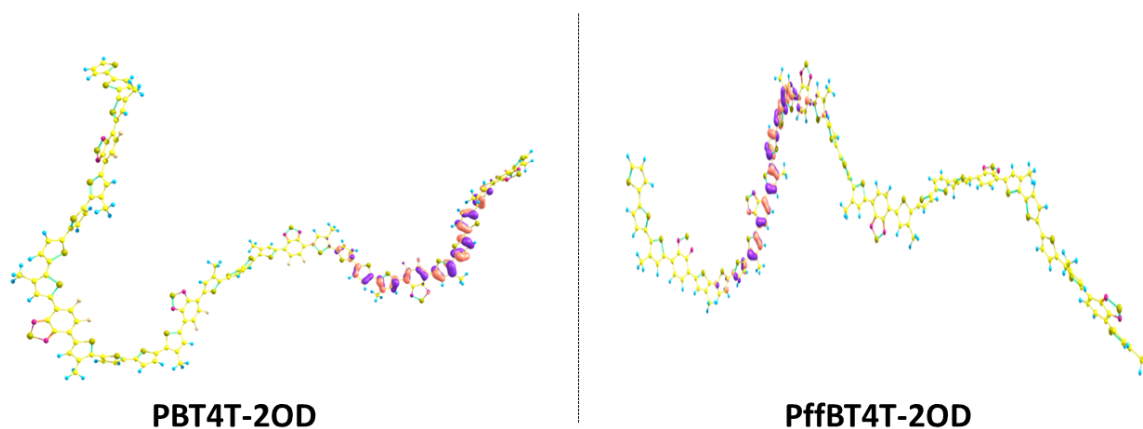


Figure 3.11. HOMOs of PBT4T-2OD and PffBT4T-2OD, as calculated at the ω B97XD/6-31G** level of theory

For that reason, each chain (6 repeat-unit long) was cut into 3 segments of two repeat units each; the HOMO-HOMO electronic couplings were then calculated between these segments (see **Figure 3.12**). We note that: (i) the electronic couplings between segments with intermolecular distances

larger than 5\AA are not evaluated since there is no effective wave-function overlap between such distant segments; and (ii) we only consider electronic couplings between HOMO levels since the polymers are hole transporters in the active layer.

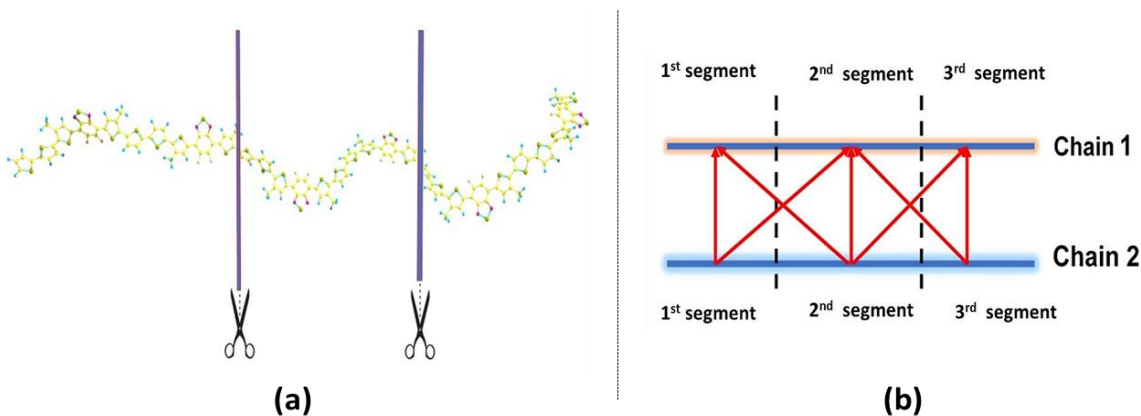


Figure 3.12. Illustration of (a) the cut of a polymer chain with six repeat units into segments of two repeat units each, (b) the protocol for the calculation of the electronic couplings between adjacent chains. The electronic couplings between the segments connected by arrows are the only ones considered for this work.

At all solution temperatures (except 100°C), the HOMO-HOMO couplings between PffBT4T-2OD segments are found to be consistently larger in comparison to the PBT4T-2OD case, see **Figure 3.13**. We note that, at higher solution temperatures, the polymer segments separate and, consequently, there are very few interacting segments at 60°C and 80°C . At 100°C , the polymer stacks are totally separated into individual chains and no interacting segments can be found within the threshold distance of 5\AA .

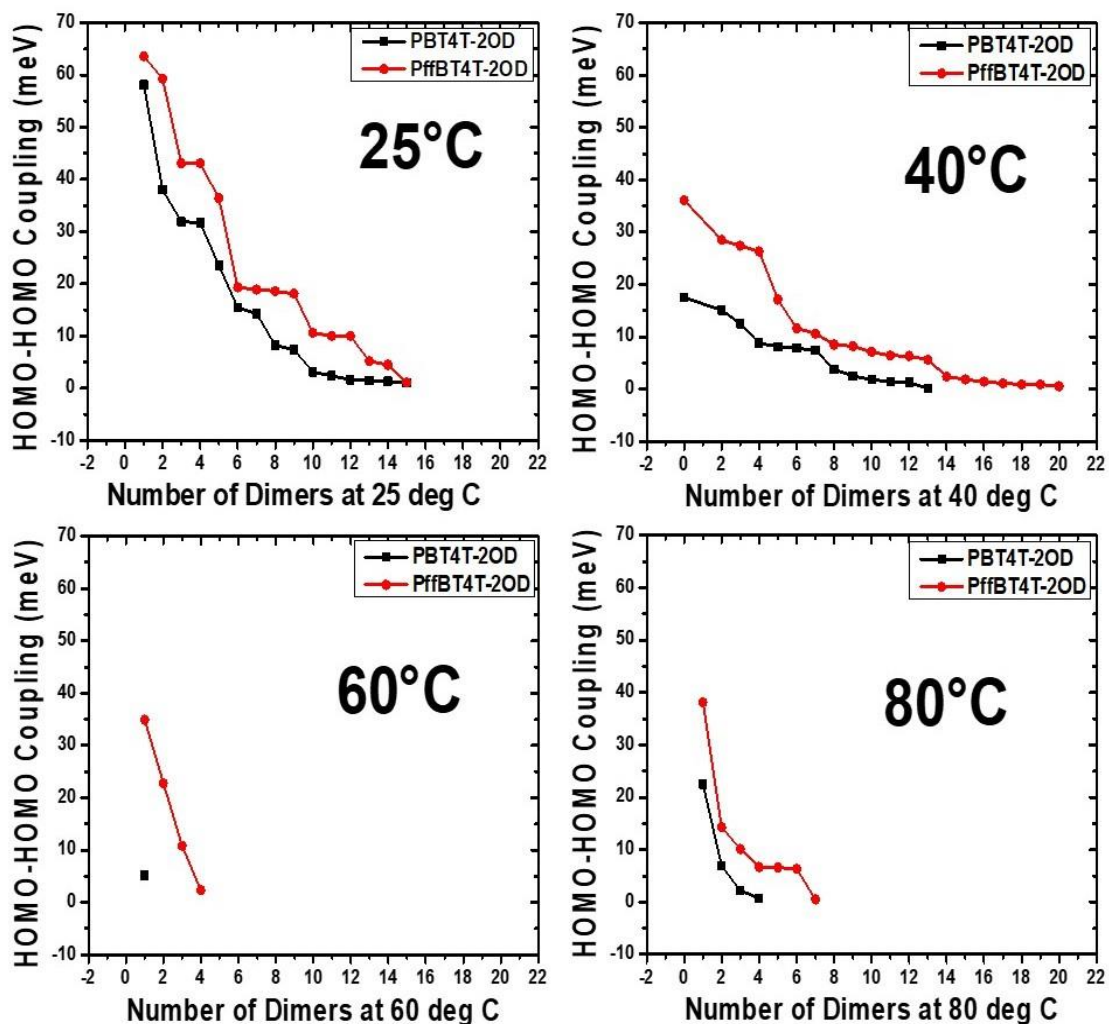


Figure 3.13. Electronic couplings between segments of the PBT4T-2OD and PffBT4T-2OD chains at 25°C, 40°C, 60°C and 80°C.

Overall, our investigations give useful insights that allow us to correlate the nature of the interactions in both polymers with the experimental results. The PffBT4T-2OD chains are observed experimentally to aggregate in solution at lower temperatures;^{11, 13} our MD simulations also show this pre-aggregation behavior as the PffBT4T-2OD stacks hold together at lower temperatures. The PffBT4T-2OD chains display better planarity, more efficient packing, and longer-range order in the stacks, leading to more efficient wave-function overlap between the chains; accordingly, we

calculate higher electronic couplings among PffBT4T-2OD segments as compared to the PBT4T-2OD case.

3.4. Conclusions

Our investigations on the effects of temperature-dependent aggregation on the solid-state packing and electronic properties of two representative polymers, PBT4T-2OD and PffBT4T-2OD, reveals that fluorination of the polymer backbone plays a key role in keeping the PffBT4T-2OD chains more co-planar than the PBT4T-2OD chains. The planarity of the polymer backbones in turn facilitates a longer interaction length between the polymer chains, as a result of which the PffBT4T-2OD chains remain well-packed in the stacks. These combined effects lead to easier pre-aggregation of the PffBT4T-2OD chains in solution.

Upon film formation, the solvent molecules evaporate; the well-aggregated nature of the PffBT4T-2OD chains is expected to maintain in the solid state, which leads to adequate size morphologies in the active layer. This can contribute to efficient exciton diffusion and hole transport within the PffBT4T-2OD domains, and ultimately lead to higher device efficiency. The exploitation of the temperature-dependent aggregation properties thus represents an effective tool to control the morphology of the active layers.

3.5. References

1. Lu, L.; Zheng, T.; Wu, Q.; Schneider, A. M.; Zhao, D.; Yu, L., Recent Advances in Bulk Heterojunction Polymer Solar Cells. *Chemical Reviews* **2015**, *115* (23), 12666-12731.
2. Brabec, C. J.; Heeney, M.; McCulloch, I.; Nelson, J., Influence of blend microstructure on bulk heterojunction organic photovoltaic performance. *Chemical Society Reviews* **2011**, *40* (3), 1185-1199.
3. Cates, N. C.; Gysel, R.; Beiley, Z.; Miller, C. E.; Toney, M. F.; Heeney, M.; McCulloch, I.; McGehee, M. D., Tuning the Properties of Polymer Bulk Heterojunction Solar Cells by Adjusting Fullerene Size to Control Intercalation. *Nano Letters* **2009**, *9* (12), 4153-4157.
4. Piliago, C.; Holcombe, T. W.; Douglas, J. D.; Woo, C. H.; Beaujuge, P. M.; Fréchet, J. M. J., Synthetic Control of Structural Order in N-Alkylthieno[3,4-c]pyrrole-4,6-dione-Based Polymers for Efficient Solar Cells. *Journal of the American Chemical Society* **2010**, *132* (22), 7595-7597.
5. Li, Z.; Tsang, S.-W.; Du, X.; Scoles, L.; Robertson, G.; Zhang, Y.; Toll, F.; Tao, Y.; Lu, J.; Ding, J., Alternating Copolymers of Cyclopenta[2,1-b;3,4-b']dithiophene and Thieno[3,4-c]pyrrole-4,6-dione for High-Performance Polymer Solar Cells. *Advanced Functional Materials* **2011**, *21* (17), 3331-3336.
6. Do, K.; Saleem, Q.; Ravva, M. K.; Cruciani, F.; Kan, Z.; Wolf, J.; Hansen, M. R.; Beaujuge, P. M.; Brédas, J.-L., Impact of Fluorine Substituents on π -Conjugated Polymer Main-Chain Conformations, Packing, and Electronic Couplings. *Advanced Materials* **2016**, *28* (37), 8197-8205.
7. Graham, K. R.; Cabanetos, C.; Jahnke, J. P.; Idso, M. N.; El Labban, A.; Ngongang Ndjawa, G. O.; Heumueller, T.; Vandewal, K.; Salleo, A.; Chmelka, B. F.; Amassian, A.; Beaujuge, P. M.; McGehee, M. D., Importance of the Donor:Fullerene Intermolecular Arrangement for High-Efficiency Organic Photovoltaics. *Journal of the American Chemical Society* **2014**, *136* (27), 9608-9618.
8. Li, W.; Albrecht, S.; Yang, L.; Roland, S.; Tumbleston, J. R.; McAfee, T.; Yan, L.; Kelly, M. A.; Ade, H.; Neher, D.; You, W., Mobility-Controlled Performance of Thick Solar Cells Based on Fluorinated Copolymers. *Journal of the American Chemical Society* **2014**, *136* (44), 15566-15576.
9. Li, Z.; Jiang, K.; Yang, G.; Lai, J. Y. L.; Ma, T.; Zhao, J.; Ma, W.; Yan, H., Donor polymer design enables efficient non-fullerene organic solar cells. *Nature Communications* **2016**, *7* (1), 13094.
10. Li, Z.; Lin, H.; Jiang, K.; Carpenter, J.; Li, Y.; Liu, Y.; Hu, H.; Zhao, J.; Ma, W.; Ade, H.; Yan, H., Dramatic performance enhancement for large bandgap thick-film polymer solar cells introduced by a difluorinated donor unit. *Nano Energy* **2015**, *15*, 607-615.
11. Liu, Y.; Zhao, J.; Li, Z.; Mu, C.; Ma, W.; Hu, H.; Jiang, K.; Lin, H.; Ade, H.; Yan, H., Aggregation and morphology control enables multiple cases of high-efficiency polymer solar cells. *Nature Communications* **2014**, *5* (1), 5293.
12. Stuart, A. C.; Tumbleston, J. R.; Zhou, H.; Li, W.; Liu, S.; Ade, H.; You, W., Fluorine Substituents Reduce Charge Recombination and Drive Structure and Morphology Development in Polymer Solar Cells. *Journal of the American Chemical Society* **2013**, *135* (5), 1806-1815.
13. Yang, G.; Li, Z.; Jiang, K.; Zhang, J.; Chen, J.; Zhang, G.; Huang, F.; Ma, W.; Yan, H., Optimal extent of fluorination enabling strong temperature-dependent aggregation, favorable

- blend morphology and high-efficiency polymer solar cells. *Science China Chemistry* **2017**, *60* (4), 545-551.
14. Zhao, J.; Li, Y.; Yang, G.; Jiang, K.; Lin, H.; Ade, H.; Ma, W.; Yan, H., Efficient organic solar cells processed from hydrocarbon solvents. *Nature Energy* **2016**, *1* (2), 15027.
 15. Ashokan, A.; Wang, T.; Ravva, M. K.; Brédas, J.-L., Impact of solution temperature-dependent aggregation on the solid-state packing and electronic properties of polymers for organic photovoltaics. *Journal of Materials Chemistry C* **2018**, *6* (48), 13162-13170.
 16. Do, K.; Ravva, M. K.; Wang, T.; Brédas, J.-L., Computational Methodologies for Developing Structure–Morphology–Performance Relationships in Organic Solar Cells: A Protocol Review. *Chemistry of Materials* **2017**, *29* (1), 346-354.
 17. Plimpton, S., Fast Parallel Algorithms for Short-Range Molecular Dynamics. *Journal of Computational Physics* **1995**, *117* (1), 1-19.
 18. Cheung, D. L.; Troisi, A., Theoretical Study of the Organic Photovoltaic Electron Acceptor PCBM: Morphology, Electronic Structure, and Charge Localization. *The Journal of Physical Chemistry C* **2010**, *114* (48), 20479-20488.
 19. Dahlgren, M. K.; Schyman, P.; Tirado-Rives, J.; Jorgensen, W. L., Characterization of Biaryl Torsional Energetics and its Treatment in OPLS All-Atom Force Fields. *Journal of Chemical Information and Modeling* **2013**, *53* (5), 1191-1199.
 20. Jackson, N. E.; Kohlstedt, K. L.; Savoie, B. M.; Olvera de la Cruz, M.; Schatz, G. C.; Chen, L. X.; Ratner, M. A., Conformational Order in Aggregates of Conjugated Polymers. *Journal of the American Chemical Society* **2015**, *137* (19), 6254-6262.
 21. Jorgensen, W. L.; Maxwell, D. S.; Tirado-Rives, J., Development and Testing of the OPLS All-Atom Force Field on Conformational Energetics and Properties of Organic Liquids. *Journal of the American Chemical Society* **1996**, *118* (45), 11225-11236.
 22. Jorgensen, W. L.; Tirado-Rives, J., The OPLS [optimized potentials for liquid simulations] potential functions for proteins, energy minimizations for crystals of cyclic peptides and crambin. *Journal of the American Chemical Society* **1988**, *110* (6), 1657-1666.
 23. Wang, T.; Chen, X.-K.; Ashokan, A.; Zheng, Z.; Ravva, M. K.; Brédas, J.-L., Bulk Heterojunction Solar Cells: Impact of Minor Structural Modifications to the Polymer Backbone on the Polymer–Fullerene Mixing and Packing and on the Fullerene–Fullerene Connecting Network. *Advanced Functional Materials* **2018**, *28* (14), 1705868.
 24. Dupradeau, F.-Y.; Pigache, A.; Zaffran, T.; Savineau, C.; Lelong, R.; Grivel, N.; Lelong, D.; Rosanski, W.; Cieplak, P., The R.E.D. tools: advances in RESP and ESP charge derivation and force field library building. *Physical Chemistry Chemical Physics* **2010**, *12* (28), 7821-7839.
 25. Marcus, R. A., Electron transfer reactions in chemistry theory and experiment. *Journal of Electroanalytical Chemistry* **1997**, *438* (1), 251-259.
 26. Coropceanu, V.; Cornil, J.; da Silva Filho, D. A.; Olivier, Y.; Silbey, R.; Brédas, J.-L., Charge Transport in Organic Semiconductors. *Chemical Reviews* **2007**, *107* (4), 926-952.
 27. Frisch, M. J.; Trucks, G. W.; Schlegel, H. B.; Scuseria, G. E.; Robb, M. A.; Cheeseman, J. R.; Scalmani, G.; Barone, V.; Mennucci, B.; Petersson, G. A.; Nakatsuji, H.; Caricato, M.; Li, X.; Hratchian, H. P.; Izmaylov, A. F.; Bloino, J.; Zheng, G.; Sonnenberg, J. L.; Hada, M.; Ehara, M.; Toyota, K.; Fukuda, R.; Hasegawa, J.; Ishida, M.; Nakajima, T.; Honda, Y.; Kitao, O.; Nakai, H.; Vreven, T.; Montgomery Jr., J. A.; Peralta, J. E.; Ogliaro, F.; Bearpark, M. J.; Heyd, J.; Brothers, E. N.; Kudin, K. N.; Staroverov, V. N.; Kobayashi, R.; Normand, J.; Raghavachari, K.; Rendell, A. P.; Burant, J. C.; Iyengar, S. S.; Tomasi,

- J.; Cossi, M.; Rega, N.; Millam, N. J.; Klene, M.; Knox, J. E.; Cross, J. B.; Bakken, V.; Adamo, C.; Jaramillo, J.; Gomperts, R.; Stratmann, R. E.; Yazyev, O.; Austin, A. J.; Cammi, R.; Pomelli, C.; Ochterski, J. W.; Martin, R. L.; Morokuma, K.; Zakrzewski, V. G.; Voth, G. A.; Salvador, P.; Dannenberg, J. J.; Dapprich, S.; Daniels, A. D.; Farkas, Ö.; Foresman, J. B.; Ortiz, J. V.; Cioslowski, J.; Fox, D. J., Gaussian 09, Revision D. 01, Gaussian, Inc.: Wallingford, CT **2009**.
28. Boys, S. F.; Bernardi, F., The calculation of small molecular interactions by the differences of separate total energies. Some procedures with reduced errors. *Molecular Physics* **1970**, *19* (4), 553-566.
29. Hu, Z.; Haws, R. T.; Fei, Z.; Boufflet, P.; Heeney, M.; Rossky, P. J.; Vanden Bout, D. A., Impact of backbone fluorination on nanoscale morphology and excitonic coupling in polythiophenes. *Proceedings of the National Academy of Sciences* **2017**, *114* (20), 5113.
30. Nielsen, C. B.; White, A. J. P.; McCulloch, I., Effect of Fluorination of 2,1,3-Benzothiadiazole. *The Journal of Organic Chemistry* **2015**, *80* (10), 5045-5048.

CHAPTER-4

Bulk-heterojunction solar cells: Understanding the intermolecular packing and electronic properties in polymer-small-molecule acceptor blends

4.1. Introduction

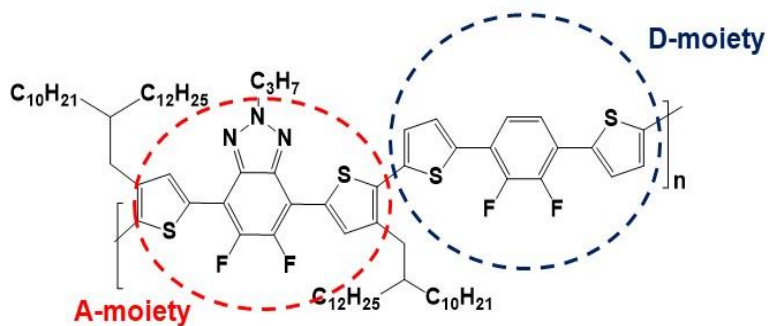
In single-junction organic solar cells (OSCs), there are two prominent compositions of the active-layer components – binary and ternary. While the former includes an electron donor and an electron acceptor, the latter contains one additional electron-donor or electron-acceptor component. Adding a suitable component to the binary blends is typically done to expand the absorption window vs. the solar spectrum,¹⁻⁵ and/or to improve charge-transport, and subsequently to lead to relatively higher device performance.⁶⁻⁹ As already demonstrated in multiple reports, the presence of a third component can also optimize the active-layer morphology in the form of increasing crystallinity and improving crystal orientation and domain sizes.¹⁰⁻¹³ Several investigations also show enhanced photo-stability and device storage lifetime for ternary blends as compared to binary ones.¹⁴⁻¹⁶

Experimental studies on the morphological properties of binary blends of polymer and fullerene derivatives have illustrated the presence of a three-phase structure in the active layer,¹⁷⁻²² that is, pure and intermixed phases of electron donors and electron acceptors coexisting in the active layer. The binary blends of polymer and non-fullerene small-molecule acceptors (SMAs) are also expected to follow the same structure. Increasing the number of components in the active layer to a ternary blend leads to significantly more complex descriptions and control of the active-layer

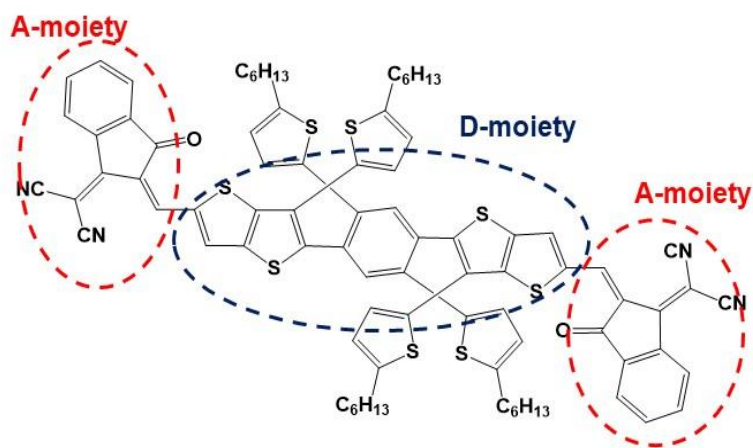
morphology. To boost the application of ternary blends in OSCs, it is important to determine the best approaches regarding morphology control while avoiding any negative impact on the variables that influence device performance.

Recently, Yan and co-workers developed a protocol for morphological control in ternary blends via minimizing the interfacial tensions among the three components.¹⁰ The ternary blend includes a polymer donor and two SMAs. The morphology control was enabled through multiple aspects. Firstly, a polymer showing a temperature-dependent aggregation (TDA) property in solution was selected as the donor component, which leads to small domains for the pure polymer phase.²³ The TDA property also allows the control of crystallization of these domains.²³⁻²⁷ Secondly, the selection of components was based on their surface tensions. The components with minimal difference in their surface tensions showed lesser interfacial tension and subsequently lesser phase-separation in the blends. Finally, reduced interfacial tension between SMAs leads to greater intermolecular intermixing. As a result, the ternary blend behaves essentially like a binary system with the polymer forming one component and the mixture of SMAs (working as an electronic alloy) forming another component. Notably, for the OSCs made of such ternary blends, the open-circuit voltage (V_{OC}) was found to follow a quasi-linear evolution *vs* the SMA composition. The fill factors for all ternary combinations of D-A1-A2 were found to be higher than those for the binary combinations of D-A1 or D-A2. Also, the introduction of the second SMA was shown to improve the crystallinity of the first SMA in the active layer. While this strategy was found to be effective for improving the efficiencies, an understanding of the molecular-scale origin of the linear evolution of V_{OC} and improvement in fill factor in the ternary blends remains to be developed. Here, we have combined atomistic molecular dynamics (MD) simulations and long-range

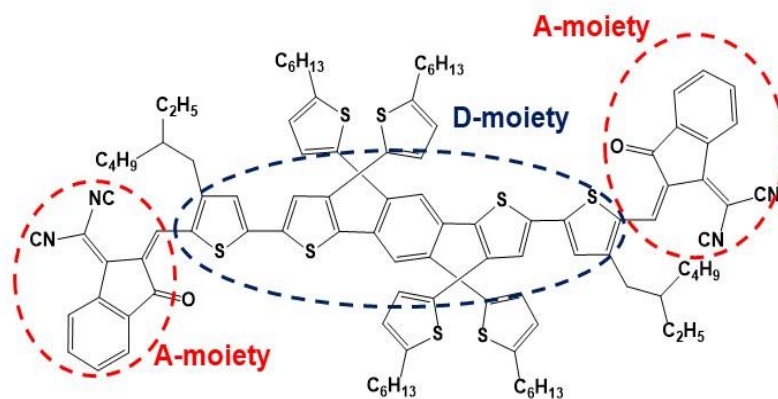
corrected density functional theory (DFT) calculations to investigate the intermolecular packing patterns and interactions as well as the related electronic properties (including electron-transfer rates among SMAs, interfacial charge-transfer states, and non-radiative recombination rates), in order to rationalize the morphological and electronic properties of these ternary blends. We have considered 4-(3-(2-decyltetradecyl)-5'-(2,3-difluoro-4-(5-methylthiophen-2-yl)phenyl)-[2,2'-bithiophen]-5-yl)-7-(4-(2-decyltetradecyl)-5-methylthiophen-2-yl)-5,6-difluoro-2-propyl-2H-benzo[d][1,2,3]triazole (PTFB-O) as the polymer donor and 3,9-bis(2-methylene-(3-(1,1-dicyanomethylene)-indanone))-5,5,11,11-tetrakis(5-hexylthienyl)-dithieno[2,3-d:2',3'-d']-s-indaceno[1,2-b:5,6-b']dithiophene (ITIC-Th) as well as 2,2'-((2Z,2'Z)-(((4,4,9,9-tetrakis(5-hexylthiophen-2-yl)-4,9-dihydro-s-indaceno[1,2-b:5,6-b']dithiophene-2,7-diyl)bis(4-octylthiophene-5,2-diyl))-bis(methanylylidene))bis(3-oxo-2,3-dihydro-1H-indene-2,1-diylidene))-dimalononitrile (IEIC-Th) as the SMAs, see **Figure 4.1**. Due to the limitations of all-atom MD simulations in terms of system sizes and time scales required for the investigation of ternary blends, we have divided the ternary combination into the three binary combinations, *i.e.*, PTFB-O:ITIC-Th, PTFB-O:IEIC-Th, and ITIC-Th:IEIC-Th. Here, as a first step into this general investigation, we have focused on distinguishing the intermolecular packing and electronic properties between the PTFB-O:ITIC-Th and PTFB-O:IEIC-Th binary blends.



PTFB-O



ITIC-Th



IEIC-Th

Figure 4.1. Chemical structures of PTFB-O, ITIC-Th, and IEIC-Th. The groups circled in red represents the electron-poor (A) moiety and those circled in blue represents the electron-rich (D) moiety.

4.2. Methodology

4.2.1 Molecular dynamics simulations

The MD simulations were performed with the LAMMPS package²⁸ and optimized potential for liquid simulations-all atom (OPLS-AA) force field.²⁹ To accurately model the intra- and intermolecular interactions, the OPLS-AA force-field was parameterized for atomic charges, bond lengths, bond angles, and dihedrals between different fragments. The parameterization of the force-field was performed based on the method described in Chapter 2 of this Thesis. Here, all the DFT calculations were performed at the ω B97XD/6-31G** level of theory with the Gaussian 09.D01 package.³⁰

The initial models were built by randomly placing the PTFB-O chains and ITIC-Th or IEIC-Th molecules in cubic cells at a low density of 0.02 g cm^{-3} . The donor:acceptor weight ratio was kept the same as the experimental value of 1:1.5. For the PTFB-O:ITIC-Th blend, the cell includes 30 PTFB-O chains and 405 ITIC-Th molecules (total of 131430 atoms), while for PTFB-O:IEIC-Th blend, the cell includes 30 PTFB-O chains and 341 IEIC-Th molecules (total of 139390 atoms). In each case, the PTFB-O chains consist of 10 repeat units.

The simulations were then carried out with the NPT (constant number of molecules, pressure and temperature) ensemble. For the summation of van der Waals interactions, a cut-off distance of 12 Å was applied. The particle-particle particle mesh (PPPM) solver³¹ was used for the long-range Coulomb interactions. Both the blends were initially kept at a high temperature of 500 K for 20 ns. We note that during the first 4 ns of simulations at 500 K, a small timestep of 0.1 fs was applied, which allows the system to slowly form the bulk. Then, a cooling process was performed by

running MD simulations for 500 ps for every 50 K from 500 K to 300 K. The Verlet integrator³² was applied with a timestep of 1.0 fs, and the Nose-Hover thermostat/barostat³³⁻³⁶ was employed for temperature/pressure control. To take account of the experimental annealing process, MD simulations were performed at 363 K for 50 ns followed by a cooling process to 300 K at the rate of 10 K ns⁻¹. Finally, MD simulations were performed at 300 K for 50 ns to allow the systems to equilibrate.

4.2.2 Density functional theory calculations

DFT calculations were performed at the ω B97XD/6-31G** level of theory to evaluate the interaction energies in pairs between PTFB-O and ITIC-Th [IEIC-Th] as well as in pairs of ITIC-Th [IEIC-Th] molecules. Here, the alkyl side chains of PTFB-O, ITIC-Th, and ITIC-Th were replaced with methyl groups; the PTFB-O chain was truncated to dimer with ITIC-Th or IEIC-Th close to the center of the dimer. To avoid the basis set superposition error (BSSE), the counterpoise-correction method proposed by Boys and Bernardi was applied.³⁷

The lowest singlet charge-transfer (¹CT₁) excited states were evaluated via TDDFT calculations at the ω B97XD/6-31G** level of theory. The range-separation parameter, ω , was optimized via a non-empirical tuning procedure³⁸ within the polarizable continuum model (PCM),³⁹ using a typical dielectric constant of $\epsilon = 3.5$.

Within the framework of semiclassical Marcus equation,⁴⁰ the electronic coupling (transfer integral) is a relevant parameter to estimate the extent of electronic interaction between states. Here, these transfer integrals were calculated using a fragment orbital approach.⁴¹ We have also

estimated the electron-transfer rates among SMAs using the semi-classical Marcus equation. The corresponding electronic couplings, reorganization energies, and energy differences between states were calculated at the PCM-tuned ω B97XD/6-31G** level of theory.

To determine the V_{OC} losses, we estimated the non-radiative recombination rates. In the case of a 1CT_1 energy larger than ~ 1 eV, the quantum component of the reorganization energy becomes important.⁴²⁻⁴⁴ Thus, the Marcus-Levich-Jortner model^{42, 45, 46} was used to examine these rates. Here as well, the calculations were performed at the PCM-tuned ω B97XD/6-31G** level of theory.

4.3. Results and Discussion

4.3.1 Intermolecular packing and interactions

It has been reported experimentally that the active layers composed of binary combinations of PTFB-O:ITIC-Th or PTFB-O:IEIC-Th and ternary combination of PTFB-O:ITIC-Th:IEIC-Th exhibit similar, homogenous bulk morphologies.¹⁰ To gain an understanding of this morphological similarity, we have investigated the intermolecular packing patterns and interactions in two binary blends of PTFB-O:ITIC-Th and PTFB-O:IEIC-Th.

Figure 4.2 shows the radial distribution functions (RDFs), $g(r)$, between the PTFB-O backbones and the SMAs in the PTFB-O:ITIC-Th and PTFB-O:IEIC-Th blends. We recall that a higher $g(r)$ peak corresponds to a larger packing density in the blends, with the first peak around ~ 5 Å indicating the nearest-neighbor PTFB-O/SMA packing. The very similar $g(r)$ peaks at this distance suggest similar PTFB-O/SMA packing densities and intermolecular interactions in the two blends.

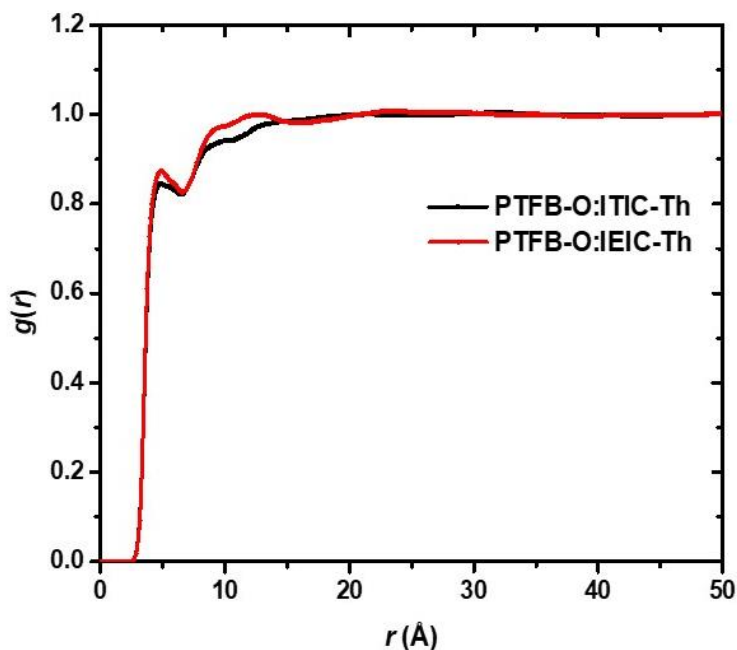


Figure 4.2. Radial distribution functions between PTFB-O backbones and SMAs in the PTFB-O:ITIC-Th and PTFB-O:IEIC-Th blends.

To further confirm this point, we have extracted all the PTFB-O:ITIC-Th, PTFB-O:IEIC-Th pairs and the ITIC-Th:ITIC-Th, IEIC-Th:IEIC-Th dimers from the MD-simulated PTFB-O:ITIC-Th and PTFB-O:IEIC-Th blends. Here, a “pair” corresponds to one PTFB-O chain interacting with a SMA within a distance of ~ 5 Å of each other, and a “dimer” corresponds to the case of two interacting SMAs. We note that, to save computational time for the quantum-chemical calculations, the long PTFB-O chain with 10 repeat units are truncated to 2 repeat units. Calculations at the (counterpoise-corrected) ω B97XD/6-31G** level indicate that the intermolecular interaction energies in PTFB-O:ITIC-Th pairs are similar to those in PTFB-O:IEIC-Th pairs (see **Table 4.1**). The same holds true between ITIC-Th:ITIC-Th and IEIC-Th:IEIC-Th dimers. These findings support the RDF results and point to an identical degree of polymer-SMA mixing in both blends.

Table 4.1. Average interaction energies (and their standard deviations) among PTFB-O, ITIC-Th, and IEIC-Th pairs and dimers. A negative value indicates an attractive interaction.

	Average interaction energies (kcal mol ⁻¹)
PTFB-O:ITIC-Th	-18.1 ± 8.4
PTFB-O:IEIC-Th	-17.9 ± 8.2
ITIC-Th:ITIC-Th	-16.4 ± 8.8
IEIC-Th:IEIC-Th	-17.3 ± 9.3

4.3.2 Intermolecular packing patterns

Here, we assess the intermolecular packing patterns in the PTFB-O:ITIC-Th and PTFB-O:IEIC-Th blends, that is, the way the electron-rich ("donor", **D**) moieties or electron-poor ("acceptor", **A**) moieties preferentially pack on top of one another. The **D** and **A** moieties of PTFB-O, ITIC-Th, and IEIC-Th are illustrated in **Figure 4.1**.

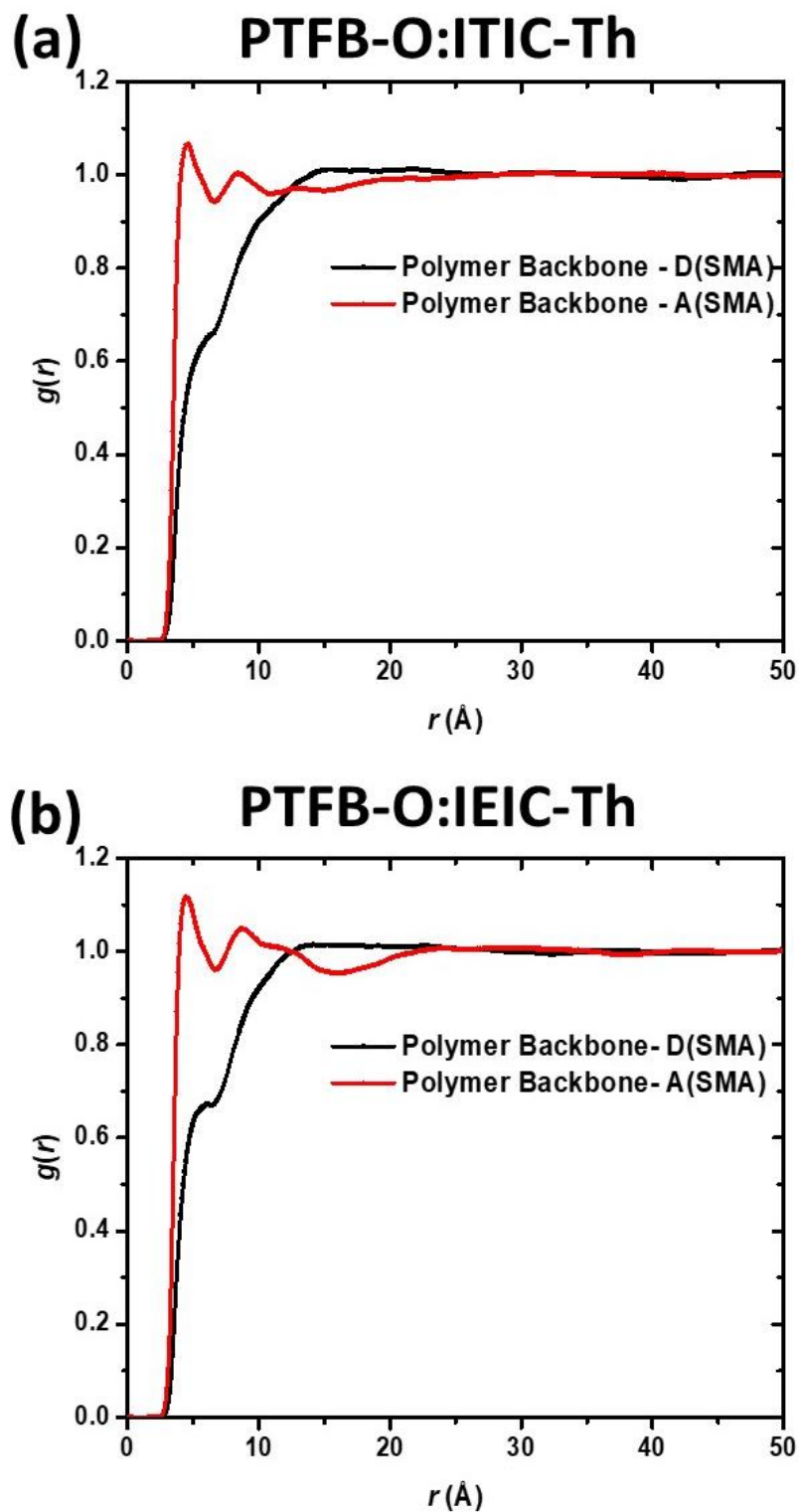


Figure 4.3. RDFs for: (a) interaction between the PTFB-O polymer backbone and the **D** moiety or **A** moiety of ITIC-Th acceptors, (b) interaction between the PTFB-O polymer backbone and the **D** moiety or **A** moiety of IEIC-Th acceptors.

We first examined the RDFs between the PTFB-O backbones and the **D/A** moieties of SMAs. **Figure 4.3** shows that around ~ 5 Å there exist gentle shoulders and sharp peaks for the RDFs between the PTFB-O backbones and the SMA **D** and **A** moieties, respectively. This indicates that the PTFB-O/SMA-**A** packing is the dominant packing pattern in both PTFB-O:ITIC-Th and PTFB-O:IEIC-Th blends; this can be attributed to the presence of the bulky hexylthiophene side chains on the SMA **D** moieties, which hinder close contacts with the PTFB-O backbones.

We further analyzed the RDFs between the **D** and **A** moieties of PTFB-O and the **A** moieties of the SMA molecules (see **Figure 4.4**). Interestingly, in both blends, the first $g(r)$ peaks that represent the PTFB-O-**A**/SMA-**A** packing density are markedly higher than those that represent the PTFB-O-**D**/SMA-**A** packing density. This suggests that the PTFB-O:ITIC-Th and PTFB-O:IEIC-Th blends have similar intermolecular donor/acceptor packing patterns: PTFB-O-**A**/SMA-**A** > PTFB-O-**D**/SMA-**A**. To quantify this observation, we explored the proportions of PTFB-O-**A**/SMA-**A** and PTFB-O-**D**/SMA-**A** pairs in both blends; the results show that $\sim 69\%$ of the packing in the PTFB-O:ITIC-Th blend and $\sim 70.5\%$ of the packing in the PTFB-O:IEIC-Th blend take place through PTFB-O-**A**/SMA-**A** packing patterns, in agreement with the RDF findings. Here as well, the average interaction energies were calculated for the PTFB-O-**A**/SMA-**A** and PTFB-O-**D**/SMA-**A** pairs extracted from the MD-simulated PTFB-O:ITIC-Th and PTFB-O:IEIC-Th blends. As expected, from the above discussion the interaction energies for the PTFB-O-**A**/SMA-**A** are larger than those for the PTFB-O-**D**/SMA-**A** pairs, see **Table 4.2**. The similarity in the PTFB-O/SMA packing density and pattern in the two binary blends can thus be anticipated to result in similar, well-mixed bulk morphologies in blends of PTFB-O:ITIC-Th and PTFB-O:IEIC-Th binary combinations and PTFB-O:ITIC-Th:IEIC-Th ternary combination.

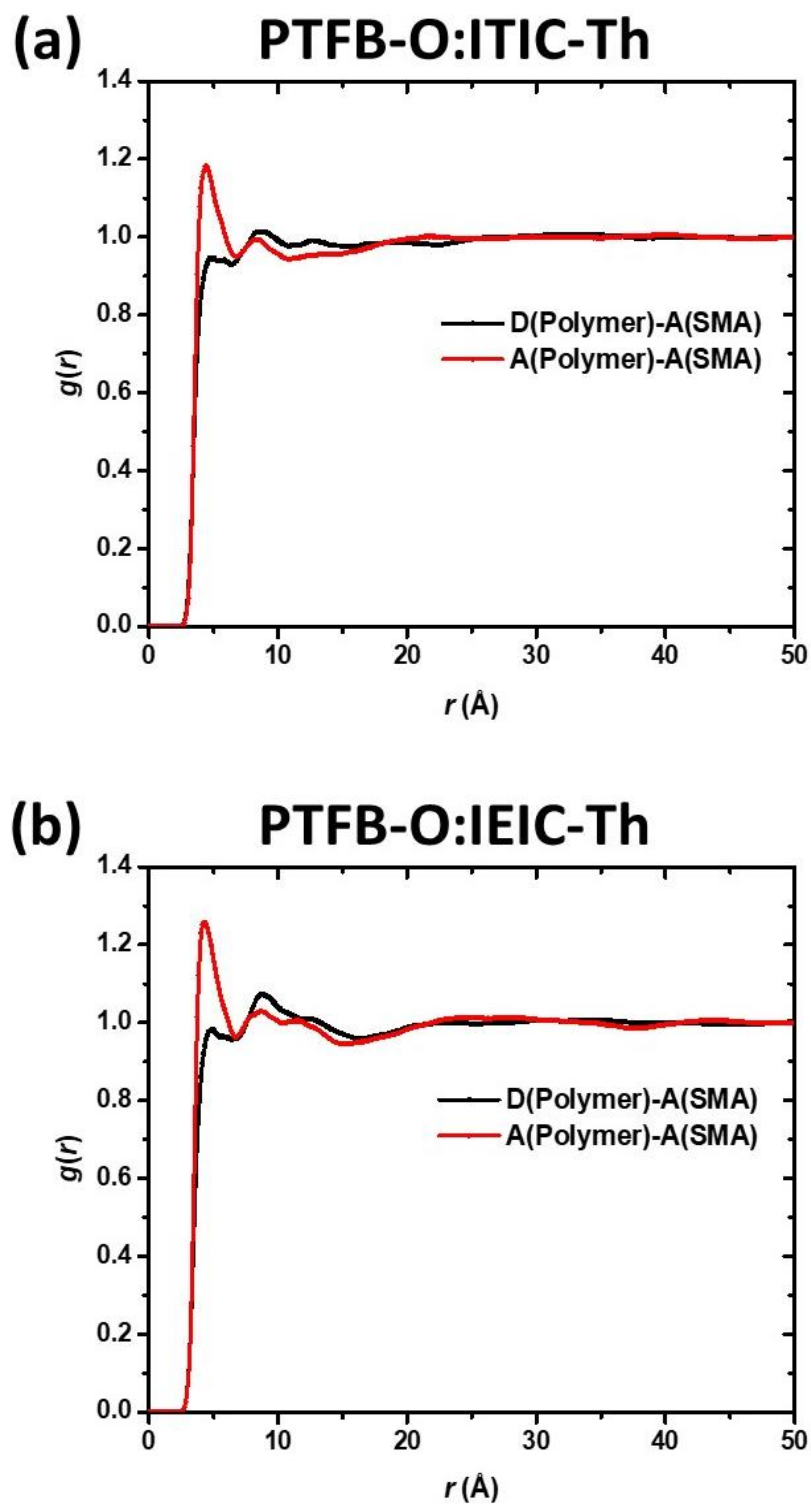


Figure 4.4. RDFs for: (a) interactions between the **D** moiety or **A** moiety of PTFB-O polymer and the **A** moiety of ITIC-Th acceptor, (b) interactions between **D** moiety or **A** moiety of PTFB-O polymer and the **A** moiety of IEIC-Th acceptor.

Table 4.2. Average interaction energies (and their standard deviations) for PTFB-O-**A**/SMA-**A** and PTFB-O-**D**/SMA-**A** pairs extracted from the MD-simulated PTFB-O:ITIC-Th and PTFB-O:IEIC-Th blends.

	Average interaction energies (kcal mol ⁻¹)	
	PTFB-O- A /SMA- A	PTFB-O- D /SMA- A
PTFB-O:ITIC-Th blend	-17.8 ± 7.9	-16.1 ± 8.2
PTFB-O:IEIC-Th blend	-18.6 ± 8.0	-14.4 ± 6.9

To this end, we examined the SMA/SMA packing patterns in both blends. The partial RDFs for the SMA-**D**/SMA-**D**, SMA-**D**/SMA-**A**, and SMA-**A**/SMA-**A** interactions point to very closely related packing patterns in both blends, with interactions decreasing in the order: SMA-**A**/SMA-**A** > SMA-**D**/SMA-**A** > SMA-**D**/SMA-**D**, see **Figure 4.5**. Again, we note that the more the **D** moieties are involved, the lesser the packing density, which can be attributed to the steric hindrance of the bulky hexylthiophene side chains attached on the **D** moieties of the ITIC-Th and IEIC-Th molecules.

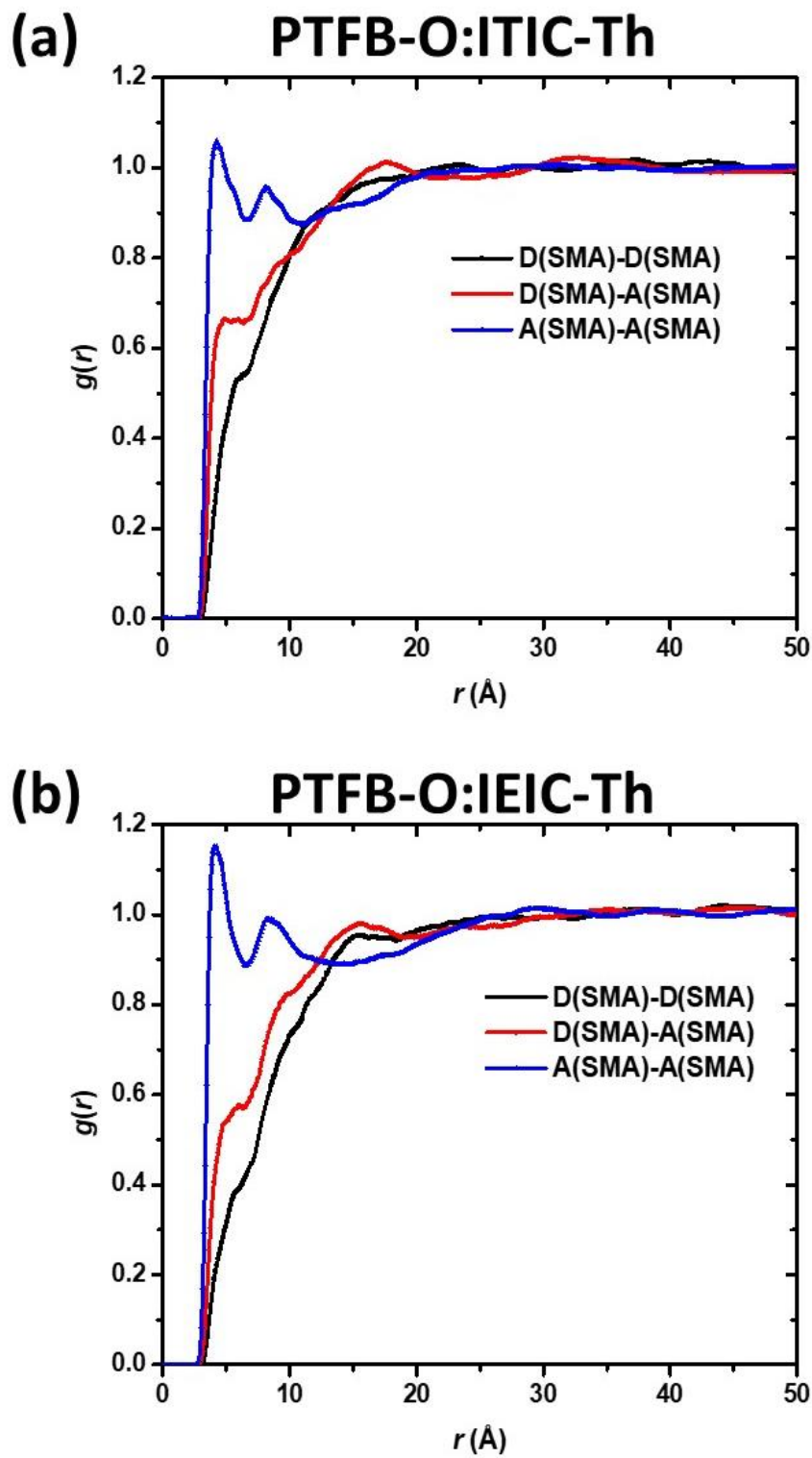


Figure 4.5. RDFs for the SMA-D/SMA-D, SMA-D/SMA-A, and SMA-A/SMA-A interactions in (a) PTFB-O:ITIC-Th and (b) PTFB-O:IEIC-Th.

4.3.3 Intermolecular electron-transfer rates among adjacent SMAs

We now turn to a discussion of the electron-transport processes in the PTFB-O:ITIC-Th and PTFB-O:IEIC-Th blends by evaluating the electron-transfer rates among SMA/SMA dimers via the semi-classical Marcus equation. Here, we evaluate the electronic couplings between the lowest unoccupied molecular orbitals (LUMOs) relevant for the electron-transport processes. **Table 4.3** collects the average LUMO-LUMO (V_{L-L}) couplings (and their standard deviations). As the calculation of electron-transfer rates considers the squares of the electron couplings, we note that the signs of the relevant transfer integrals have not been tracked. **Table 4.3** shows that the ITIC-Th/ITIC-Th dimers exhibit somewhat stronger electronic couplings as compared to the IEIC-Th/IEIC-Th dimers. To further confirm this, **Figure 4.6** provides a distribution of the electronic couplings for all the ITIC-Th/ITIC-Th (IEIC-Th/IEIC-Th) dimers extracted from the MD-simulated PTFB-O:ITIC-Th (PTFB-O:IEIC-Th) blend. At lower coupling values below ~ 20 meV, the IEIC-Th/IEIC-Th dimers present a higher distribution than the ITIC-Th/ITIC-Th dimers, a trend that reverses at higher coupling values.

Table 4.3. Average electronic couplings (V_{L-L}) and the standard deviations between the LUMOs of SMA/SMA dimers extracted from the MD-simulated PTFB-O:ITIC-Th and PTFB-O:IEIC-Th blends.

SMA/SMA dimers	V_{L-L} (meV)
ITIC-Th/ITIC-Th	17.6 ± 18.2
IEIC-Th/IEIC-Th	13.9 ± 15.6

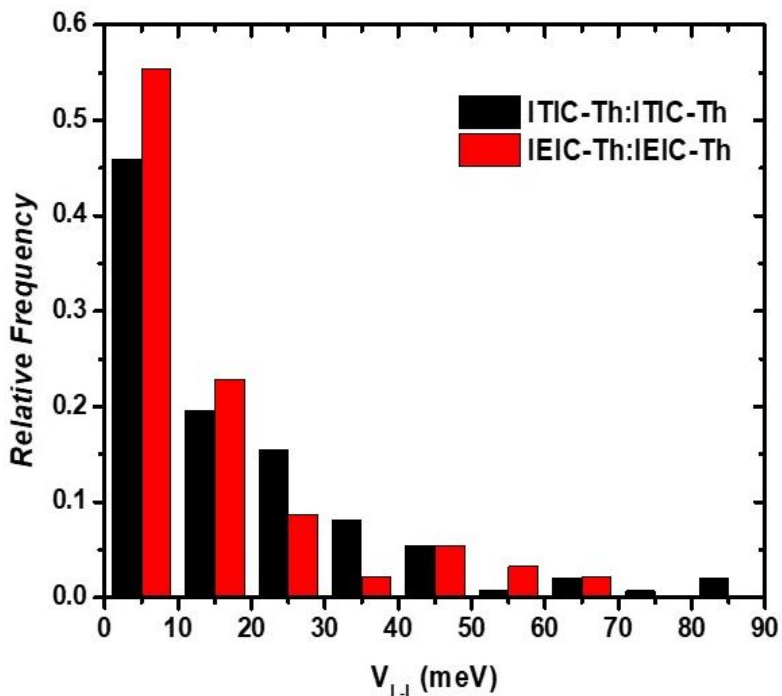


Figure 4.6. Distributions for the electronic couplings between the LUMOs of SMAs all the SMA/SMA dimers extracted from the MD-simulated PTFB-O:ITIC-Th and PTFB-O:IEIC-Th blends.

We also evaluated another important transport parameter i.e., reorganization energy (λ). The intramolecular reorganization energies were found to be slightly very higher for ITIC-Th (~175 meV) than IEIC-Th (~169 meV). By fitting the electronic couplings, reorganization energies, and the energy differences (between the initial and final states) into the semi-classical Marcus equation, **Table 4.4** collects the proportions of SMA/SMA dimers at different orders of magnitude of electron-transfer rates for both blends.

Table 4.4. Proportions of SMA/SMA dimers corresponding to different orders of magnitude in electron-transfer rates and experimentally measured electron mobilities for the blends of PTFB-O:ITIC-Th and PTFB-O:IEIC-Th.

Electron-transfer rates (s^{-1})	PTFB-O:ITIC-Th	PTFB-O:IEIC-Th
$>10^{12}$	45.3%	38.0%
$>10^{11}$	76.3%	66.3%
$>10^{10}$	90.5%	83.6%
$>10^9$	97.2%	94.5%
$<10^9$	2.7%	5.4%
Experimentally measured electron mobility ($cm^2 V^{-1} s^{-1}$)	4.6×10^{-5}	2.6×10^{-5}

Interestingly, all the higher levels of electron-transfer rates (*i.e.*, $>10^{12} s^{-1}$, $>10^{11} s^{-1}$, $>10^{10} s^{-1}$, $>10^9 s^{-1}$) correspond to a higher proportion of ITIC-Th/ITIC-Th dimers in PTFB-O:ITIC-Th blend, as compared to that of IEIC-Th/IEIC-Th dimers in PTFB-O:IEIC-Th blend. These trends contribute to rationalize the slightly higher mobility and J_{sc} for the PTFB-O:ITIC-Th blend.

4.3.4. Interfacial charge-transfer states and non-radiative recombination rates

Finally, we examined the interfacial charge-transfer (CT) states and non-radiative recombination rates for the two blends. We extracted approximately ~600 PTFB-O/SMA pairs from three snapshots of the MD-simulated PTFB-O:ITIC-Th or PTFB-O:IEIC-Th blends. **Figure 4.7** displays the energetic distribution of the CT states (via fitting to a Gaussian function) for both blends.

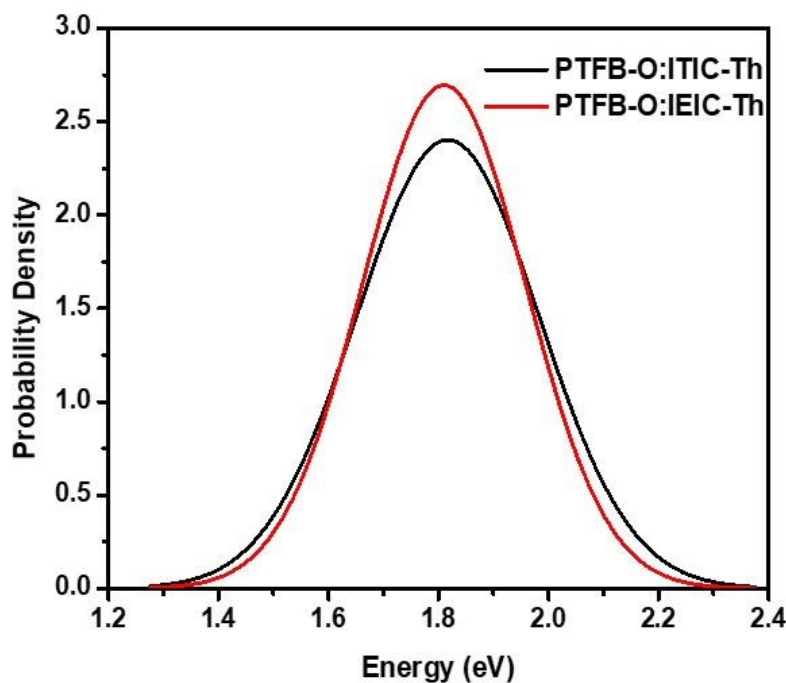


Figure 4.7. Energetic distribution of the CT states in MD-simulated blends of PTFB-O:ITIC-Th and PTFB-O:IEIC-Th.

The average CT-state energies of (E_{CT}^a) are very close (*i.e.*, 1.817 eV for PTFB-O:ITIC-Th and 1.810 eV for PTFB-O:IEIC-Th). However, a notable difference is found for their standard deviations, which relate to the total disorder, *i.e.*, ~ 166 meV for PTFB-O:ITIC-Th and ~ 148 meV for PTFB-O:IEIC-Th. There thus occurs a larger energetic disorder in the former case.

We recall that the total energetic disorder of the CT states arises from two contributions – static and dynamic. While the former is linked to variations in positions and geometries of donor and acceptor molecules in blends, which lead to a *time-independent* variance in CT-state energies, the latter occurs due to electron-vibration interactions and results in a *time-dependent* variance in CT-state energies (the standard deviations corresponding to total, dynamic, and static disorders are denoted by σ_T , σ_D , and σ_S , respectively). When the static and dynamic components follow

Gaussian distributions, the total variances of the CT-state energies can be expressed as: $\sigma_T^2 = \sigma_D^2 + \sigma_S^2$.⁴⁷⁻⁴⁹ We obtain the dynamic disorder by considering the PTFB-O/SMA pairs generated from trajectories of MD simulations as a function of time; the coordinates of 200 configurations of each of 5 randomly selected PTFB-O/SMA pairs are extracted from the trajectories of the MD-simulated blends. We then evaluate σ_D for all selected pairs and average them. The static component is then simply calculated via $\sigma_S = \sqrt{\sigma_T^2 - \sigma_D^2}$.⁴⁹ **Table 4.5** summarizes the total, dynamic, and static contributions to the energetic disorders in both blends. Interestingly, the extent of dynamic disorder is similar in both blends. Consequently, static disorder contributes to the difference in the total disorder between the two blends.

Table 4.5. Standard deviations of the energetic distributions of the CT states, corresponding to total, dynamic, and static disorders for the PTFB-O:ITIC-Th and PTFB-O:IEIC-Th blends.

	σ_T (meV)	σ_D (meV)	σ_S (meV)
PTFB-O:ITIC-Th blend	166	116	118
PTFB-O:IEIC-Th blend	148	116	91

Since an exact partition of the reorganization energy into classical (λ_c) and quantum components (λ_{qm}) is not known (where $\lambda = \lambda_c + \lambda_{qm}$; λ is the total reorganization energy), **Figure 4.8** presents the non-radiative recombination rates, k_{nr} , as a function of the value chosen for the quantum component of the reorganization energy. We note that the estimation here is based on the Marcus-Levich-Jortner model that includes the quantum effects.^{45, 50}

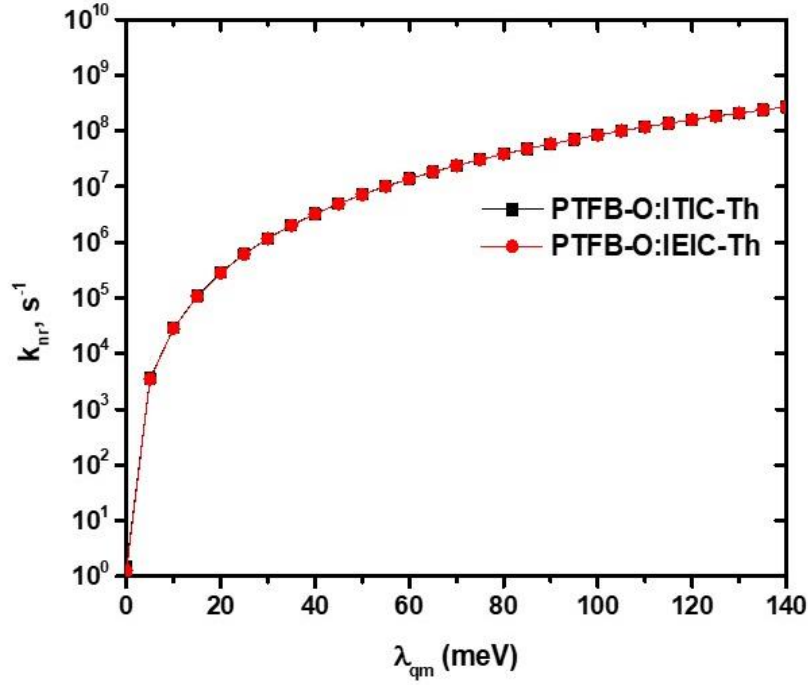


Figure 4.8. Non-radiative recombination rates as a function of the quantum component of reorganization energy.

It is seen that the evolution of the k_{nr} values of both blends overlap as a function of λ_{qm} , which implies that the voltage losses from the non-radiative recombination processes should be nearly identical in both cases. Therefore, the differences in the experimental V_{oc} values between the two blends (PTFB-O:ITIC and PTFB-O:IEIC-Th) arise from the different distributions of the CT-state energies. Here, with the average CT-state energies being similar for both blends, the blend with lower disorder is predicted to have a higher V_{oc} .

To further clarify this point, we estimate the effective CT-state energy, E_{CT}^e , on the basis of the calculated E_{CT}^a and σ_T values. We employ the relation of $E_{CT}^e = E_{CT}^a - \frac{\sigma_T^2}{2k_B T}$, where k_B is Boltzmann constant and T is the temperature (see **Table 4.6**).^{51, 52} The effective CT-state energies are found

to be 1.26 eV and 1.37 eV for the PTFB-O:ITIC-Th and PTFB-O:IEIC-Th blends, respectively. The 0.1 eV higher V_{OC} in the PTFB-O:IEIC-Th is consistent with the higher E_{CT}^e value, which is induced by the lower interfacial disorder.

Table 4.6. Average CT-state energy (E_{CT}^a); standard deviation (σ_T); V_{OC} loss due to interfacial disorder ($\frac{\sigma_T^2}{2k_B T}$); effective CT-state energy (E_{CT}^e) evaluated using $E_{CT}^e = E_{CT}^a - \frac{\sigma_T^2}{2k_B T}$,⁵¹ and experimentally measured V_{OC} ,¹⁰ for the cases of PTFB-O:ITIC-Th and PTFB-O:IEIC-Th.

Blends	E_{CT}^a (eV)	σ_T (eV)	$\frac{\sigma_T^2}{2k_B T}$ (eV)	E_{CT}^e (eV)	Exp. V_{OC} (V)
PTFB-O:ITIC-Th	1.817	0.166	0.551	1.266	0.92
PTFB-O:IEIC-Th	1.810	0.148	0.438	1.372	1.02

4.4. Conclusions

We have used a combination of MD simulations and long-range corrected DFT calculations to examine the intermolecular packing and electronic properties in the binary blends of PTFB-O:ITIC-Th and PTFB-O:IEIC-Th. Our main results can be summarized as follows:

- (i) The intermolecular donor/acceptor packing density is found to be very much the same in both blends, which is induced by the similar nature of the intermolecular interactions.
- (ii) The intermolecular packing patterns between PTFB-O and the SMAs are nearly identical in the two blends and mainly proceed through their A moieties; the same pattern is also found for the SMA/SMA packing. The similar intermolecular packing density and pattern point to the homogeneously well-mixed nature of the two binary blends. This is consistent with the linear

dependence of the V_{oc} values as a function of the concentration in one of the SMAs in the PTFB-O:ITIC-Th:IEIC-Th ternary blend.

(iii) The higher electronic couplings between neighboring ITIC-Th molecules in the PTFB-O:ITIC-Th blend leads to higher intermolecular electron-transfer rates, which accounts for the higher electron mobility and J_{sc} values in PTFB-O:ITIC-Th OSC.

(iv) While the average CT-state energies of both blends are similar, the different standard deviations corresponding to total energetic disorder mainly comes from the effect of static disorder.

(v) Similar non-radiative recombination rates point to similar non-radiative voltage losses in both blends. The difference in experimental V_{oc} values is expected to arise from different distributions of CT-state energies. With the average CT-state energy being the same, the PTFB-O:IEIC-Th blend that possesses a lower static energetic disorder has a higher V_{oc} .

4.5. References

1. Yang, Y.; Chen, W.; Dou, L.; Chang, W.-H.; Duan, H.-S.; Bob, B.; Li, G.; Yang, Y., High-performance multiple-donor bulk heterojunction solar cells. *Nature Photonics* **2015**, *9*, 190.
2. Xu, H.; Ohkita, H.; Tamai, Y.; Benten, H.; Ito, S., Interface Engineering for Ternary Blend Polymer Solar Cells with a Heterostructured Near-IR Dye. *Advanced Materials* **2015**, *27* (39), 5868-5874.
3. Huang, J.-S.; Goh, T.; Li, X.; Sfeir, M. Y.; Bielinski, E. A.; Tomasulo, S.; Lee, M. L.; Hazari, N.; Taylor, A. D., Polymer bulk heterojunction solar cells employing Förster resonance energy transfer. *Nature Photonics* **2013**, *7*, 479.
4. Khlyabich, P. P.; Burkhart, B.; Thompson, B. C., Compositional Dependence of the Open-Circuit Voltage in Ternary Blend Bulk Heterojunction Solar Cells Based on Two Donor Polymers. *Journal of the American Chemical Society* **2012**, *134* (22), 9074-9077.
5. Lu, L.; Xu, T.; Chen, W.; Landry, E. S.; Yu, L., Ternary blend polymer solar cells with enhanced power conversion efficiency. *Nature Photonics* **2014**, *8*, 716.
6. Khlyabich, P. P.; Burkhart, B.; Thompson, B. C., Efficient Ternary Blend Bulk Heterojunction Solar Cells with Tunable Open-Circuit Voltage. *Journal of the American Chemical Society* **2011**, *133* (37), 14534-14537.
7. Ameri, T.; Khoram, P.; Min, J.; Brabec, C. J., Organic Ternary Solar Cells: A Review. *Advanced Materials* **2013**, *25* (31), 4245-4266.
8. Felekidis, N.; Wang, E.; Kemerink, M., Open circuit voltage and efficiency in ternary organic photovoltaic blends. *Energy & Environmental Science* **2016**, *9* (1), 257-266.
9. Cheng, P.; Zhang, M.; Lau, T.-K.; Wu, Y.; Jia, B.; Wang, J.; Yan, C.; Qin, M.; Lu, X.; Zhan, X., Realizing Small Energy Loss of 0.55 eV, High Open-Circuit Voltage >1 V and High Efficiency >10% in Fullerene-Free Polymer Solar Cells via Energy Driver. *Advanced Materials* **2017**, *29* (11), 1605216.
10. Jiang, K.; Zhang, G.; Yang, G.; Zhang, J.; Li, Z.; Ma, T.; Hu, H.; Ma, W.; Ade, H.; Yan, H., Multiple Cases of Efficient Nonfullerene Ternary Organic Solar Cells Enabled by an Effective Morphology Control Method. *Advanced Energy Materials* **2018**, *8* (9), 1701370.
11. Li, H.; Lu, K.; Wei, Z., Polymer/Small Molecule/Fullerene Based Ternary Solar Cells. *Advanced Energy Materials* **2017**, *7* (17), 1602540.
12. Zhang, Y.; Deng, D.; Lu, K.; Zhang, J.; Xia, B.; Zhao, Y.; Fang, J.; Wei, Z., Synergistic Effect of Polymer and Small Molecules for High-Performance Ternary Organic Solar Cells. *Advanced Materials* **2015**, *27* (6), 1071-1076.
13. Nian, L.; Kan, Y.; Wang, H.; Gao, K.; Xu, B.; Rong, Q.; Wang, R.; Wang, J.; Liu, F.; Chen, J.; Zhou, G.; Russell, T. P.; Jen, A. K. Y., Ternary non-fullerene polymer solar cells with 13.51% efficiency and a record-high fill factor of 78.13%. *Energy & Environmental Science* **2018**, *11* (12), 3392-3399.
14. Cheng, P.; Yan, C.; Wu, Y.; Wang, J.; Qin, M.; An, Q.; Cao, J.; Huo, L.; Zhang, F.; Ding, L.; Sun, Y.; Ma, W.; Zhan, X., Alloy Acceptor: Superior Alternative to PCBM toward Efficient and Stable Organic Solar Cells. *Advanced Materials* **2016**, *28* (36), 8021-8028.
15. Cheng, P.; Yan, C.; Lau, T.-K.; Mai, J.; Lu, X.; Zhan, X., Molecular Lock: A Versatile Key to Enhance Efficiency and Stability of Organic Solar Cells. *Advanced Materials* **2016**, *28* (28), 5822-5829.

16. Baran, D.; Ashraf, R. S.; Hanifi, D. A.; Abdelsamie, M.; Gasparini, N.; Röhr, J. A.; Holliday, S.; Wadsworth, A.; Lockett, S.; Neophytou, M.; Emmott, C. J. M.; Nelson, J.; Brabec, C. J.; Amassian, A.; Salleo, A.; Kirchartz, T.; Durrant, J. R.; McCulloch, I., Reducing the efficiency–stability–cost gap of organic photovoltaics with highly efficient and stable small molecule acceptor ternary solar cells. *Nature Materials* **2016**, *16*, 363.
17. Hoppe, H.; Sariciftci, N. S., Morphology of polymer/fullerene bulk heterojunction solar cells. *Journal of Materials Chemistry* **2006**, *16* (1), 45-61.
18. Yang, X.; Loos, J., Toward High-Performance Polymer Solar Cells: The Importance of Morphology Control. *Macromolecules* **2007**, *40* (5), 1353-1362.
19. Liu, F.; Gu, Y.; Jung, J. W.; Jo, W. H.; Russell, T. P., On the morphology of polymer-based photovoltaics. *Journal of Polymer Science Part B: Polymer Physics* **2012**, *50* (15), 1018-1044.
20. Collins, B. A.; Tumbleston, J. R.; Ade, H., Miscibility, Crystallinity, and Phase Development in P3HT/PCBM Solar Cells: Toward an Enlightened Understanding of Device Morphology and Stability. *The Journal of Physical Chemistry Letters* **2011**, *2* (24), 3135-3145.
21. Burke, T. M.; McGehee, M. D., How High Local Charge Carrier Mobility and an Energy Cascade in a Three-Phase Bulk Heterojunction Enable >90% Quantum Efficiency. *Advanced Materials* **2014**, *26* (12), 1923-1928.
22. Sweetnam, S.; Graham, K. R.; Ngongang Ndjawa, G. O.; Heumüller, T.; Bartelt, J. A.; Burke, T. M.; Li, W.; You, W.; Amassian, A.; McGehee, M. D., Characterization of the Polymer Energy Landscape in Polymer:Fullerene Bulk Heterojunctions with Pure and Mixed Phases. *Journal of the American Chemical Society* **2014**, *136* (40), 14078-14088.
23. Li, Z.; Jiang, K.; Yang, G.; Lai, J. Y. L.; Ma, T.; Zhao, J.; Ma, W.; Yan, H., Donor polymer design enables efficient non-fullerene organic solar cells. *Nature Communications* **2016**, *7* (1), 13094.
24. Ashokan, A.; Wang, T.; Ravva, M. K.; Brédas, J.-L., Impact of solution temperature-dependent aggregation on the solid-state packing and electronic properties of polymers for organic photovoltaics. *Journal of Materials Chemistry C* **2018**, *6* (48), 13162-13170.
25. Yang, G.; Li, Z.; Jiang, K.; Zhang, J.; Chen, J.; Zhang, G.; Huang, F.; Ma, W.; Yan, H., Optimal extent of fluorination enabling strong temperature-dependent aggregation, favorable blend morphology and high-efficiency polymer solar cells. *Science China Chemistry* **2017**, *60* (4), 545-551.
26. Li, Z.; Lin, H.; Jiang, K.; Carpenter, J.; Li, Y.; Liu, Y.; Hu, H.; Zhao, J.; Ma, W.; Ade, H.; Yan, H., Dramatic performance enhancement for large bandgap thick-film polymer solar cells introduced by a difluorinated donor unit. *Nano Energy* **2015**, *15*, 607-615.
27. Liu, Y.; Zhao, J.; Li, Z.; Mu, C.; Ma, W.; Hu, H.; Jiang, K.; Lin, H.; Ade, H.; Yan, H., Aggregation and morphology control enables multiple cases of high-efficiency polymer solar cells. *Nature Communications* **2014**, *5* (1), 5293.
28. Plimpton, S., Fast Parallel Algorithms for Short-Range Molecular Dynamics. *Journal of Computational Physics* **1995**, *117* (1), 1-19.
29. Jorgensen, W. L.; Maxwell, D. S.; Tirado-Rives, J., Development and Testing of the OPLS All-Atom Force Field on Conformational Energetics and Properties of Organic Liquids. *Journal of the American Chemical Society* **1996**, *118* (45), 11225-11236.

30. Frisch, M. J.; Trucks, G. W.; Schlegel, H. B.; Scuseria, G. E.; Robb, M. A.; Cheeseman, J. R.; Scalmani, G.; Barone, V.; Mennucci, B.; Petersson, G. A.; Nakatsuji, H.; Caricato, M.; Li, X.; Hratchian, H. P.; Izmaylov, A. F.; Bloino, J.; Zheng, G.; Sonnenberg, J. L.; Hada, M.; Ehara, M.; Toyota, K.; Fukuda, R.; Hasegawa, J.; Ishida, M.; Nakajima, T.; Honda, Y.; Kitao, O.; Nakai, H.; Vreven, T.; Montgomery Jr., J. A.; Peralta, J. E.; Ogliaro, F.; Bearpark, M. J.; Heyd, J.; Brothers, E. N.; Kudin, K. N.; Staroverov, V. N.; Kobayashi, R.; Normand, J.; Raghavachari, K.; Rendell, A. P.; Burant, J. C.; Iyengar, S. S.; Tomasi, J.; Cossi, M.; Rega, N.; Millam, N. J.; Klene, M.; Knox, J. E.; Cross, J. B.; Bakken, V.; Adamo, C.; Jaramillo, J.; Gomperts, R.; Stratmann, R. E.; Yazyev, O.; Austin, A. J.; Cammi, R.; Pomelli, C.; Ochterski, J. W.; Martin, R. L.; Morokuma, K.; Zakrzewski, V. G.; Voth, G. A.; Salvador, P.; Dannenberg, J. J.; Dapprich, S.; Daniels, A. D.; Farkas, Ö.; Foresman, J. B.; Ortiz, J. V.; Cioslowski, J.; Fox, D. J., Gaussian 09, Revision D. 01, Gaussian. *Inc.: Wallingford, CT* **2009**.
31. Hockney, R. W.; Eastwood, J. W., *Computer simulation using particles*. Taylor & Francis, Inc.: 1988; p 564.
32. Verlet, L., Computer "Experiments" on Classical Fluids. I. Thermodynamical Properties of Lennard-Jones Molecules. *Physical Review* **1967**, *159* (1), 98-103.
33. Nosé, S., A molecular dynamics method for simulations in the canonical ensemble. *Molecular Physics* **1984**, *52* (2), 255-268.
34. Nosé, S., A unified formulation of the constant temperature molecular dynamics methods. *The Journal of Chemical Physics* **1984**, *81* (1), 511-519.
35. Hoover, W. G., Canonical dynamics: Equilibrium phase-space distributions. *Physical Review A* **1985**, *31* (3), 1695-1697.
36. Hoover, W. G., Constant-pressure equations of motion. *Physical Review A* **1986**, *34* (3), 2499-2500.
37. Boys, S. F.; Bernardi, F., The calculation of small molecular interactions by the differences of separate total energies. Some procedures with reduced errors. *Molecular Physics* **1970**, *19* (4), 553-566.
38. Sun, H.; Zhong, C.; Brédas, J.-L., Reliable Prediction with Tuned Range-Separated Functionals of the Singlet–Triplet Gap in Organic Emitters for Thermally Activated Delayed Fluorescence. *Journal of Chemical Theory and Computation* **2015**, *11* (8), 3851-3858.
39. Tomasi, J.; Mennucci, B.; Cammi, R., Quantum Mechanical Continuum Solvation Models. *Chemical Reviews* **2005**, *105* (8), 2999-3094.
40. Marcus, R. A., Electron transfer reactions in chemistry theory and experiment. *Journal of Electroanalytical Chemistry* **1997**, *438* (1), 251-259.
41. Coropceanu, V.; Cornil, J.; da Silva Filho, D. A.; Olivier, Y.; Silbey, R.; Brédas, J.-L., Charge Transport in Organic Semiconductors. *Chemical Reviews* **2007**, *107* (4), 926-952.
42. Unger, T.; Wedler, S.; Kahle, F.-J.; Scherf, U.; Bässler, H.; Köhler, A., The Impact of Driving Force and Temperature on the Electron Transfer in Donor–Acceptor Blend Systems. *The Journal of Physical Chemistry C* **2017**, *121* (41), 22739-22752.
43. Benduhn, J.; Tvingstedt, K.; Piersimoni, F.; Ullbrich, S.; Fan, Y.; Tropiano, M.; McGarry, K. A.; Zeika, O.; Riede, M. K.; Douglas, C. J.; Barlow, S.; Marder, S. R.; Neher, D.; Spoltore, D.; Vandewal, K., Intrinsic non-radiative voltage losses in fullerene-based organic solar cells. *Nature Energy* **2017**, *2* (6), 17053.

44. Azzouzi, M.; Yan, J.; Kirchartz, T.; Liu, K.; Wang, J.; Wu, H.; Nelson, J., Nonradiative Energy Losses in Bulk-Heterojunction Organic Photovoltaics. *Physical Review X* **2018**, *8* (3), 031055.
45. Jortner, J., Temperature dependent activation energy for electron transfer between biological molecules. *The Journal of Chemical Physics* **1976**, *64* (12), 4860-4867.
46. Kahle, F.-J.; Rudnick, A.; Bäessler, H.; Köhler, A., How to interpret absorption and fluorescence spectra of charge transfer states in an organic solar cell. *Materials Horizons* **2018**, *5* (5), 837-848.
47. Tummala, N. R.; Zheng, Z.; Aziz, S. G.; Coropceanu, V.; Brédas, J.-L., Static and Dynamic Energetic Disorders in the C60, PC61BM, C70, and PC71BM Fullerenes. *The Journal of Physical Chemistry Letters* **2015**, *6* (18), 3657-3662.
48. Coropceanu, V.; Chen, X.-K.; Wang, T.; Zheng, Z.; Brédas, J.-L., Charge-transfer electronic states in organic solar cells. *Nature Reviews Materials* **2019**, *4* (11), 689-707.
49. Zheng, Z.; Tummala, N. R.; Wang, T.; Coropceanu, V.; Brédas, J.-L., Charge-Transfer States at Organic–Organic Interfaces: Impact of Static and Dynamic Disorders. *Advanced Energy Materials* **2019**, *9* (14), 1803926.
50. Wang, T.; Coropceanu, V.; Brédas, J.-L., All-Polymer Solar Cells: Impact of the Length of the Branched Alkyl Side Chains on the Polymer Acceptors on the Interchain Packing and Electronic Properties in Amorphous Blends. *Chemistry of Materials* **2019**, *31* (16), 6239-6248.
51. Burke, T. M.; Sweetnam, S.; Vandewal, K.; McGehee, M. D., Beyond Langevin Recombination: How Equilibrium Between Free Carriers and Charge Transfer States Determines the Open-Circuit Voltage of Organic Solar Cells. *Advanced Energy Materials* **2015**, *5* (11), 1500123.
52. Wang, T.; Chen, X.-K.; Ashokan, A.; Zheng, Z.; Ravva, M. K.; Brédas, J.-L., Bulk Heterojunction Solar Cells: Impact of Minor Structural Modifications to the Polymer Backbone on the Polymer–Fullerene Mixing and Packing and on the Fullerene–Fullerene Connecting Network. *Advanced Functional Materials* **2018**, *28* (14), 1705868.

CHAPTER 5

Electronic and Charge-Transport Properties of F₆TNAP-based Charge-Transfer Cocrystals

5.1 Introduction

Over the years, organic donor-acceptor co-crystals have garnered extensive research interest due to their potential applications in organic (opto)-electronic devices. They are formed by regular arrangement of two or more molecular moieties in a defined stoichiometry. The assembly of co-crystals is controlled by means of intermolecular interactions between its components, like charge-transfer (CT), π - π , or hydrogen bonding interactions. These materials exhibit properties distinct from those of their individual molecular moieties; for instance, ambipolar charge-transport characteristics were reported on co-crystals made of components that individually exhibited p-type and n-type semiconducting properties.¹⁻⁵

In this Thesis, we mainly focused on binary CT co-crystals where one component acts as an π -electron donor (D) and the other as a π -electron acceptor (A). The selected components are usually coplanar and tightly packed, features that facilitate efficient frontier orbital overlaps and intermolecular interactions in the solid state. We note that the degree of CT is tunable by means of chemical modifications to the molecular backbones in the CT complex. As mentioned in Chapter 1, two major types of molecular stacking motifs are found in CT crystals with 1:1 stoichiometry: (1) mixed stacks, in which D and A molecules alternate along the stacking direction, -D-A-D-A; and (2) segregated stacks, in which D and A molecules form separate stacks, -D-D-D- and -A-A-A. In the absence of disorder, metallic conductivities can be exhibited by CT co-crystals in segregated stacking arrangement. The CT in metallic, segregated co-crystals is normally found

to be midway ($\rho = \text{ca. } 0.5$) between the fully neutral ($\rho = 0$) and fully ionic ($\rho = 1$) limits.^{4, 6-8} However, co-crystals in mixed-stack packing arrangement are usually semiconductors or insulators.^{7, 9-11}

We note that packing of the D and A molecules in co-crystals has significant effect in directing its charge-transport behavior. In mixed-stack systems, apart from through space interactions between adjacent D and A molecules, the electronic interactions along the stacking direction also occurs via a *superexchange* mechanism.¹¹⁻¹⁴ This involves hybridization of frontier molecular orbitals of two closest D [A] molecules with the orbitals of the bridging A [D] molecule; as a result, both electron and hole transport can be promoted along mixed-stacked DA columns. It was reported earlier, based on density functional theory (DFT) calculations, that ambipolar charge-transport properties can be observed in DMQ_tT-F₄TCNQ (DMQ_tT = dimethylquarterthiophene, F₄TCNQ = 2,3,5,6-tetrafluoro-7,7,8,8-tetracyanoquinodimethane), DBTTF-TCNQ (DBTTF = dibenzotetrathiafulvalene, TCNQ = 7,7,8,8-tetracyanoquinodimethane), and, STB-F₄TCNQ (STB = stilbene) CT co-crystals, which is a consequence of similar superexchange electronic couplings for holes and electrons along the stacking direction.¹¹ Also, this feature results in quasi-mirror symmetry between valence and conduction bands in their respective band structures. However, we note that electron-hole symmetry is not a common trend in co-crystals as different degrees of electronic interactions can exist between its components. This issue will be discussed in more detail in the next chapter.

Here, we investigate the electronic-structure and charge-transport properties of co-crystals made of the 1,3,4,5,7,8-hexafluoro-11,11,12,12-tetracyano-2,6-naphthoquinodimethane (F₆TNAP,

also known as F₆TCNNQ) acceptor and six different donor molecules – triphenylene (TP), pyrene (PY), benzo[*b*]benzo[4,5]thieno[2,3-*d*]thiophene (BTBT), benzo[1,2-*b*:4,5-*b'*]dithiophene (BDT), anthracene (ANT), and carbazole (CBZ), see **Figure 5.1**. Experimentally, these co-crystals were synthesized in the groups of Professor Seth Marder at Georgia Institute of Technology and Professor Adam Matzger at the University of Michigan and their crystal structures were determined by single-crystal X-ray diffraction (SCXRD) performed in the group of Professor Tatiana Timofeeva at the New Mexico Highlands University. The predictions on the charge-transport properties obtained from our DFT calculations were correlated with experimental data obtained from field-effect transistor (FET) and space-charge-limited current (SCLC) measurements performed in the group of Professor Oana Jurchescu at the Wake Forest University. This work has been recently published in *Adv. Funct. Mater.*, **2019**, 1904858.¹⁵

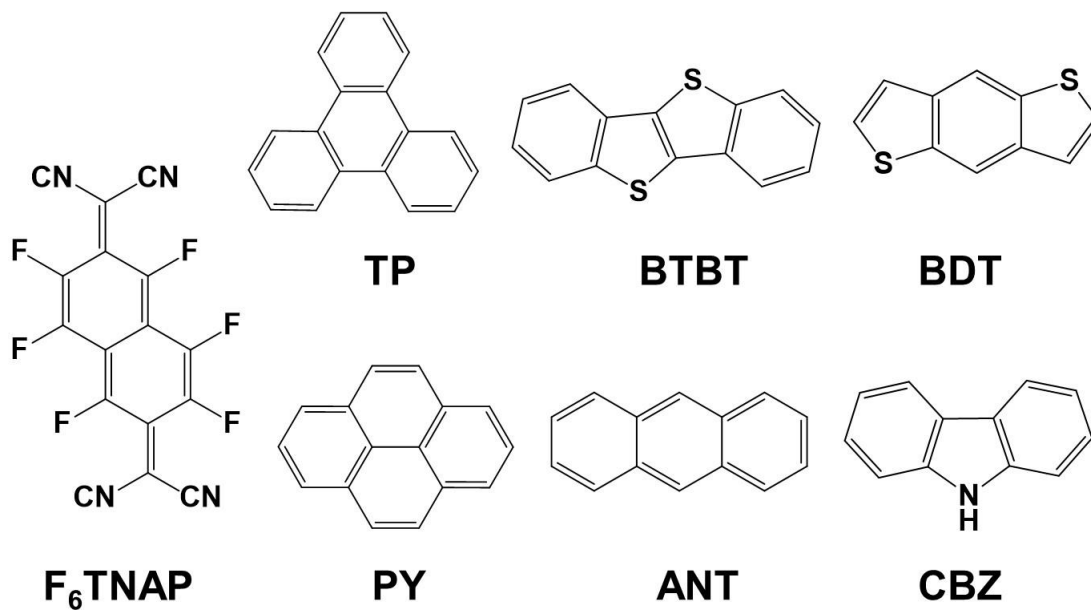


Figure 5.1. Chemical structures of the F₆TNAP acceptor and the TP, BTBT, BDT, PY, ANT, and CBZ donors.

5.2 Methodology

5.2.1. Density Functional Theory Calculations

The molecular energy levels of the individual molecules were calculated using DFT with the B3LYP functional and the 6-31G basis set as implemented in the Gaussian 09.D01 package.¹⁶ The experimental crystal geometries were used for the calculations of the band structure and densities of states of the co-crystals. Uniform 8×4×4, 10×8×6, 8×8×4, 8×8×4, 8×10×4, and 8×8×8 Monkhorst-Pack k-point meshes were employed for the TP:F₆TNAP, BTBT:F₆TNAP, BDT:F₆TNAP, PY:F₆TNAP, ANT:F₆TNAP, and CBZ:F₆TNAP crystals, respectively. All band structure calculations were performed using the CRYSTAL 14 package.^{17, 18}

As explained in Chapter 2, the inverse effective mass tensor for the 3-dimensional crystal is calculated using the expression:

$$\frac{1}{m_{ij}} = \frac{1}{\hbar^2} \left(\frac{d^2 E}{dk_j dk_i} \right) \quad (1)$$

where subscripts i and j represent the Cartesian coordinates in reciprocal space; \hbar is the reduced Planck constant and k , the electron wave-vector. The diagonalization of m_{ij}^{-1} provides the principal components and their orientations. The inverse effective mass tensor was calculated by means of Sperling's centered difference method with $dk = 0.01 \text{ bohr}^{-1}$.

The effective electronic couplings (transfer integrals) between molecules along different directions were calculated by using a molecular-fragment orbital approach combined with a basis-set orthogonalization procedure at the B3LYP/6-31G level of theory. A more simple approach to evaluate the transfer integrals was considered by applying Koopman's theorem¹⁹ (see **Figure 5.2**) where the transfer integrals for holes [electrons] are approximated as half the energy difference

between the highest occupied molecular orbitals (HOMOs) [lowest unoccupied molecular orbitals(LUMOs)], following the relation:

$$t_{mn} = \frac{E_{H[L+1]} - E_{H-1[L]}}{2}$$

where the subscripts H[L+1] and H-1[L] represent the HOMO[LUMO+1] and HOMO-1[LUMO] energies of a dimer, respectively; m and n correspond to the individual molecules forming a dimer.

An essential condition for applicability of this approximation is that the dimer should be symmetric (monomers forming the dimer are the same) with the HOMO and HOMO-1 (as well as LUMO and LUMO+1) molecular orbitals having a similar nature.

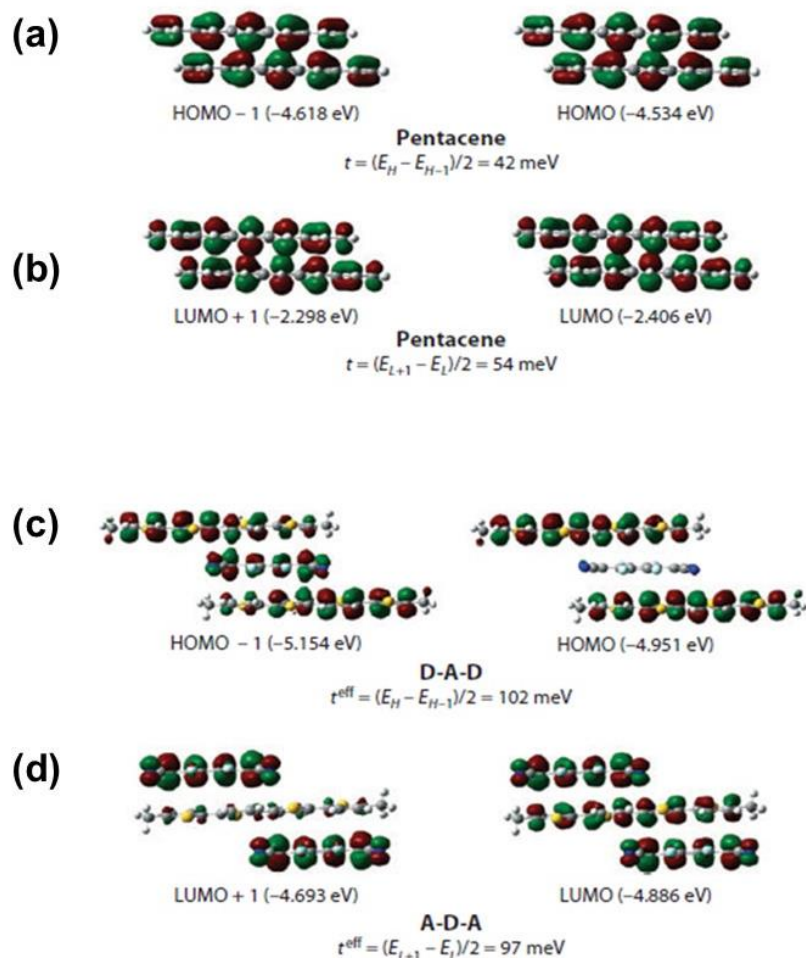


Figure 5.2. Illustration of the energy-splitting estimates of the transfer integrals along the stacking direction for (a) holes and (b) electrons of Pentacene dimer and (c) holes and (d) electrons of DMQ_tT-F4TCNQ co-crystal. Adapted from reference [13]

The energy splitting approach can also be applied in the evaluation of the superexchange coupling, where the molecular orbitals of the bridge molecule (acceptor [donor]) takes part in the electronic coupling between two donors [acceptors] along the stacking direction. Here, instead of the energy levels of a dimer, the molecular orbitals of a cluster need to be considered.¹³ For example, the effective transfer integrals for electrons are calculated from the orbital energies, E , of a A-D-A triad (see **Figure 5.2**) as:

$$t_{electrons}^{eff} = \frac{(E_{L+1}-E_L)}{2} \quad (2)$$

and those for the holes, from the orbital energies of a D-A-D triad as:

$$t_{holes}^{eff} = \frac{(E_H-E_{H-1})}{2} \quad (3)$$

where the subscripts L and L+1 refer to the LUMO and LUMO+1 of the neutral state of the A-D-A triad, and H and H-1 to the HOMO and HOMO-1 of the D-A-D triad. We note that this approach is only applicable in instances where the donor and acceptor molecules are equidistant along the stacking direction. In the cases of co-crystals where the packing along the stacking direction is not symmetric, the effective electronic couplings can be evaluated by means of a projection approach that accounts for the electronic couplings of the transport orbitals with the low energy orbitals of the bridging unit. Here, the t^{eff} values are estimated only for co-crystals with symmetric packing of donor and acceptor molecules along the stacking direction. The calculations of the transfer integrals were carried out using the B3LYP functional and 6-31G basis set with the Gaussian 09.D01 package.¹⁶

5.2.2. Experimental

It is useful to briefly describe the device fabrication process and the electrical measurements carried out in the Jurchescu group. Organic field-effect transistors (OFETs) were obtained by laminating the single crystals over pre-fabricated elastomeric polydimethylsiloxane (PDMS) stamps.²⁰⁻²² In this structure, a 5.5 μm thick gap between the raised and recessed regions of the PDMS stamp served as the air/vacuum gate dielectric. A layer of 40 nm of Au was e-beam evaporated on the patterned PDMS stamp to form electrically isolated electrodes with the source and drain defined on the raised region and the gate on the recessed region of the PDMS stamp. Space-charge-limited current (SCLC) measurements were performed in the same configuration, with the coplanar contacts using non-gated two-point current-voltage measurements. Both OFET and SCLC measurements were performed at room temperature, in the dark and under vacuum using an Agilent 4155C Semiconductor Parameter Analyzer. At least 5 crystals of each type were measured in each case giving consistent results. SCLC measurements were taken in incremental voltage steps of 0.1 V and FET measurements were performed in 1 V steps. Background noise was minimized by integrating the measurements over longer times, during which the instrument averages several measurement samples. The medium integration time was used in all measurements; this is automatically adjusted by the instrument depending on the current level: smaller current requires longer integration time (50 PLC needed for a current of 10 pA, 5 PLC for 1 nA, and 1 PLC for 10 nA to 100 mA, where PLC is the power-line cycle mode and 1 PLC=1/60 s).

5.3 Results and Discussions

5.3.1. Electronic structure, Band-Structure, and Electronic Couplings

The crystal-structure data of all the co-crystals investigated here were deposited in the Cambridge Crystallographic Database (CCDC 1922856-1922863). The selection of the donor molecules was performed based on their oxidation potentials; variations similar to the experimental ones were observed in the DFT derived highest occupied molecular orbital (HOMO) and ionization energies (IE), see **Table 5.1**.

Table 5.1. Electrochemical potentials^a (as measured in the Marder group) and B3LYP/6-31G-calculated orbital energies, adiabatic ionization energy (IE) and electron affinity values (EA) for the donor and acceptor molecules.

Molecule	$E_{1/2}^{+/0}$ / V	$E_{1/2}^{0/-}$ / V	E_{HOMO} / eV	E_{LUMO} / eV	IE / eV	EA / eV
TP	+1.10 ^b	-	-5.81	-0.78	7.3	-
BTBT	+1.00 ^c	-	-5.61	-1.11	7.1	-
BDT	+0.96 ^b	-	-5.56	-0.78	7.3	-
PY	+0.94 ^c	-	-5.32	-1.37	6.8	-
ANT	+0.88 ^d	-	-5.20	-1.53	6.8	-
CBZ	+0.80 ^d	-	-5.43	-0.51	7.1	-
F ₆ TNAP	-	+0.26 ^e	-7.32	-5.43	-	4.3

^a 0.1 M ⁿBu₄NPF₆/CH₂Cl₂ vs FeCp₂⁺⁰; ^b peak potential, E_{pa} , from cyclic voltammetry; ^c $E_{1/2}$ from cyclic voltammetry; ^d peak potential from oxidative differential pulse-voltammetry; ^e peak potential from reductive differential pulse-voltammetry

All the co-crystals are characterized by a 1:1 stoichiometry and crystallize in mixed-stack arrays. The crystals of TP:F₆TNAP, BTBT:F₆TNAP, and CBZ:F₆TNAP belong to triclinic group P1, while the crystals of ANT:F₆TNAP, BDT:F₆TNAP, and PY:F₆TNAP belong to the monoclinic space group P21/c. Structural analyses of TP:F₆TNAP reveal two distinct centroid-to-centroid distances along two different stacks in the asymmetric unit (the distances are 3.799Å and 4.437Å along one stack and 3.747Å and 4.453Å along the other stack). CBZ:F₆TNAP also displays two distinct centroid-to-centroid distances (3.551Å and 3.608Å) along the stacks. However, all the other co-crystals have equally spaced alternating donor and acceptor molecules along the stacks.

The electronic band structures and the densities of states of the six co-crystals are shown in **Figure 5.3**.

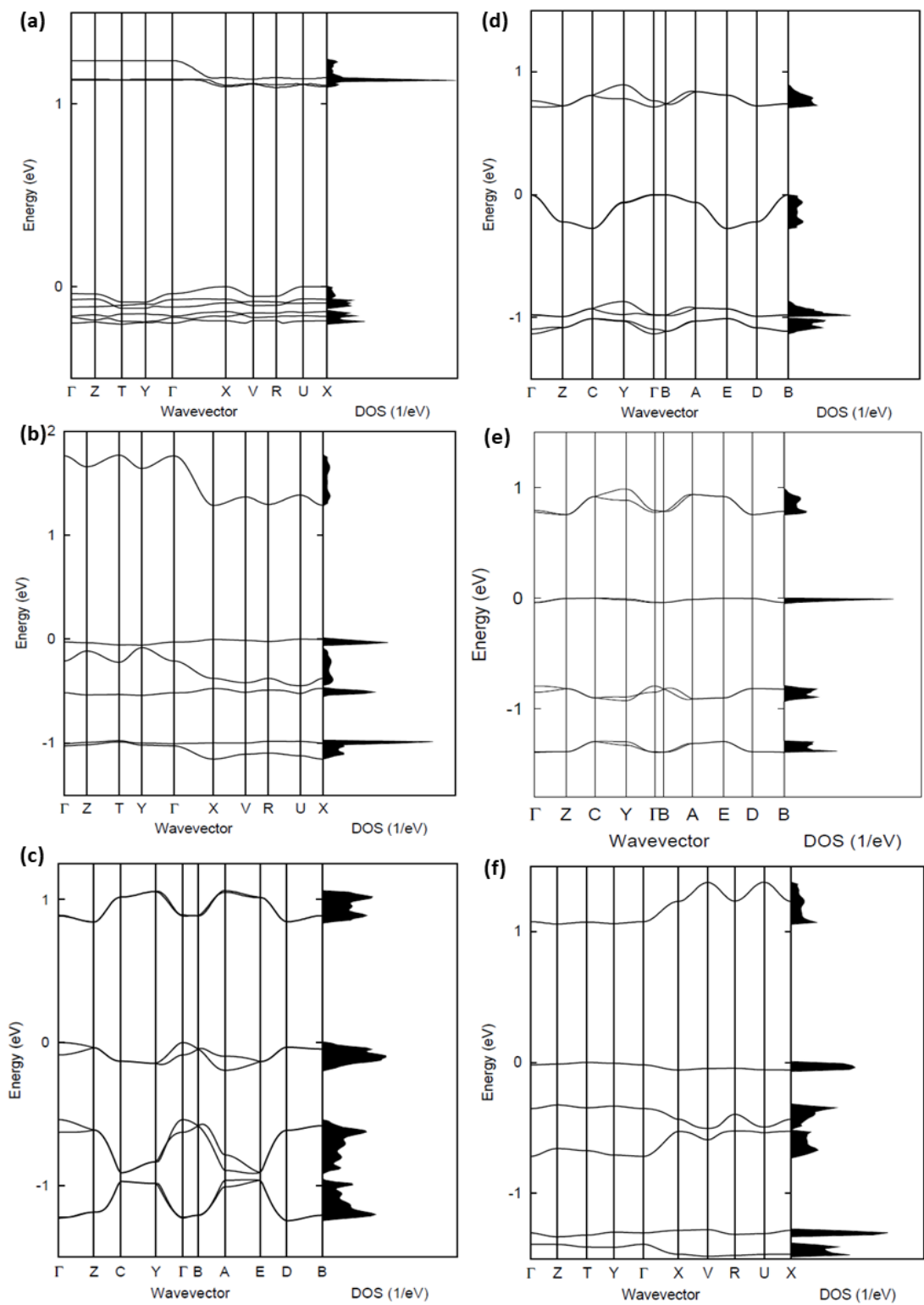


Figure 5.3. Electronic band structure and density of states of the (a) TP:F₆TNAP, (b) BTBT:F₆TNAP, (c) BDT:F₆TNAP, (d) PY:F₆TNAP, (e) ANT:F₆TNAP, and (f) CBZ:F₆TNAP co-crystals. The high-symmetry points in the first Brillouin zone are labelled as: $\Gamma = (0,0,0)$, $Z = (0,0,0.5)$, $T = (0,0.5,0.5)$, $Y = (0,0.5,0)$, $X = (0.5,0,0)$, $V = (0.5,0.5,0)$, $R = (0.5,0.5,0.5)$ and $U = (0.5,0,0.5)$ for the (a, b & f) cases, and $\Gamma = (0,0,0)$, $Z = (0,0.5,0)$, $C = (0.5,0.5,0)$, $Y = (0.5,0,0)$, $B = (0,0,0.5)$, $A = (-0.5,0,0.5)$, $E = (-0.5,0.5,0.5)$ and $D = (0,0.5,0.5)$ for the (c, d, & e) cases. All points are given in fractional coordinates in the reciprocal space. The zero of energy is taken as the top of the valence band.

Table 5.2 compares for each co-crystal the widths of the conduction band (CB) and valence band (VB) along with the effective masses. **Figure 5.4** and **Table 5.3** provide more details regarding effective masses and transfer integrals, respectively.

Table 5.2. B3LYP/6-31G conduction and valence bandwidths (in meV) along with the lowest two effective masses (in units of electron mass in vacuum, m_0).

Cocrystal	Valence Bandwidth	Conduction Bandwidth	Effective Mass, Holes		Effective Mass, Electrons	
			m_1 / m_0	m_2 / m_0	m_1 / m_0	m_2 / m_0
TP:F ₆ TNAP	220	156	1.2	>10	1.4	2.7
BTBT:F ₆ TNAP	57.4	482	4.5	>10	0.6	1.4
BDT:F ₆ TNAP	194	212	1.0	3.1	0.8	>10
PY:F ₆ TNAP	272	181	1.2	5.0	2.8	>10
ANT:F ₆ TNAP	37.2	231	>10	>10	1.8	>10
CBZ:F ₆ TNAP	57.6	318	4.5	>10	0.7	7.6

The largest CB bandwidth of about 480 meV is estimated for BTBT:F₆TNAP (**Figure 5.3b**), which is slightly larger than the highest value (445 meV) computed at the same level of theory for co-crystals based on F₄TCNQ.¹¹ The largest band dispersion is found along the stacking direction and is due to a large effective (super-exchange) transfer integral (76 meV) (see **Figure 5.4**). A relatively large CB bandwidth (320 meV) is also found for CBZ:F₆TNAP. The VBs are significantly narrower than the CBs for BTBT:F₆TNAP, ANT:F₆TNAP, and CBZ:F₆TNAP. For

BDT:F₆TNAP, the VB approaches the CB in width, while for TP:F₆TNAP and PY:F₆TNAP the VB is somewhat wider than the CB. Thus, the present systems do not exhibit the usual “mirror” symmetry between VBs and CBs found in many previously studied co-crystals.^{12, 23} The lack of mirror symmetry is an indication that the super-exchange coupling is not dominated by the interaction involving only the donor and acceptor molecular frontier orbitals (a situation found in many CT systems) but rather contains contributions from more molecular levels. As a result, the super-exchange transfer integrals, t^{eff} , for holes can be very different than for electrons; in the present systems, overall these couplings are smaller for holes than for electrons (see **Figure 5.4** and **Table 5.3**).¹² We also note that the super-exchange couplings depend on the transfer integrals (t_{DA}) between donor and acceptor frontier orbitals and the related energy gaps (ΔE_{DA}); thus, in the weak electronic coupling limit, they can be expressed as:

$$t^{eff} = t_{DA}^2 / \Delta E_{DA} \quad (4)$$

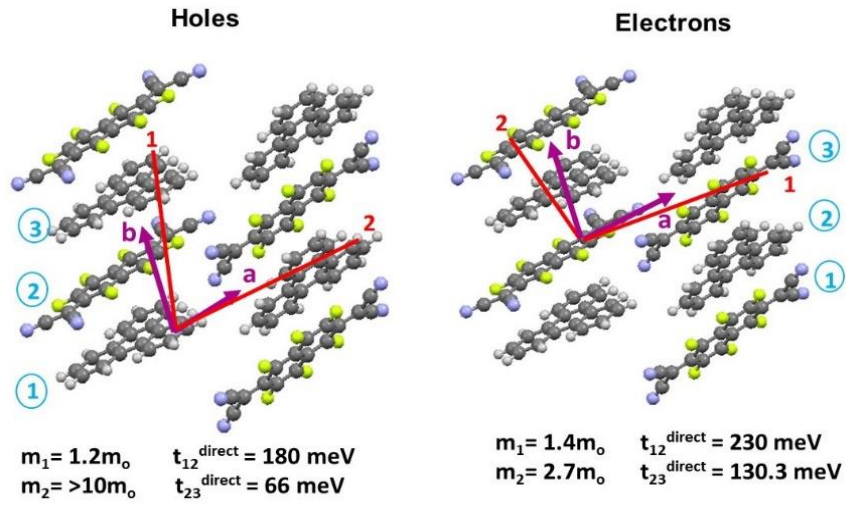
The DFT results for the considered systems show that despite a 0.5 eV variation in the ΔE_{DA} values, the t_{DA} integrals that are controlled by the crystal packing, have a stronger effect on the relative super-exchange couplings (see **Table 5.3**).

Table 5.3. B3LYP/6-31G estimates of ΔE_{DA} (computed using the IP and EA values from Table 5.1), t_{DA} , and super-exchange couplings for holes (t_h^{eff}) and electrons (t_e^{eff}).

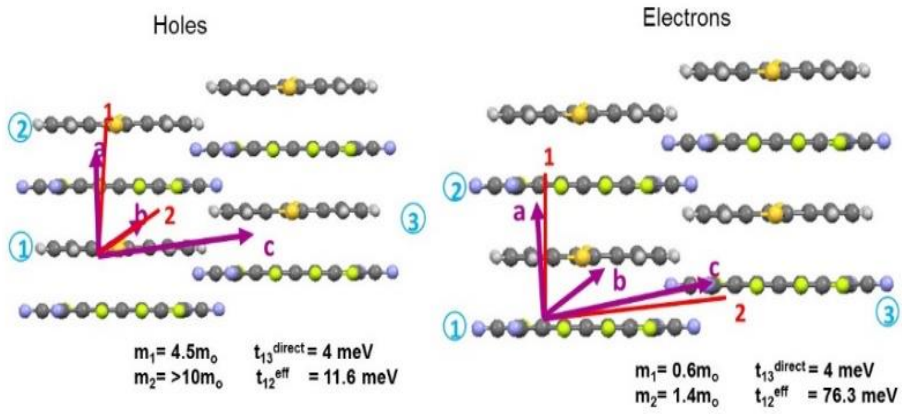
Co-crystals	ΔE_{DA} (eV)	t_{DA} (meV)	t_h^{eff} (meV)	t_e^{eff} (meV)
TP:F6TNAP	3.0	185.4/66 230/130.3	-	-
BTBT:F6TNAP	2.8	300.5	11.6	76.3
BDT:F6TNAP	3.0	163.5	24.5	34.6
PY:F6TNAP	2.5	186.4	9.2	13.6
ANT:F6TNAP	2.5	125.3	6.8	30
CBZ:F6TNAP	2.8	179.3/101.3	-	-

In line with the results obtained for the band dispersions and transfer integrals, the smallest effective masses for electrons are found along the stacking direction. Except in the case of PY:F₆TNAP, the effective mass for electrons are smaller than $2m_0$, where m_0 is the electron mass in vacuum. In particular, very small effective-mass values of $0.64 m_0$ and $0.75 m_0$ are found for BTBT:F₆TNAP and CBZ:F₆TNAP, respectively. Small effective masses of $1.25 m_0$, $1.00 m_0$, and $1.25 m_0$ are also found for holes in TP:F₆TNAP, BDT:F₆TNAP, and PY:F₆TNAP, respectively. However, in contrast to what is found for electrons, the smallest effective masses for holes are found along the stacking direction only in BDT:F₆TNAP, while in the TP:F₆TNAP and PY:F₆TNAP cocrystals, they are found along directions approximately perpendicular to the stacking direction (see **Figure 5.4** and **Table 5.4**); this is a consequence in these systems of direct through-space transfer integrals that exceed the super-exchange couplings. In most cases, the charge carriers are characterized by a small effective mass only along one crystal direction. However, two small components of the effective masses are found for electrons in TP:F₆TNAP and BTBT:F₆TNAP and for holes in BDT:F₆TNAP, which suggests that charge transport in these cases has a two-dimensional character. For comparison, we note that the calculated effective masses for holes and electrons in pentacene, which is one of the most extensively studied single-component systems in organic electronics, are ca. $1.5 m_0$ and $1.6 m_0$, respectively.¹⁴

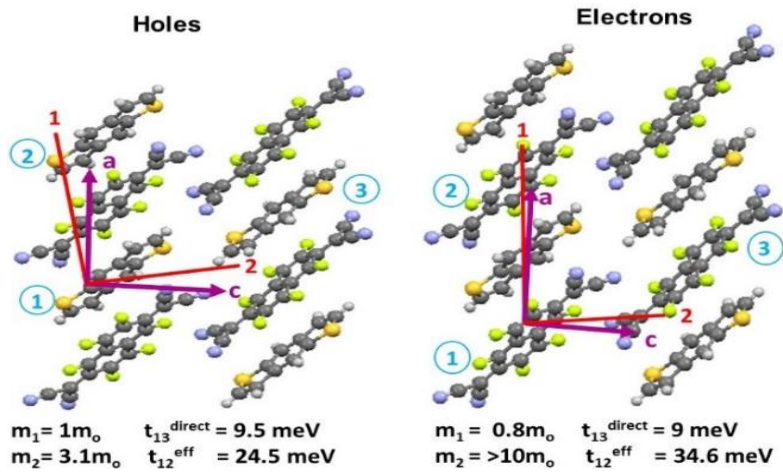
(a)



(b)



(c)



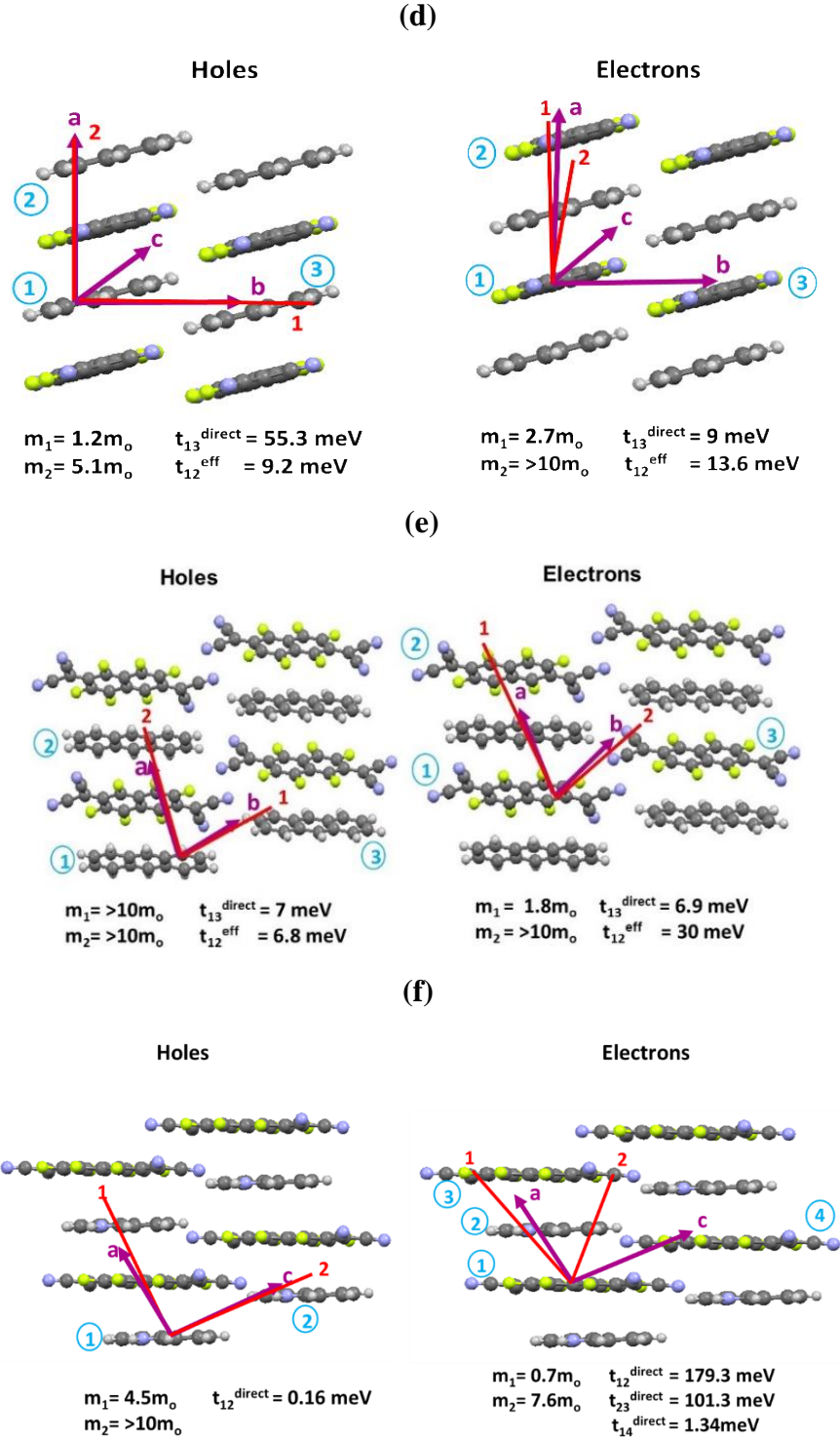


Figure 5.4. Illustrations of the largest transfer integrals and smallest effective masses for holes and electrons in: (a) TP:F₆TNAP, (b) BTBT:F₆TNAP, (c) BDT:F₆TNAP, (d) PY:F₆TNAP; (e) ANT:F₆TNAP, and (f) CBZ:F₆TNAP. The red lines indicate the directions along which the principal components of m_{ji}^{-1} have the smallest values of effective mass.

Table 5.4. Hole and electron effective masses, m (in units of the free electron mass at rest, m_0).

Crystal		m / m_0	Parallel to
TP:F ₆ TNAP	Holes at X (0.5, 0, 0)	1.2	b+0.35a+0.005c
		10.77	a-0.05b-0.017c
		1129.9	c+0.49a+0.48b
	Electrons at R(0.5, 0.5, 0.5)	1.4	a+0.13b+0.23c
		2.7	b-0.81a+0.97c
		4.9	b+0.49a-0.46c
BTBT:F ₆ TNAP	Holes at U (0.5, 0, 0.5)	4.5	a-0.27b-0.03c
		11.4	b+0.7a+0.36c
		107.8	c-0.02a-0.54c
	Electrons at X (0.5,0,0)	0.64	a+0.29b+0.31c
		1.40	c+0.77b-0.77a
		171.9	b+0.1a-0.33c
BDT:F ₆ TNAP	Holes at Γ (0, 0, 0)	1.01	a+0.2c
		3.06	c-0.37a
		20.0	b
	Electrons at Z (0, 0.5, 0)	0.81	a+0.006c
		18.5	b+0.2a
		30.0	b
PY:F ₆ TNAP	Holes at Γ (0, 0, 0)	1.25	b
		5.01	a+0.04c
		35.13	c+0.078a
	Electrons at (0, 0.2, 0)	2.76	a+0.36c
		10.13	a-0.43c
		120	b
ANT:F ₆ TNAP	Holes at E (-0.5, 0.5, 0.5)	17.1	b
		468.6	a-0.6c
		158.7	a+0.18c
	Electrons at D (0, 0.5, 0.5)	1.81	a+0.0002c
		12.4	b
		240.1	c+0.16a
CBZ:F ₆ TNAP	Holes at Γ (0, 0, 0)	4.56	a-0.05b
		60.00	c-0.06a-0.14b
		70.77	b-0.13a
	Electrons at (0, 0.035, 0.5)	0.75	a-0.24b+0.25c
		7.61	c-0.45a+0.22b
		60.83	b+0.19a-0.22c

Overall, the calculations predict good electron-transport properties in all six cocrystals, particularly for the BTBT:F₆TNAP and CBZ:F₆TNAP cocrystals, while good hole-transport

properties are also predicted for TP:F₆TNAP, BDT:F₆TNAP, and PY:F₆TNAP, which suggests that these three co-crystals could display ambipolar transport.

5.3.2. Electrical properties

In this Section, we briefly describe the experimental data from the Jurchescu group on the charge-transport properties of the co-crystals and correlate them with the results of our DFT calculations. As a first step, two-terminal current-voltage characteristics were measured for all six co-crystals and the charge-carrier mobility values, μ , were evaluated using the space-charge-limited current (SCLC) method.²⁴⁻³¹ **Figure 5.5** shows current-voltage characteristics of BTBT:F₆TNAP and CBZ:F₆TNAP as representative examples. The resistivity (ρ) was calculated from the low-voltage regime of the curve, in which the current density (J) and the applied voltage (V) are directly proportional ($J \propto V$, indicated by the blue line). Charge-carrier mobility values (μ) were then estimated from the SCLC regime in which J has a quadratic dependence on V ($J \propto V^2$), by using the Mott-Gurney law²⁴:

$$J_{\text{SCLC}} = \frac{9}{8} \frac{m_e e_r e_0 q}{L^3} V^2 \quad (5)$$

where L is the distance between the contacts, ϵ_r is the relative permittivity of the semiconductor (approximated to be 3), ϵ_0 is the permittivity of free space, and θ the ratio of free charge carriers to total charge carriers (assumed to be 1).

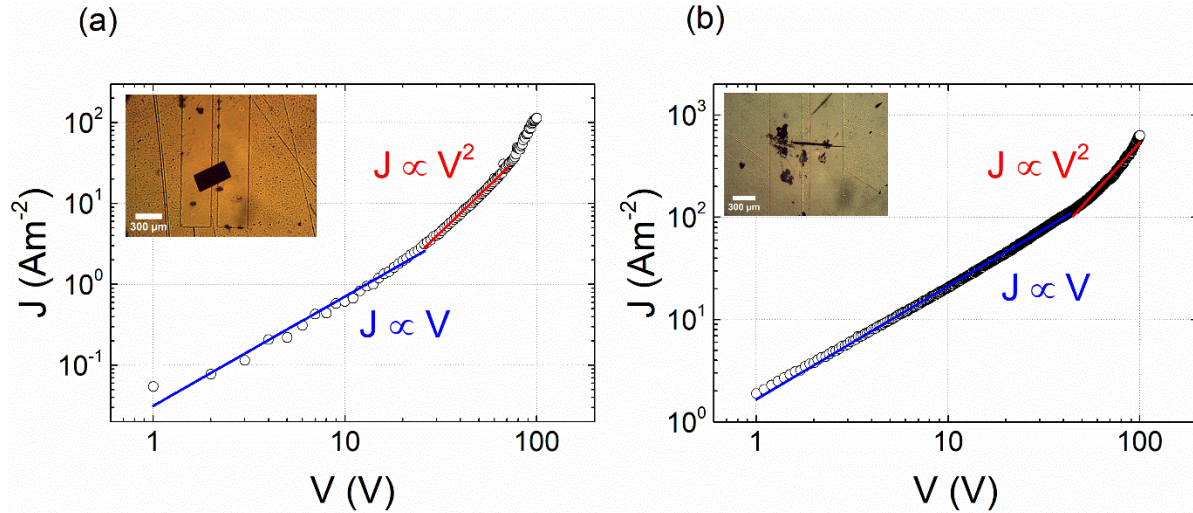


Figure 5.5. SCLC measurements for the representative examples of the (a) BTBT:F₆TNAP and (b) CBZ:F₆TNAP co-crystals. Inset shows an optical micrograph of a crystal laminated across the electrodes. The blue and red solid lines represent linear fits for the ohmic and SCLC regimes, respectively. Measurements conducted in the Jurchescu group.

Table 5.5 lists the values of μ obtained for all six cocrystals. We note that there are significant uncertainties in the estimation of the μ values from the SCLC measurements, which arise from the assumed values of θ and ε_r and with measurements of crystal thickness; hence, here, we report the order of magnitude rather than actual values. The SCLC mobility values fall into two groups: The TP:F₆TNAP, BTBT:F₆TNAP, PY:F₆TNAP, and CBZ:F₆TNAP co-crystals exhibit mobilities in the $0.1 - 1 \text{ cm}^2 \text{ V}^{-1} \text{ s}^{-1}$ range, while the mobilities are substantially lower for BDT:F₆TNAP and ANT:F₆TNAP. Overall, SCLC mobility values exceeding $1 \text{ cm}^2 \text{ V}^{-1} \text{ s}^{-1}$ are observed only for BTBT:F₆TNAP and CBZ:F₆TNAP, for which the DFT-estimated conduction bandwidths are the largest among all co-crystals considered in this work.

Table 5.5. Summary of the electrical properties evaluated from the SCLC and OFET measurements conducted in the Jurchescu group.

Cocrystal	SCLC Measurements ^a		OFET Characteristics
	$\mu_{\text{SCLC}} / \text{cm}^2 \text{V}^{-1} \text{s}^{-1}$	$\mu_{\text{th}} / \text{cm}^2 \text{V}^{-1} \text{s}^{-1}$	$\mu_{\text{e}} / \text{cm}^2 \text{V}^{-1} \text{s}^{-1}$
TP:F ₆ TNAP	10 ⁻¹	-	-
BTBT:F ₆ TNAP	10 ⁰	-	-
BDT:F ₆ TNAP	10 ⁻⁴	-	-
PY:F ₆ TNAP	10 ⁻¹	$(1.4 \pm 0.42) \times 10^{-2}$	$(2.0 \pm 0.71) \times 10^{-2}$
ANT:F ₆ TNAP	10 ⁻³	$(3.8 \pm 0.14) \times 10^{-4}$	$(6.6 \pm 0.49) \times 10^{-4}$
CBZ:F ₆ TNAP	10 ¹	-	-

^aReported as an order of magnitude because these values are estimated with numerous approximations.

The electrical properties of the co-crystals were also evaluated using bottom-gate bottom-contact organic field-effect transistors (OFETs). ANT:F₆TNAP and PY:F₆TNAP crystals yielded functional FETs, while for the other systems, the attempts to fabricate OFETs were unsuccessful, most likely due to the high surface roughness of these crystals. **Figure 5.6** shows the current between the source and drain electrodes, I_{D} , as a function of gate-source voltage (V_{GS}) at constant source-drain voltage, $V_{\text{DS}} = -60 \text{ V}$ (left panel) and $V_{\text{DS}} = +60 \text{ V}$ (right panel) for ANT:F₆TNAP and PY: F₆TNAP devices; the data clearly indicate ambipolar transport. The electron and hole charge carrier mobilities were evaluated in the respective saturation regimes using standard OFET equations and are given in **Table 5.5**.

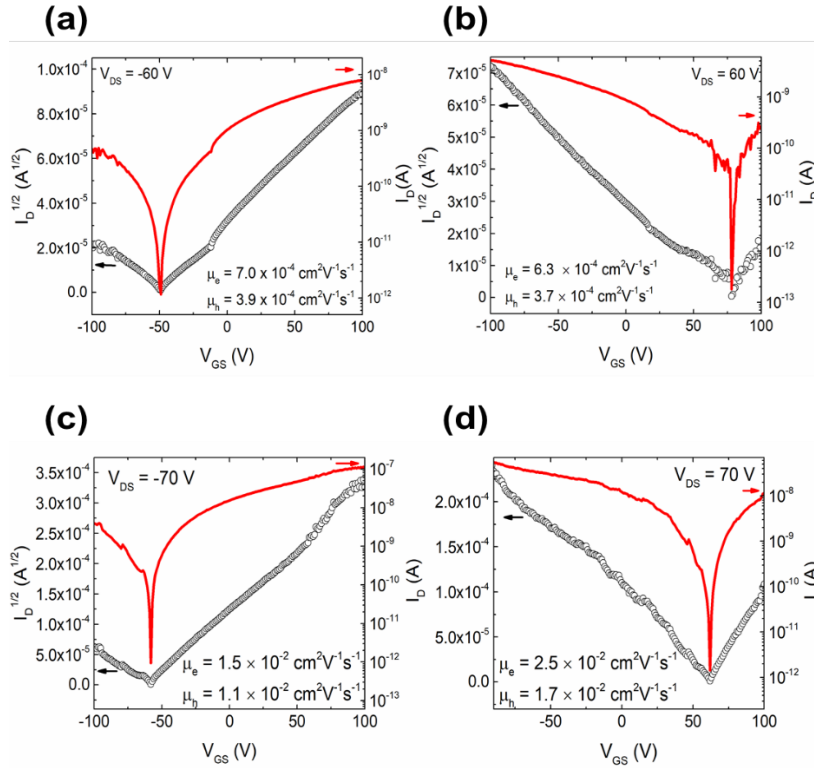


Figure 5.6. Evolution of the drain current, I_D as a function of gate-source voltage, V_{GS} (a) at $V_{DS} = -60$ V, and (b) $V_{DS} = 60$ V for ANT:F₆TNAP and (c) at $V_{DS} = -70$ V, and (d) $V_{DS} = 70$ V for PY:F₆TNAP. The left axis shows the square root of I_D while the right axis shows I_D on a logarithmic scale. The reliability factors for the graphs in panels are (a) 87%, (b) 94%, (c) 97% and (d)70%, respectively. Measurements conducted in the Jurschescu group.

The ambipolarity observed for the PY:F₆TNAP cocrystal is consistent with the band-structure calculations, which indicate large widths for both VB and CB. On the other hand, the calculated VB bandwidth for the ANT:F₆TNAP cocrystal is much lower than the CB bandwidth, apparently at odds with the ambipolarity suggested by the FET mobility data; this might be due to preferential trapping of electrons at the dielectric interface, which reduces electron mobility. The estimated μ_{SCLC} values for BTBT:F₆TNAP and CBZ:F₆TNAP are broadly consistent with calculated bandwidths or effective masses; however, the trends in μ_{SCLC} values for the other cocrystals show no obvious correlation with the trends in the calculated bandwidths or effective masses.

5.3.3 Degree of charge transfer

Having discussed the charge-transport properties of six F₆TNAP acceptor-based co-crystals, it is of interest to understand whether these properties correlate with the degree of charge-transfer (ρ) in these systems. Several reports have underlined the sensitivity of certain vibrational modes to charge-transfer excitations.³²⁻³⁷ In particular, the nitrile (C≡N) stretching frequencies in cyano-functionalized acceptors (like TCNQ, F₂TCNQ, F₄TCNQ or F₆TNAP) have often been used to estimate this parameter.³⁸⁻⁴² In this work, the relevant vibrational modes were identified from the IR spectra taken in the Marder group for all the co-crystals (see **Figure 5.7**) and ρ was estimated from the highest-energy stretching modes of C≡N (see **Table 5.6**).

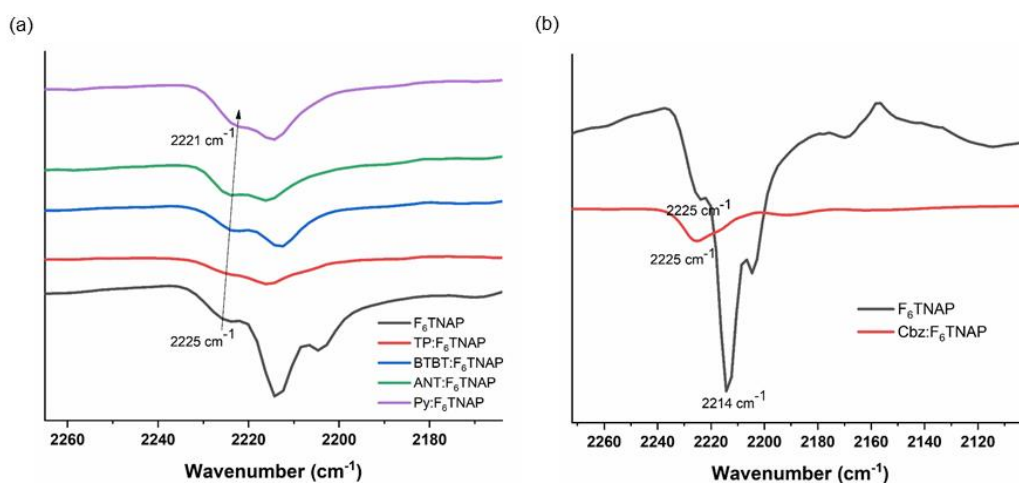


Figure 5.7. IR spectra comparing the nitrile stretching modes of F₆TNAP with (a) TP:F₆TNAP, BTBT:F₆TNAP, ANT:F₆TNAP, PY:F₆TNAP cocrystals, and (b) CBZ:F₆TNAP. Measurements conducted in the Marder group.

The degree of charge-transfer was then estimated according to:^{40, 42-47}

$$r = \frac{2Dn}{n_0 \left(1 - n_1^2 / n_0^2\right)} \quad (6)$$

where $\Delta\nu = \nu_0 - \nu_{CT}$ and ν_0 , ν_1 , and ν_{CT} denote the highest nitrile stretching frequencies of F₆TNAP in the neutral state ($\rho = 0$, $\nu_0 = 2225 \text{ cm}^{-1}$), the F₆TNAP anion ($\rho = 1$, $\nu_1 = 2194 \text{ cm}^{-1}$), and the CT

co-crystal, respectively. In the case of CBZ:F₆TNAP, the value of ν_{CT} was found to be equivalent to that of ν_0 , precluding its use in estimating ρ .

Table 5.6. Highest nitrile stretching frequencies (cm⁻¹) for F₆TNAP, cocrystals, and F₆TNAP⁻, ν_0 , ν_{CT} , and ν_1 , respectively, and along with estimated degree of charge transfer (ρ) for cocrystals.^a

Cocrystal	ν_0	ν_{CT}	ν_1	ρ
TP:F ₆ TNAP	2225	2223	2194	0.06±0.03
BTBT:F ₆ TNAP	2225	2222	2194	0.09±0.03
BDT:F ₆ TNAP	2225	2223	2194	0.06±0.03
PY:F ₆ TNAP	2225	2221	2194	0.13±0.03
ANT:F ₆ TNAP	2225	2223	2194	0.06±0.03

Although the method described above is widely used in estimating ρ , we note that there are several inconsistencies within this approximation. First of all, the IR spectra of the neat F₆TNAP crystal shows three peaks instead of the two that are expected. As seen from Figure 7, there occurs a sharp central peak along with two weak-intensity peaks. We note that the F₆TNAP crystal contains two molecules per unit cell. Therefore, these results indicate that interactions between the same kinds of molecules could also largely impact the vibrational properties; thus, the change in the vibrational energies when going from a single-component crystal to a D-A crystal should not be expected to be related only with the amount of electron transfer. Therefore, the use of nitrile stretching frequencies or other frequencies to access the degree of charge transfer could be, in general, challenging and lead to inconsistencies.

The DFT simulated infra-red vibrational frequencies of C≡N stretching modes of F₆TNAP in the co-crystals present a similar picture (see **Figure 5.8**) with multiple peaks largely differing in intensities. As discussed above, the higher-energy modes can correspond to interactions between molecules along different directions or a linear combination of different vibrations and need not necessarily arise solely from absorption by the C≡N stretching modes of F₆TNAP.

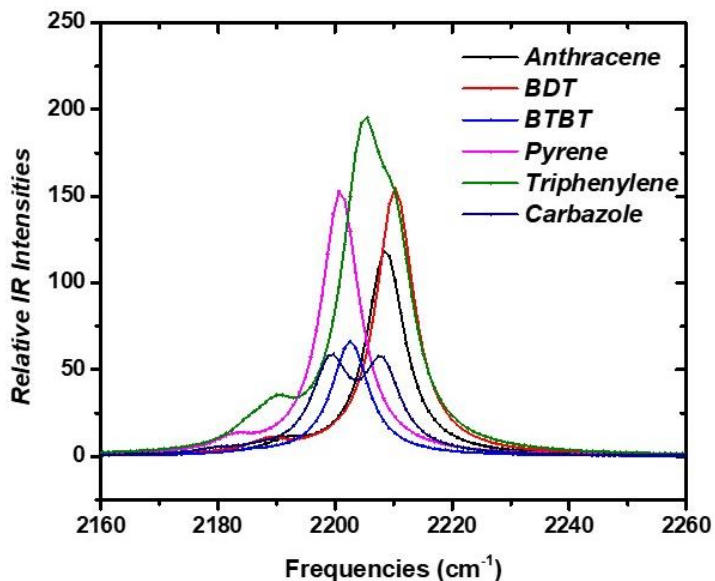


Figure 5.8. DFT simulated (IR) vibrational frequencies (scaled by 0.9614) comparing the C≡N stretching modes of F₆TNAP in the charge-transfer complexes, as calculated at the B3LYP/6-31G level.

Clearly in addition to IR or Raman data, other approaches should be used to provide a reliable estimation of ρ . On the theory side, in order to estimate the degree of charge-transfer, an approach based on Mulliken charges can be used.²³ **Table 5.7** collects the absolute values of charge transfer for all the co-crystals estimated in this way. We note that the charge-transfer values are significantly smaller than those estimated from the IR vibrational modes.

Table 5.7. Degree of charge transfer in the co-crystals based on Mulliken charges.

co-crystal	ρ (calculated)
TP: F₆TNAP	0.019
BTBT: F₆TNAP	0.050
BDT: F₆TNAP	0.014
PY: F₆TNAP	0.018
ANT: F₆TNAP	0.016
CBZ: F₆TNAP	0.053

Here, the largest magnitude of charge transfer is observed for the BTBT: F₆TNAP and CBZ: F₆TNAP co-crystals. We recall from our electronic-structure calculations that these systems show the largest conduction bandwidths and the lowest effective masses for the electrons along the stacking direction. Additionally, the strong electronic couplings along the stacking directions and the large magnitude of the experimental SCLC mobilities affirm the strong nature of the CT interactions in these two systems. On the other hand, TP: F₆TNAP, BDT: F₆TNAP, PY: F₆TNAP and ANT: F₆TNAP display similar ρ values, which indicate a similar nature of CT interactions in these systems. The DFT prediction of ambipolar charge-transport characteristics in TP: F₆TNAP, BDT: F₆TNAP and PY: F₆TNAP as well as the experimental OFET ambipolar charge-transfer characteristics for PY: F₆TNAP and ANT: F₆TNAP are generally consistent with this result. Overall, while a quantitative picture of charge transfer cannot be derived, our work provides a qualitative description that is consistent with the experimental observations.

5.4. Conclusions

We have investigated the electronic and charge-transport properties of six co-crystals of F₆TNAP with coplanar donors using a combination of DFT calculations, IR spectroscopy, and electrical measurements. The DFT calculations point to large conduction bandwidths and small effective masses for electrons along the stacking direction for all six co-crystals, which suggests good electron-transport properties. Large valence bandwidths and low effective masses for holes are also found for the TP:F₆TNAP, BDT:F₆TNAP, and PY:F₆TNAP co-crystals. Based on these results, ambipolar charge-transport properties are predicted for three of the six co-crystals (TP:F₆TNAP, BDT:F₆TNAP and PY:F₆TNAP); experimentally, only two of these co-crystals yield functioning OFET devices (PY:F₆TNAP and ANT: F₆TNAP) displaying ambipolar charge transport. Charge carrier mobilities are found to be in excess of $10^{-1} \text{ cm}^2\text{V}^{-1}\text{s}^{-1}$ for four of the co-crystals; these values are comparable to the highest values reported in the literature for other CT complexes. We also evaluated the degree of charge transfer using IR spectroscopy data as well as DFT calculations and found qualitative trends that are in line with the charge-transport behavior of the co-crystals.

5.5. References

1. Zhan, X.; Facchetti, A.; Barlow, S.; Marks, T. J.; Ratner, M. A.; Wasielewski, M. R.; Marder, S. R., Rylene and Related Diimides for Organic Electronics. *Advanced Materials* **2011**, *23* (2), 268-284.
2. Mohebbi, A. R.; Yuen, J.; Fan, J.; Munoz, C.; Wang, M. f.; Shirazi, R. S.; Seifert, J.; Wudl, F., Emeraldicene as an Acceptor Moiety: Balanced-Mobility, Ambipolar, Organic Thin-Film Transistors. *Advanced Materials* **2011**, *23* (40), 4644-4648.
3. Zhao, Y.; Guo, Y.; Liu, Y., 25th Anniversary Article: Recent Advances in n-Type and Ambipolar Organic Field-Effect Transistors. *Advanced Materials* **2013**, *25* (38), 5372-5391.
4. Hasegawa, T.; Takeya, J., Organic field-effect transistors using single crystals. *Science and Technology of Advanced Materials* **2009**, *10* (2), 024314.
5. Zhang, J.; Xu, W.; Sheng, P.; Zhao, G.; Zhu, D., Organic Donor–Acceptor Complexes as Novel Organic Semiconductors. *Accounts of Chemical Research* **2017**, *50* (7), 1654-1662.
6. Ferraris, J. P.; Poehler, T. O.; Bloch, A. N.; Cowan, D. O., Synthesis of the highly conducting organic salt: tetramethyltetrathiofulvalenium - tetracyano-p-quinodimethanide. *Tetrahedron Letters* **1973**, *14* (27), 2553-2556.
7. Goetz, K. P.; Vermeulen, D.; Payne, M. E.; Kloc, C.; McNeil, L. E.; Jurchescu, O. D., Charge-transfer complexes: new perspectives on an old class of compounds. *Journal of Materials Chemistry C* **2014**, *2* (17), 3065-3076.
8. Mori, T.; Kawamoto, T., Organic conductors—from fundamentals to nonlinear conductivity. *Annual Reports Section "C" (Physical Chemistry)* **2007**, *103* (0), 134-172.
9. Pope, M.; Swenberg, C. E., Electronic Processes in Organic Crystals and Polymers. **1999**.
10. Saito, G.; Pac, S.-S.; Drozdova, O. O., First metallic DA alternating charge transfer complex: (HMTTeF)(Et₂TCNQ)(THF)_x. *Synthetic Metals* **2001**, *120* (1), 667-670.
11. Zhu, L.; Yi, Y.; Li, Y.; Kim, E.-G.; Coropceanu, V.; Brédas, J.-L., Prediction of Remarkable Ambipolar Charge-Transport Characteristics in Organic Mixed-Stack Charge-Transfer Crystals. *Journal of the American Chemical Society* **2012**, *134* (4), 2340-2347.
12. Zhu, L.; Yi, Y.; Fonari, A.; Corbin, N. S.; Coropceanu, V.; Brédas, J.-L., Electronic Properties of Mixed-Stack Organic Charge-Transfer Crystals. *The Journal of Physical Chemistry C* **2014**, *118* (26), 14150-14156.
13. Coropceanu, V.; Li, H.; Winget, P.; Zhu, L.; Brédas, J.-L., Electronic-Structure Theory of Organic Semiconductors: Charge-Transport Parameters and Metal/Organic Interfaces. *Annual Review of Materials Research* **2013**, *43* (1), 63-87.
14. Coropceanu, V.; Li, Y.; Yi, Y.; Zhu, L.; Brédas, J.-L., Intrinsic charge transport in single crystals of organic molecular semiconductors: A theoretical perspective. *MRS Bulletin* **2013**, *38* (1), 57-64.
15. Dasari, R. R.; Wang, X.; Wiscons, R. A.; Haneef, H. F.; Ashokan, A.; Zhang, Y.; Fonari, M. S.; Barlow, S.; Coropceanu, V.; Timofeeva, T. V.; Jurchescu, O. D.; Brédas, J.-L.; Matzger, A. J.; Marder, S. R., Charge-Transport Properties of F6TNAP-Based Charge-Transfer Cocrystals. *Advanced Functional Materials* **2019**, *0* (0), 1904858.
16. Frisch, M. J.; Trucks, G. W.; Schlegel, H. B.; Scuseria, G. E.; Robb, M. A.; Cheeseman, J. R.; Scalmani, G.; Barone, V.; Mennucci, B.; Petersson, G. A.; Nakatsuji, H.; Caricato, M.; Li, X.; Hratchian, H. P.; Izmaylov, A. F.; Bloino, J.; Zheng, G.; Sonnenberg, J. L.; Hada, M.; Ehara, M.; Toyota, K.; Fukuda, R.; Hasegawa, J.; Ishida, M.; Nakajima, T.;

- Honda, Y.; Kitao, O.; Nakai, H.; Vreven, T.; Montgomery Jr., J. A.; Peralta, J. E.; Ogliaro, F.; Bearpark, M. J.; Heyd, J.; Brothers, E. N.; Kudin, K. N.; Staroverov, V. N.; Kobayashi, R.; Normand, J.; Raghavachari, K.; Rendell, A. P.; Burant, J. C.; Iyengar, S. S.; Tomasi, J.; Cossi, M.; Rega, N.; Millam, N. J.; Klene, M.; Knox, J. E.; Cross, J. B.; Bakken, V.; Adamo, C.; Jaramillo, J.; Gomperts, R.; Stratmann, R. E.; Yazyev, O.; Austin, A. J.; Cammi, R.; Pomelli, C.; Ochterski, J. W.; Martin, R. L.; Morokuma, K.; Zakrzewski, V. G.; Voth, G. A.; Salvador, P.; Dannenberg, J. J.; Dapprich, S.; Daniels, A. D.; Farkas, Ö.; Foresman, J. B.; Ortiz, J. V.; Cioslowski, J.; Fox, D. J., Gaussian 09, Revision D. 01, Gaussian, Inc.: Wallingford, CT **2009**.
17. Dovesi, R.; Orlando, R.; Erba, A.; Zicovich-Wilson, C. M.; Civalleri, B.; Casassa, S.; Maschio, L.; Ferrabone, M.; De La Pierre, M.; D'Arco, P.; Noël, Y.; Causà, M.; Rérat, M.; Kirtman, B., CRYSTAL14: A program for the ab initio investigation of crystalline solids. *International Journal of Quantum Chemistry* **2014**, *114* (19), 1287-1317.
 18. Dovesi, R.; Erba, A.; Orlando, R.; Zicovich-Wilson, C. M.; Civalleri, B.; Maschio, L.; Rérat, M.; Casassa, S.; Baima, J.; Salustro, S.; Kirtman, B., Quantum-mechanical condensed matter simulations with CRYSTAL. *Wiley Interdisciplinary Reviews: Computational Molecular Science* **2018**, *8* (4), e1360.
 19. Koopmans, T., About the assignment of wave functions and eigenvalues to the individual electrons of an atom. *Physica* **1934**, *1* (1), 104-113.
 20. Sundar, V. C.; Zaumseil, J.; Podzorov, V.; Menard, E.; Willett, R. L.; Someya, T.; Gershenson, M. E.; Rogers, J. A., Elastomeric Transistor Stamps: Reversible Probing of Charge Transport in Organic Crystals. *Science* **2004**, *303* (5664), 1644.
 21. Menard, E.; Podzorov, V.; Hur, S. H.; Gaur, A.; Gershenson, M. E.; Rogers, J. A., High-Performance n- and p-Type Single-Crystal Organic Transistors with Free-Space Gate Dielectrics. *Advanced Materials* **2004**, *16* (23-24), 2097-2101.
 22. Pereira, M. J.; Ayela, C.; Hirsch, L.; Dufour, I.; Briseno, A.; Matta, M.; Olivier, Y.; Muccioli, L.; Crosby, A.; Wantz, G. In *Pressure sensor based on organic single crystal air-gap transistor*, 2017 19th International Conference on Solid-State Sensors, Actuators and Microsystems (TRANSDUCERS), 18-22 June 2017; 2017; pp 1163-1166.
 23. Behera, R. K.; Goud, N. R.; Matzger, A. J.; Brédas, J.-L.; Coropceanu, V., Electronic Properties of 1,5-Diaminonaphthalene:Tetrahalo-1,4-benzoquinone Donor-Acceptor Cocrystals. *The Journal of Physical Chemistry C* **2017**, *121* (42), 23633-23641.
 24. Mott, N. F.; Gurney, R. W., *Electronic processes in ionic crystals*. Oxford, Clarendon Press: Oxford, 1940.
 25. Rose, A., Space-Charge-Limited Currents in Solids. *Physical Review* **1955**, *97* (6), 1538-1544.
 26. Rose, A.; Lampert, M. A., Photoconductor Performance, Space-Charge Currents, and the Steady-State Fermi Level. *Physical Review* **1959**, *113* (5), 1227-1235.
 27. Helfrich, W.; Mark, P., Raumladungsbeschränkte Ströme in Anthrazen als Mittel zur Bestimmung der Beweglichkeit von Defektelektronen. *Zeitschrift für Physik* **1962**, *166* (4), 370-385.
 28. Podzorov, V.; Sysoev, S. E.; Loginova, E.; Pudalov, V. M.; Gershenson, M. E., Single-crystal organic field effect transistors with the hole mobility ~ 8 cm²/Vs. *Applied Physics Letters* **2003**, *83* (17), 3504-3506.
 29. Jurchescu, O. D.; Baas, J.; Palstra, T. T. M., Effect of impurities on the mobility of single crystal pentacene. *Applied Physics Letters* **2004**, *84* (16), 3061-3063.

30. Blom, P. W. M.; de Jong, M. J. M.; Vleggaar, J. J. M., Electron and hole transport in poly(p-phenylene vinylene) devices. *Applied Physics Letters* **1996**, *68* (23), 3308-3310.
31. Dacuña, J.; Salleo, A., Modeling space-charge-limited currents in organic semiconductors: Extracting trap density and mobility. *Physical Review B* **2011**, *84* (19), 195209.
32. Bozio, R.; Pecile, C., Spectroscopy of advanced materials. *Advances in Spectroscopy* **1991**, *10*, 1-3.
33. Maennig, B.; Pfeiffer, M.; Nollau, A.; Zhou, X.; Leo, K.; Simon, P., Controlled p-type doping of polycrystalline and amorphous organic layers: Self-consistent description of conductivity and field-effect mobility by a microscopic percolation model. *Physical Review B* **2001**, *64* (19), 195208.
34. Stires, I. V. J. C.; McLaurin, E. J.; Kubiak, C. P., Infrared spectroscopic determination of the degree of charge transfer in complexes of TCNE with methyl-substituted benzenes. *Chemical Communications* **2005**, (28), 3532-3534.
35. Zhu, L.; Kim, E.-G.; Yi, Y.; Brédas, J.-L., Charge Transfer in Molecular Complexes with 2,3,5,6-Tetrafluoro-7,7,8,8-tetracyanoquinodimethane (F4-TCNQ): A Density Functional Theory Study. *Chemistry of Materials* **2011**, *23* (23), 5149-5159.
36. Karpov, Y.; Erdmann, T.; Stamm, M.; Lappan, U.; Guskova, O.; Malanin, M.; Raguzin, I.; Beryozkina, T.; Bakulev, V.; Günther, F.; Gemming, S.; Seifert, G.; Hamsch, M.; Mannsfeld, S.; Voit, B.; Kiriy, A., Molecular Doping of a High Mobility Diketopyrrolopyrrole–Dithienylthieno[3,2-b]thiophene Donor–Acceptor Copolymer with F6TCNNQ. *Macromolecules* **2017**, *50* (3), 914-926.
37. Hu, P.; Wang, S.; Chaturvedi, A.; Wei, F.; Zhu, X.; Zhang, X.; Li, R.; Li, Y.; Jiang, H.; Long, Y.; Kloc, C., Impact of C–H···X (X = F, N) and π – π Interactions on Tuning the Degree of Charge Transfer in F6TNAP-Based Organic Binary Compound Single Crystals. *Crystal Growth & Design* **2018**, *18* (3), 1776-1785.
38. Zhang, J.; Geng, H.; Virk, T. S.; Zhao, Y.; Tan, J.; Di, C.-a.; Xu, W.; Singh, K.; Hu, W.; Shuai, Z.; Liu, Y.; Zhu, D., Sulfur-Bridged Annulene-TCNQ Co-Crystal: A Self-Assembled “Molecular Level Heterojunction” with Air Stable Ambipolar Charge Transport Behavior. *Advanced Materials* **2012**, *24* (19), 2603-2607.
39. Robles-Martínez, J. G.; Salmerón-Valverde, A.; Argüelles-Ramírez, J.; Zehe, A., Variation of Charge Transfer in Zn-naphtholimines with TCNQ. *Molecular Engineering* **1999**, *8* (4), 411-417.
40. Morherr, A.; Witt, S.; Chernenkaya, A.; Bäcker, J.-P.; Schönhense, G.; Bolte, M.; Krellner, C., Crystal growth of new charge-transfer salts based on π -conjugated donor molecules. *Physica B: Condensed Matter* **2016**, *496*, 98-105.
41. Mahns, B.; Kataeva, O.; Islamov, D.; Hampel, S.; Steckel, F.; Hess, C.; Knupfer, M.; Büchner, B.; Himcinschi, C.; Hahn, T.; Renger, R.; Kortus, J., Crystal Growth, Structure, and Transport Properties of the Charge-Transfer Salt Picene/2,3,5,6-Tetrafluoro-7,7,8,8-tetracyanoquinodimethane. *Crystal Growth & Design* **2014**, *14* (3), 1338-1346.
42. Hu, P.; Du, K.; Wei, F.; Jiang, H.; Kloc, C., Crystal Growth, HOMO–LUMO Engineering, and Charge Transfer Degree in Perylene-F_xTCNQ (x = 1, 2, 4) Organic Charge Transfer Binary Compounds. *Crystal Growth & Design* **2016**, *16* (5), 3019-3027.
43. Castagnetti, N.; Kociok-Köhn, G.; Da Como, E.; Girlando, A., Temperature-induced valence instability in the charge-transfer crystal TMB-TCNQ. *Physical Review B* **2017**, *95* (2), 024101.

44. Goetz, K. P.; Fonari, A.; Vermeulen, D.; Hu, P.; Jiang, H.; Diemer, P. J.; Ward, J. W.; Payne, M. E.; Day, C. S.; Kloc, C.; Coropceanu, V.; McNeil, L. E.; Jurchescu, O. D., Freezing-in orientational disorder induces crossover from thermally-activated to temperature-independent transport in organic semiconductors. *Nature Communications* **2014**, *5* (1), 5642.
45. Hu, P.; Li, H.; Li, Y.; Jiang, H.; Kloc, C., Single-crystal growth, structures, charge transfer and transport properties of anthracene-F4TCNQ and tetracene-F4TCNQ charge-transfer compounds. *CrystEngComm* **2017**, *19* (4), 618-624.
46. Hu, P.; Ma, L.; Tan, K. J.; Jiang, H.; Wei, F.; Yu, C.; Goetz, K. P.; Jurchescu, O. D.; McNeil, L. E.; Gurzadyan, G. G.; Kloc, C., Solvent-Dependent Stoichiometry in Perylene–7,7,8,8-Tetracyanoquinodimethane Charge Transfer Compound Single Crystals. *Crystal Growth & Design* **2014**, *14* (12), 6376-6382.
47. Salmerón-Valverde, A.; Robles-Martínez, J. G.; García-Serrano, J.; Gómez, R.; Ridaura, R. M.; Quintana, M.; Zehe, A., A Study of the Degree of Charge Transfer in TTF Molecular Complexes with Nitro-Carboxylated Fluorene Derivatives. *Molecular Engineering* **1999**, *8* (4), 419-426.

CHAPTER-6

Electronic, vibrational and charge-transport properties of di-C_nBTBT-F_mTCNQ co-crystals: Impact of alkyl chains and fluorination

6.1 Introduction

In the previous Chapter, we have investigated the electronic and charge-transport properties in co-crystals based on the F₆TNAP acceptor. Here, we primarily focus on charge-transfer (CT) co-crystals formed from donor moieties based on the benzothieno[3,2-b][1]benzothiophene (BTBT) molecule and acceptor moieties based on 7,7,8,8-tetracyanoquinodimethane (TCNQ) and its fluorinated derivatives.

Over the years, BTBT and its alkylated derivatives have found promising prospects as a p-type semiconducting material for organic field-effect transistor (OFET) applications. In their pristine form, di-C_n-BTBT shows a high-degree of layered crystallinity that facilitates hole transport through the material. Field-effect mobilities of up to 10 cm²V⁻¹s⁻¹ were observed,¹⁻³ which mainly arises from the herringbone packing pattern of these molecules in their pure phases. Here, it is useful to recall that rubrene also displays a similar packing pattern and exhibits mobilities in the same range (~20 cm²V⁻¹s⁻¹).⁴⁻⁶

Recently, Mèndez and coworkers, reported that the doping of 2,7-didecyl-BTBT (di-C₁₀BTBT) with fluorinated derivatives of TCNQ resulted in the formation of CT complexes.⁷ Despite the strong p-type conduction features of BTBT in its pure phase, several recent experimental reports indicate n-type or ambipolar transport characteristics upon formation of CT co-crystals of BTBT

(or its alkylated forms) with TCNQ (or its fluorinated derivatives). Two reports are especially of interest. In the first report, OFET transport characteristics measured for co-crystals formed between unsubstituted BTBT and F_m TCNQ ($m = 0, 2, 4$) identified only n-type conduction in all the combinations of co-crystals.⁸ The largest mobilities were found for the BTBT- F_4 TCNQ co-crystal, in both thin-film and single-crystal based devices. In the second report, OFET mobilities were measured for a series of CT compounds of $(di-C_n-BTBT)(F_mTCNQ)$ [$n = 4, 8, 12; m = 0, 2, 4$] and the largest mobility value among all combinations was observed for $di-C_8BTBT-F_2TCNQ$ in single-crystal based devices.⁹ Interestingly, $di-C_8BTBT-TCNQ$ shows ambipolar transport characteristics, even though its mobility is ~ 4 orders of magnitude lower than that of $di-C_8BTBT-F_2TCNQ$. However, the structure-property relationships that govern the nature of transport with sequential addition of: (1) alkyl chains to the donor moiety and/or (2) fluorine atoms to the acceptor moiety, are not yet established.

A second aspect of interest is the presence of two CT bands for $di-C_8BTBT-F_mTCNQ$ ($m=0,2,4$) co-crystals in the low-energy part of the optical absorption spectra.⁹ The CT-state energies were found to systematically shift towards lower energies with the increase in the number of fluorine atoms on the TCNQ backbone. However, the presence of additional features in the spectra along different axes challenges the CT peak assignments. Hence, it is important to identify the molecular-scale factors that define the nature of the excited states in these systems and to correlate them to experimental predictions.

To obtain a better perspective, we choose to investigate the electronic-structure, vibrational, and charge-transport properties of $BTBT-F_mTCNQ$ ($m=0,2,4$) and $di-C_nBTBT-F_mTCNQ$ ($n=8,12;$

m=0,4) co-crystals (see **Figure 6.1**). Our work here mostly focuses on deriving the structure-property relationships and identifying the trends in the electronic properties upon: (1) increasing the length of the alkyl chains on the D moiety and (2) increasing the number of fluorine atoms on the A moiety, in the co-crystals considered. Also, we quantify the ground-state degree of CT in these systems in order to rationalize the impact of the aspects mentioned above.

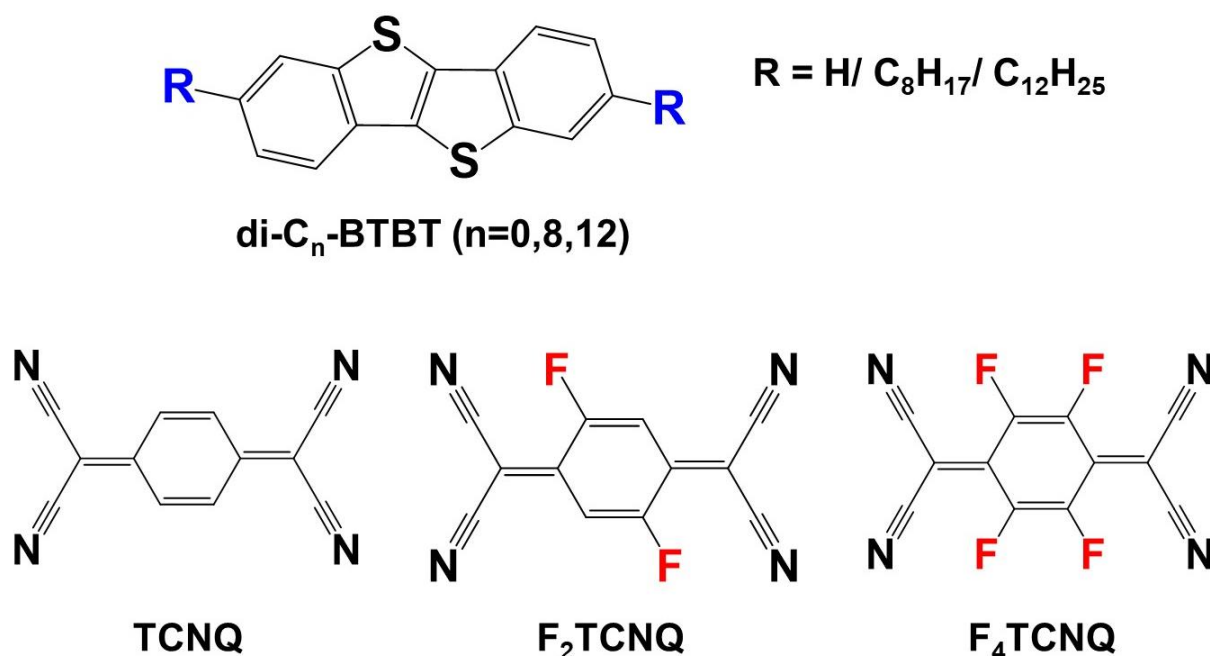


Figure 6.1. Chemical structures of the BTBT (n=0, R=H), di-C₈BTBT (n=8, R=C₈H₁₇), and di-C₁₂BTBT (n=12, R=C₁₂H₂₅) donors as well as the TCNQ, F₂TCNQ, and F₄TCNQ acceptor molecules.

6.2. Methodology

Geometry optimizations and calculations of individual molecular energies of BTBT, di-C_n-BTBT (n=8,12) and F_mTCNQ (m=0, 2, 4) were performed using density functional theory (DFT) at the B3LYP/6-31G (d, p) level. Time-dependent density functional theory (TDDFT) was used at the same level on the optimized ground-state geometries to calculate the electronic excitations from the ground state. A natural transition orbital (NTO) approach was applied to visualize the

electronic excitations.¹⁰ All of these calculations were performed using the Gaussian 09. D01 package.¹¹

The geometry optimizations of the CT co-crystals were also performed at the B3LYP/6-31G (d, p) level. During optimization, the cell parameters were kept fixed at their experimental values while the atomic positions were allowed to relax. Harmonic vibrational frequencies were calculated at the Γ point of the crystals. A Coupled Perturbed Hartree-Fock/ Kohn-Sham (CPHF/CPKS) approach,¹² which performs a completely analytical determination of IR and RAMAN intensities, was used for calculating the vibrational spectra. These DFT calculations with periodic boundary conditions were carried out with the CRYSTAL 17 package.¹³

The electronic band-structures and density of states (DOS) for all the crystals were calculated at B3LYP/6-31G (d, p) level. In order to compare our results with previous studies, the electronic-structure calculations of the co-crystals were also performed using the experimental crystal structures.¹⁴ Uniform $8\times 8\times 8$ or $8\times 8\times 4$ Monkhorst-Pack k-point meshes were employed for the BTBT- F_m TCNQ ($m=0,2,4$) and di- C_n BTBT- F_m TCNQ ($n=8,12$ and $m=0,4$) co-crystals. All band-structure calculations were performed using the CRYSTAL 14 package.¹⁵

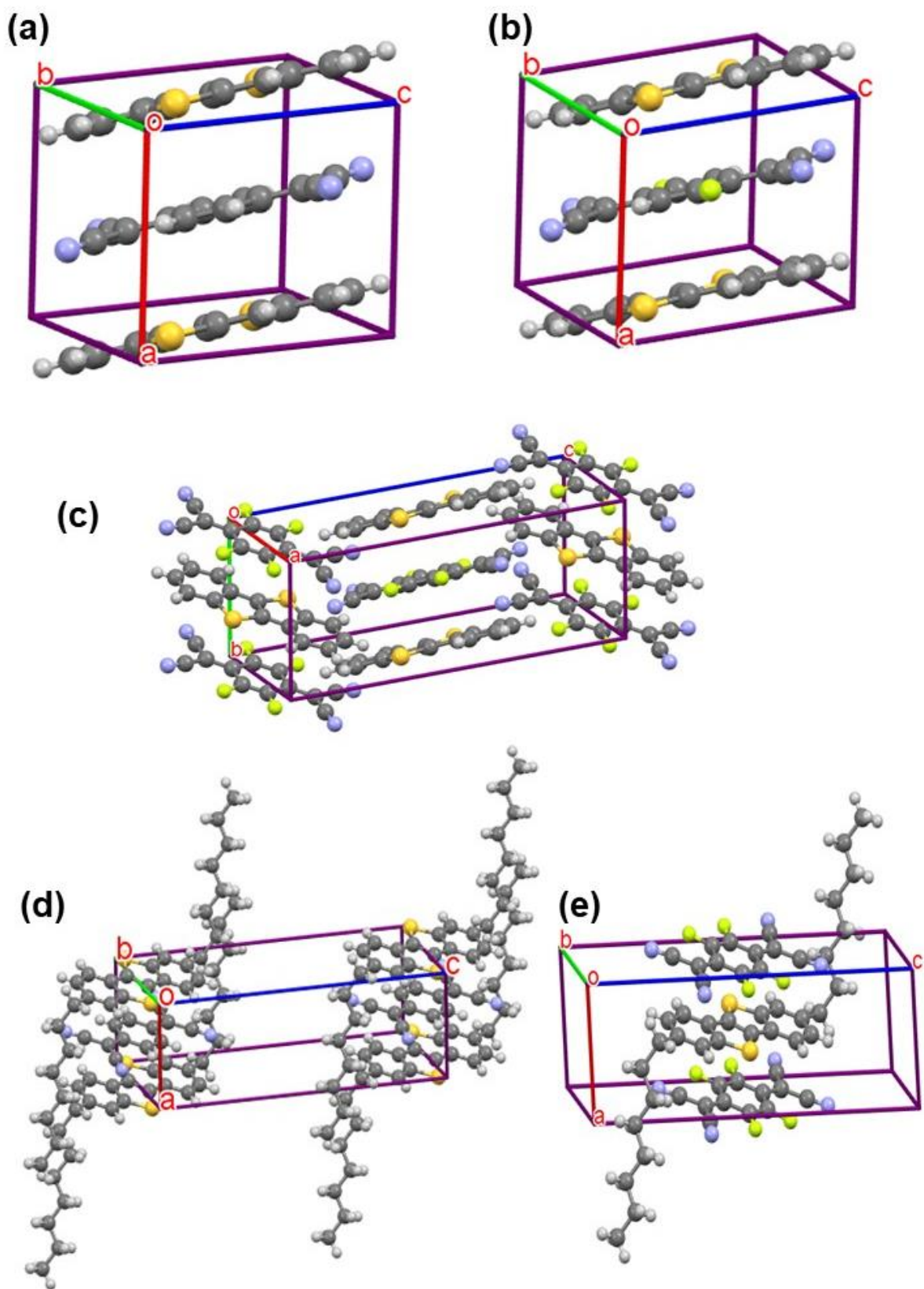
The charge-transport properties of the co-crystals were characterized based on electronic-coupling (transfer-integrals) and effective-mass calculations for both holes and electrons. We have applied the same protocols for all these calculations as in Chapter 5.¹⁶⁻¹⁸ In addition to through-space electronic couplings along the stacking direction, the transfer integrals between donor-donor, donor-acceptor, and acceptor-acceptor components located in different stacks were evaluated

using the fragment orbital approach. Also, superexchange couplings were estimated for both holes and electrons using a modified version of the Koopmans theorem, similar to the description in Chapter 5.¹⁹ All these calculations were carried out at the B3LYP/6-31G (d, p) level with the Gaussian 09.D01 package.¹¹

6.3. Results and Discussions

6.3.1. Electronic Structure and Electronic Couplings

The crystal structures of BTBT-F_mTCNQ and di-C_nBTBT-F_mTCNQ were taken from the Cambridge Structural Database (CCDC), deposits 1031368, 1031369, 1031371, 1031372, 1583470, 1583471 and 1583473.^{8, 9} BTBT-TCNQ, BTBT-F₂TCNQ and di-C_nBTBT-F_mTCNQ (n=8,12; m=0,4) co-crystals belong to the triclinic space group P $\bar{1}$, while the BTBT-F₄TCNQ co-crystal belongs to the monoclinic P2₁/c space group. All co-crystals are characterized by a 1:1 stoichiometry and crystallize in a mixed stack array. The BTBT-TCNQ, BTBT-F₂TCNQ, and di-C_nBTBT-F_mTCNQ co-crystals are stacked along the a-direction while BTBT-F₄TCNQ is stacked along the b-direction (see **Figure 6.2**). In all cases, the donor and acceptor molecules are equidistant from each other along the stacking direction; therefore, similar electronic couplings can be expected between donor-acceptor pairs along the stacking direction in all these co-crystals.



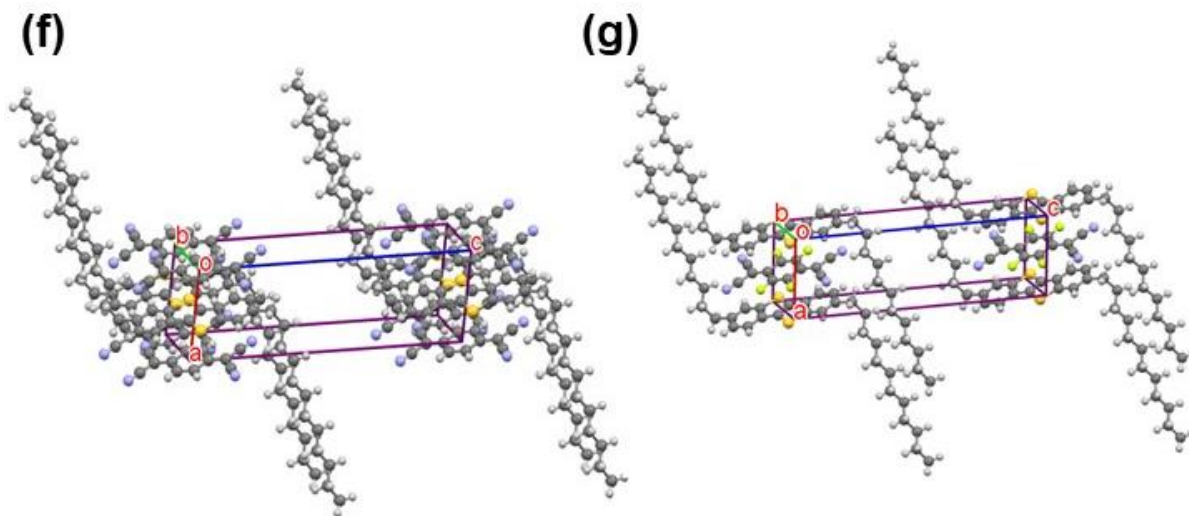


Figure 6.2. Crystal structures of (a) BTBT-TCNQ, (b) BTBT-F₂TCNQ, (c) BTBT-F₄TCNQ, (d) di-C₈BTBT-TCNQ, (e) di-C₈BTBT-F₄TCNQ, (f) di-C₁₂BTBT-TCNQ, and (g) di-C₁₂BTBT-F₄TCNQ. The stacking directions are represented in red for (a, b, d, e, f, and g) cases and in green for the (c) case.

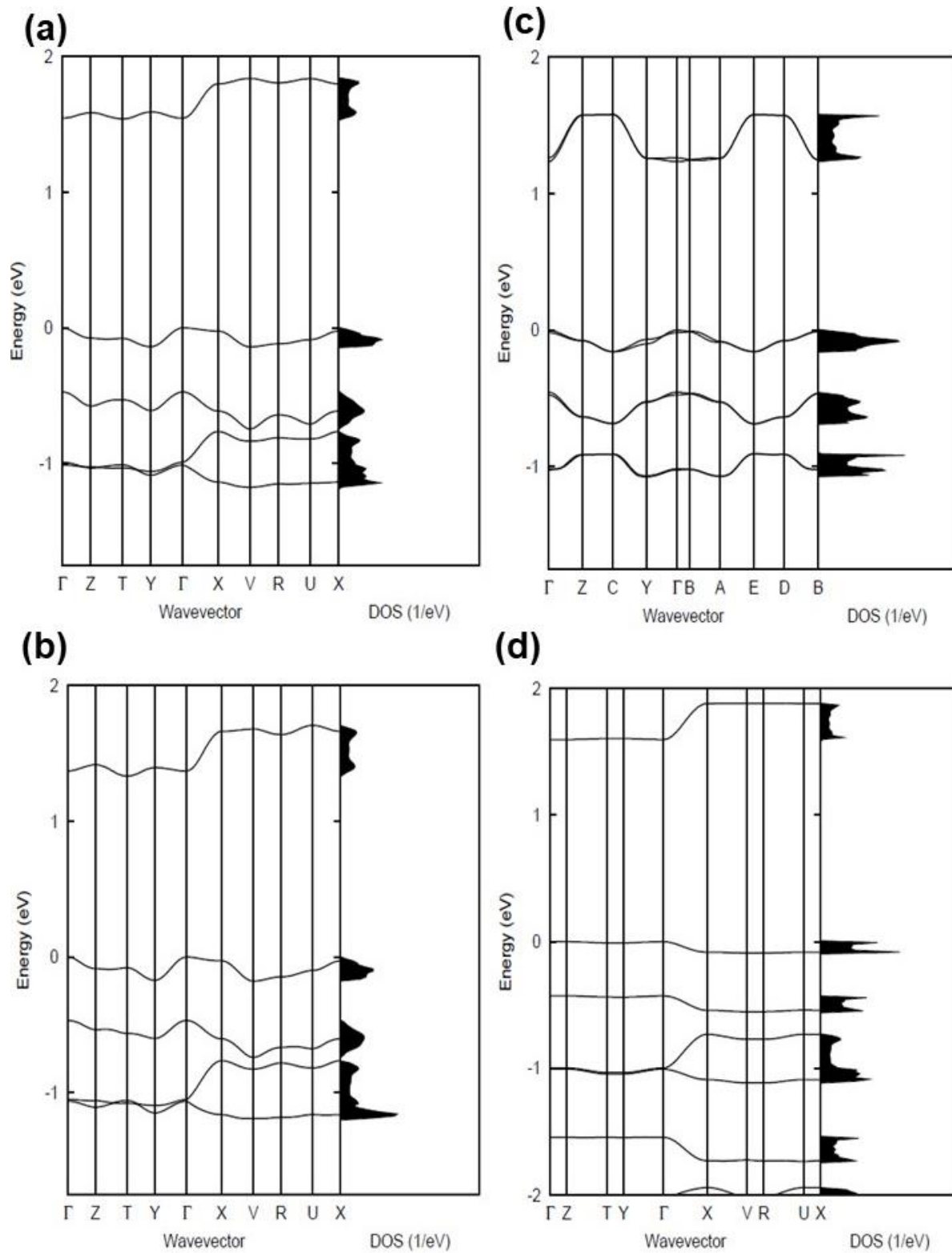
The band structures and the densities of states of the co-crystals are given in **Figure 6.3**. **Table 6.1** collects the widths of conduction bands (CB) and valence bands (VB), along with the effective masses for each co-crystal (**Table 6.2** and **Table 6.3** provide more details on the effective masses and transfer integrals, respectively). The CB bandwidths are found to be relatively large, in the range of 280-380 meV, comparable to those already reported for the co-crystals based on TCNQ and F₄TCNQ acceptors.^{14,20} The main contribution to the total CB width comes from the electronic interactions between acceptor molecules along the stacking direction. The largest values among the CB widths are estimated for the BTBT:F₂TCNQ, BTBT:F₄TCNQ, di-C₈BTBT-F₄TCNQ and di-C₁₂BTBT:F₄TCNQ co-crystals; this results from the large effective (superexchange) transfer integral (~60-70 meV) along their respective stacking directions (see **Table 6.3**).

The VB width of all co-crystals are narrower, in the range of 80-180 meV. The BTBT-F_mTCNQ (m=0,2,4) co-crystals have a relatively larger and dispersive VB width along multiple directions,

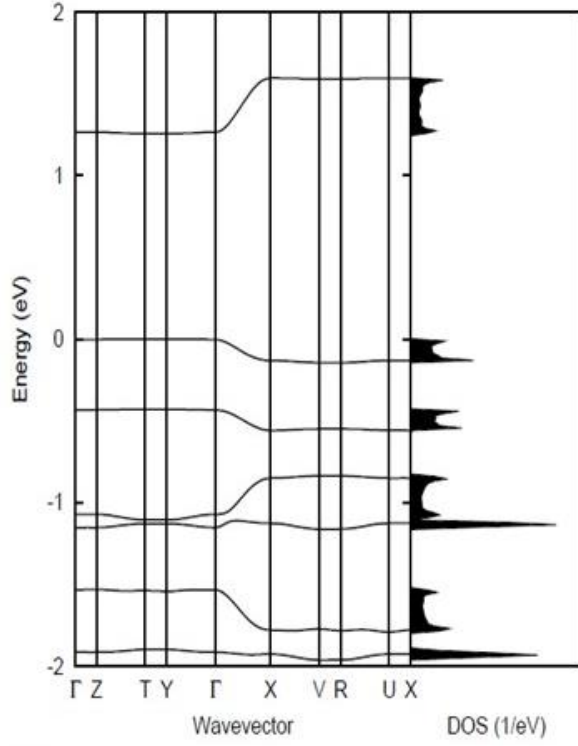
in comparison to the co-crystals based on the di-C_nBTBT donors; the di-C_nBTBT-F_mTCNQ (n=8,12; m=0,4) co-crystals show VB dispersion only along the stacking direction. In all co-crystals, the superexchange couplings for the holes are much smaller than those for the electrons. However, direct through-space transfer integrals between BTBT molecules in different stacks are found to be either larger (>10 meV) or nearly similar to the superexchange couplings (holes) in the BTBT-F_mTCNQ co-crystals; consequently, the dispersive nature of their VB in the band structure.

Table 6.1. B3LYP/6-31G (d, p) conduction and valence bandwidths (in meV) along with the lowest two effective masses (in units of electron mass in vacuum, m_0).

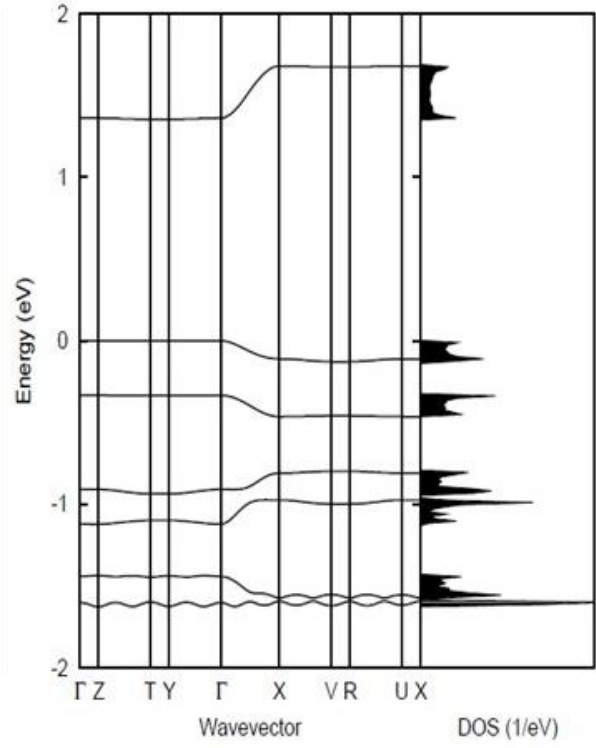
Co-crystals	Conduction Bandwidth	Valence Bandwidth	Effective Mass Electrons		Effective Mass Holes	
			m_1/m_0	m_2/m_0	m_1/m_0	m_2/m_0
			BTBT-TCNQ	299	139	1.0
BTBT-F ₂ TCNQ	372	177	0.8	1.5	1.0	3.4
BTBT-F ₄ TCNQ	345	157	0.8	3.6	2.1	2.3
di-C ₈ BTBT-TCNQ	286	89	1.0	>10	3.1	>10
di-C ₈ BTBT-F ₄ TCNQ	340	132	0.7	>10	1.5	>10
di-C ₁₂ BTBT-TCNQ	283	100	1.2	7.5	3.9	>10
di-C ₁₂ BTBT-F ₄ TCNQ	324	128	1.1	6.0	3.6	>10



(e)



(g)



(f)

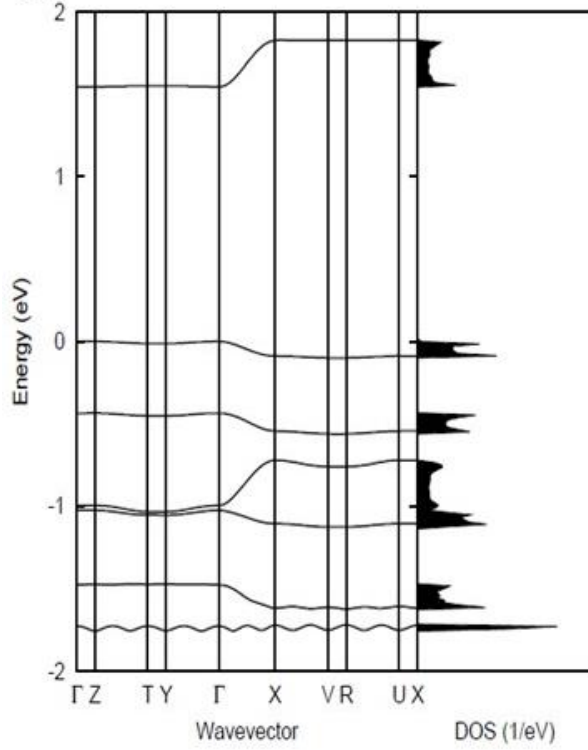


Figure 6.3. Electronic band structures and densities of states of the: (a) BTBT:TCNQ, (b) BTBT:F₂TCNQ, (c) BTBT:F₄TCNQ, (d) di-C₈BTBT:TCNQ, (e) di-C₈BTBT:F₄TCNQ, (f) di-C₁₂BTBT:TCNQ, and (g) di-C₁₂BTBT:F₄TCNQ crystals. The high-symmetry points in the first Brillouin zone are labelled as: $\Gamma = (0,0,0)$, $Z = (0,0,0.5)$, $T = (0,0.5,0.5)$, $Y = (0,0.5,0)$, $X = (0.5,0,0)$, $V = (0.5,0.5,0)$, $R = (0.5,0.5,0.5)$ and $U = (0.5,0,0.5)$, for the (a, b, d, e, f & g) cases, and $\Gamma = (0,0,0)$, $Z = (0,0.5,0)$, $C = (0.5,0.5,0)$, $Y = (0.5,0,0)$, $B = (0,0,0.5)$, $A = (-0.5,0,0.5)$, $E = (-0.5,0.5,0.5)$ and $D = (0,0.5,0.5)$ for the (c) case. All points are given in fractional coordinates in the reciprocal space. The zero of energy is taken as the top of the valence band.

Consistent with the band structure and electronic-coupling results, the smallest effective masses for electrons are found along the stacking directions in all co-crystals. Very small effective-mass values of $0.8m_0$, $0.8m_0$, and $0.7 m_0$ are calculated for electrons in BTBT-F₂TCNQ, BTBT-F₄TCNQ, and di-C₈BTBT-F₄TCNQ, respectively (where m_0 is the rest mass of electrons in vacuum). The smallest effective mass values for electrons in other co-crystals are in the range of 1-1.2 m_0 . The smallest effective-mass components for holes are larger, although, in the BTBT-TCNQ and BTBT-F₂TCNQ cases, they are comparable to some of the smallest components of electron-effective masses. In a pattern that is similar to the F₆TNAP-based co-crystals, the smallest effective masses for holes in the BTBT-F_mTCNQ ($m=0,2,4$) co-crystals are oriented along a direction perpendicular to the stacking axis (see **Tables 6.2 & 6.3**), due to the electronic coupling between the donor molecules located in different stacks. This is in contrast to the cases of the di-C_nBTBT-F_mTCNQ ($n=8,12$; $m=0,4$) co-crystals in which the effective-mass components for holes are oriented only along the stacking direction. Interestingly, a rather small effective-mass component for holes ($2.3 m_0$) is also found along the stacking direction in BTBT-F₄TCNQ, indicating a 2D nature of hole transport in this system. The BTBT-F₂TCNQ co-crystal also exhibits a 2D character of charge transport in this case for electrons; a small component of electron-effective mass ($1.5 m_0$) is found oriented indeed along a direction perpendicular to the stacking axis.

Table 6.2. Hole and electron effective masses, m (in units of the free electron mass at rest, m_0).

Crystal		m / m_0	Parallel to
BTBT-TCNQ	Holes at Γ (0, 0, 0)	1.3	b-0.09a-0.71c
		4.7	c+0.45a+0.87b
		10.7	a-0.11b-0.19c
	Electrons at T (0, 0.5, 0.5)	1.07	a-0.03b+0.01c
		3.2	c-0.03a-0.79b
		13.4	b-0.02a+0.55c
BTBT-F ₂ TCNQ	Holes at Γ (0, 0, 0)	1.03	b-0.13a-0.77c
		3.41	b+0.45a+0.96c
		4.91	a-0.09b-0.19c
	Electrons at T (0, 0.5, 0.5)	0.8	a-0.07b+0.05c
		1.5	b+0.1a-0.7c
		4.3	c-0.04a+0.8c
BTBT-F ₄ TCNQ	Holes at Γ (0, 0, 0)	2.1	a+0.17c
		2.3	b
		5.2	c-0.65a
	Electrons at Γ (0, 0, 0)	0.83	b
		3.62	a+0.31c
		5.73	a-0.61c
di-C ₈ BTBT-TCNQ	Holes at Γ (0, 0, 0)	3.06	a+0.011b-0.002c
		33.76	b-0.27a-0.09c
		358.06	c-0.56a+0.51b
	Electrons at Γ (0, 0, 0)	1.0	a-0.007b
		26.9	b-0.29a
		240.0	c-0.4a-0.03b
di-C ₈ BTBT-F ₄ TCNQ	Holes at Y (0, 0.5, 0)	1.5	a-0.04b+0.00098c
		61.66	c-0.6b+0.7c
		308.26	b-0.23b-0.16c
	Electrons at T (0, 0.5, 0.5)	0.73	a+0.02b+0.003c
		15.80	b-0.4a+0.09c
		327.9	c-0.14a-0.56c
di-C ₁₂ BTBT-TCNQ	Holes at Γ (0, 0, 0)	3.9	a-0.07b-0.04c
		13.7	b+0.03a+0.82c
		18.9	b-0.26a-0.18c
	Electrons at Γ (0, 0, 0)	1.25	a-0.09b-0.03c
		7.54	b-0.001a+0.71c
		14.91	b-0.24a-0.20c
di-C ₁₂ BTBT-F ₄ TCNQ	Holes at Y (0, 0.5, 0)	3.56	a-0.17b-0.03c
		21.06	b+0.017a+0.63c
		30.92	b-0.15a-0.24c
	Electrons at (0, 0.5, 0.010)	1.11	a-0.009b-0.043c
		6.0	b-0.03a+0.7c
		11.54	b-0.27a-0.22c

Experimentally, Mori and co-workers have reported n-type conduction in single-crystal OFET devices of the BTBT-F_mTCNQ (m=0, 2, 4) systems; with the largest mobilities observed for the BTBT-F₄TCNQ co-crystal.⁸ Hasegawa and co-workers have also reported n-type transport in devices based on diC₈BTBT-F_mTCNQ (m=0,2,4) co-crystals.⁹ Our DFT calculations are consistent with the available experimental results as good electron-transport properties are predicted for the seven co-crystals. However, our calculations also predict good hole-transport properties for the BTBT-F_mTCNQ (m=0,2,4) and di-C₈BTBT-F₄TCNQ cases, which suggests that ambipolar charge transport could be displayed in these systems. Experimentally, ambipolar transport has been observed only for the di-C₈BTBT-TCNQ co-crystal, for which our DFT calculations predict only electron-transport characteristics.

Table 6.3. B3LYP/6-31G (d,p) estimates of t_{AA} , t_{DD} , and t_{DA} , and super-exchange couplings for holes (t_h^{eff}) and electrons (t_e^{eff}).

Co-crystals	t_{A-A}	t_{D-D}	t_{D-A}	$t_{electrons}^{eff}$	t_{holes}^{eff}
BTBT-TCNQ	1.9	14.2	160.3	56.3	3.6
BTBT-F ₂ TCNQ	7.2	17.6	226.7	63.2	5.3
BTBT-F ₄ TCNQ	2.7	13.9	252.4	66.5	16.5
di-C ₈ BTBT-TCNQ	0.7	7.9	213.8	57.9	5.4
di-C ₈ BTBT-F ₄ TCNQ	3.3	5.7	276.4	62.8	13.6
di-C ₁₂ BTBT-TCNQ	0.6	10.6	184.6	57.0	6.6
di-C ₁₂ BTBT-F ₄ TCNQ	2.7	5.1	174.3	60.9	10.3

6.3.2. Superexchange Couplings: Electron hole Asymmetry

A characteristic feature of many co-crystals is the “mirror symmetry” between VBs and CBs in their band structures. Representative examples for DMQtT-F₄TCNQ and DBTTF-TCNQ are shown in **Figure 6.4**. However, in the co-crystals considered in the present Chapter and the previous Chapter, this mirror symmetry between VB and CB is absent.

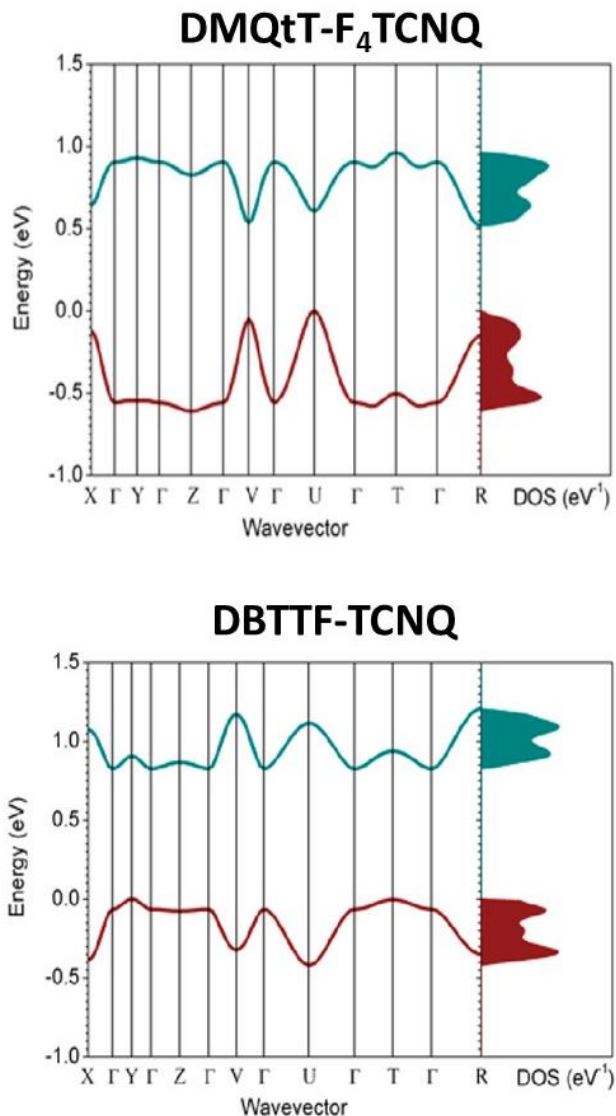


Figure 6.4. Electronic band structures and densities of states of the: (a) DMQtT:F₄TCNQ and (b) DBTTF:F₄TCNQ co-crystals. The points of high symmetry in the first Brillouin zone are labelled as follows: $\Gamma = (0,0,0)$, $Z = (0,0,0.5)$, $T = (0,0.5,0.5)$, $Y = (0,0.5,0)$, $X = (0.5,0,0)$, $V = (0.5,0.5,0)$, $R = (0.5,0.5,0.5)$ and $U = (0.5,0,0.5)$. All points are given in fractional coordinates of the reciprocal space. The zero of energy is taken as the top of valence band. Adapted from Reference [17].

In order to explain why the electron-hole symmetry is observed in some co-crystals but is absent in others, we have considered the case where superexchange couplings can be treated by means of perturbation theory. The super-exchange couplings for holes and electrons in this limit are given as:

$$t_h^{eff} = \sum_{a_D(b_A)} \frac{t_{a_{D1}b_A} t_{b_A a_{D2}}}{E_{a_D b_A}} \quad (1)$$

$$t_e^{eff} = \sum_{b_A(a_D)} \frac{t_{b_{A1}a_D} t_{a_D b_{A2}}}{E_{a_D b_A}} \quad (2)$$

Here, a_D and b_A represent the molecular orbitals of the donor and acceptor (with $D_1[A_1]$ and $D_2[A_2]$ corresponding to two donor[acceptor] molecules in the D_1 -A- D_2 [A_1 -D- A_2] triad); $E_{a_D b_A}$ and $t_{a_D b_A}$ are the energy gaps and transfer integrals involving these orbitals. When only the transfer integral from the HOMO (H_D) of the donor to the LUMO (L_A) of the acceptor contributes to the superexchange couplings, we obtain:

$$t_e^{eff} = t_h^{eff} = \frac{t_{H_D L_A}^2}{E_{H_D L_A}} \quad (3)$$

Thus, in this case, the effective coupling for holes and electrons are equal. Generally, this occurs when the highest occupied molecular orbital (HOMO) and lowest unoccupied molecular orbital (LUMO) levels are energetically well separated from the rest of the molecular orbital levels. However, this is not the case in the current set of co-crystals. As seen from **Table 6.4**, the electronic couplings of the HOMO-1 energy level of BTBT and LUMOs on the acceptors are at least 50% larger than the couplings between $HOMO_D$ and $LUMO_A$. Since the HOMO-1 and HOMO levels of BTBT are separated by only 0.3 eV (see **Figure 6.5**), these two electronic coupling pathways ($HOMO_D \Rightarrow LUMO_A$ and $HOMO-1_D \Rightarrow LUMO_A$) contribute nearly equally to the superexchange couplings for electrons, resulting in relatively larger t_e^{eff} values and a large dispersion of the CBs.

Several electronic-coupling pathways also contribute to the super-exchange couplings for holes. Our calculations on the BTBT-TCNQ co-crystal show that, despite the fact that the LUMO+1 in TCNQ, F₂TCNQ, and F₄TCNQ is separated from their respective LUMO by about 2 eV, the HOMO_D => LUMO+1_A channel also contributes considerably to the superexchange coupling. We note that, in general, two DA transfer integrals in the same triad (for instance, $t_{a_{D_1}b_A}$ and $t_{b_A a_{D_2}}$ in D₁-A-D₂) could have similar or opposite signs. In the case of BTBT-TCNQ, the main contributions for the hole-transport have an opposite sign and cancel each other, leading to very low superexchange couplings for the holes. Therefore, the VB along the stacking directions shows a much lower dispersion in comparison with the CB, resulting in high asymmetry between holes and electrons.

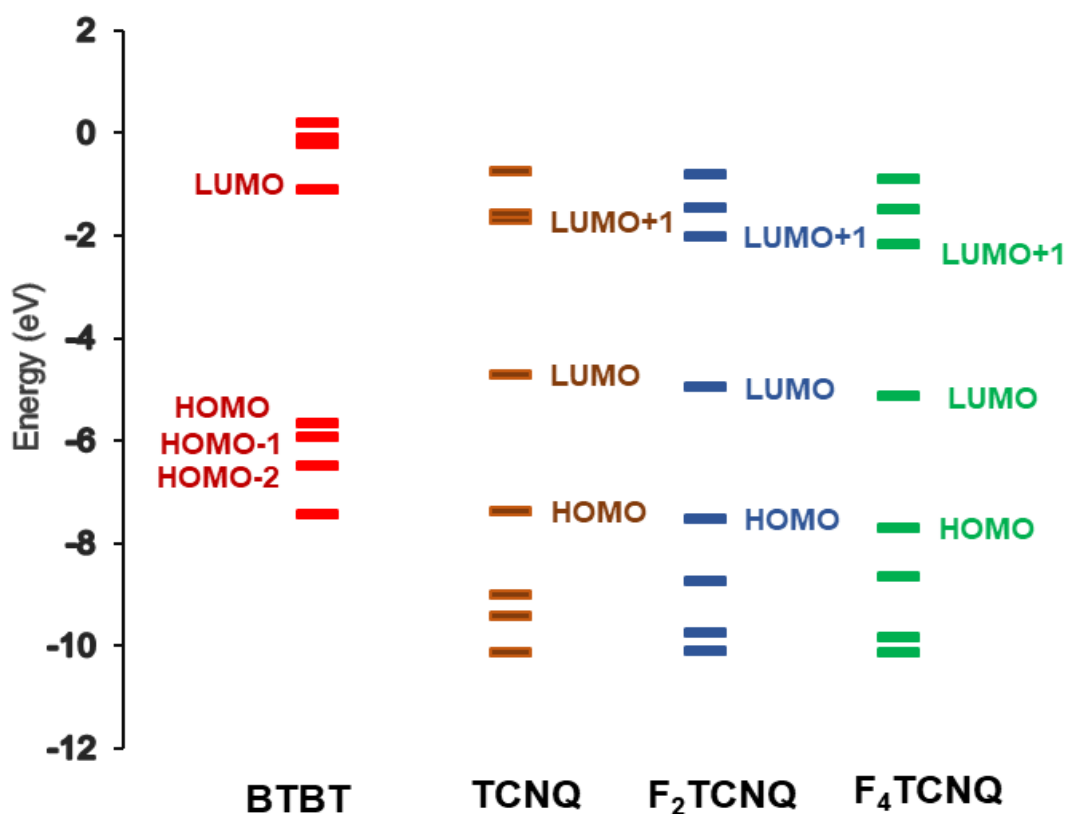


Figure 6.5. Energy levels of BTBT, TCNQ, F₂TCNQ, and F₄TCNQ calculated at the B3LYP/6-31G(d, p) level.

Table 6.4. B3LYP/6-31G (d,p) estimates of $t_{(H)D-(L)A}$ (meV) and $t_{(H-1)D-LA}$ [(H)_D=HOMO of the donor molecule and L_A is the LUMO of the acceptor molecule].

co-crystals	t_{HD-LA} (meV)	$t_{(H-1)D-LA}$ (meV)
BTBT-TCNQ	160.3	348.1
BTBT-F ₂ TCNQ	226.7	329.5
BTBT-F ₄ TCNQ	252.4	331.9
di-C ₈ BTBT-TCNQ	213.8	424.4
di-C ₈ BTBT-F ₄ TCNQ	276.4	394.5
di-C ₁₂ BTBT-TCNQ	184.6	430.3
di-C ₁₂ BTBT-F ₄ TCNQ	174.3	239.7

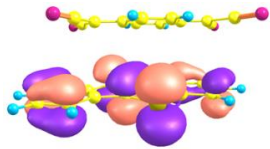
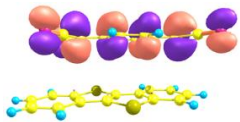
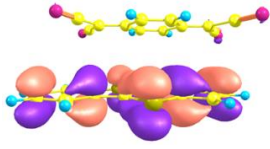
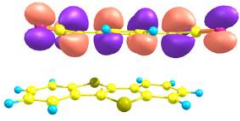
6.3.3. Low-energy CT Optical Transitions

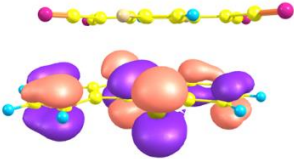
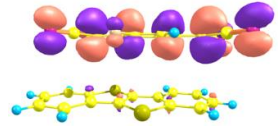
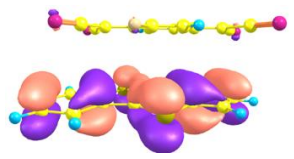
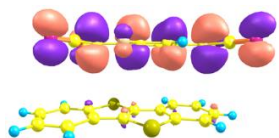
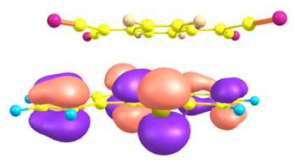
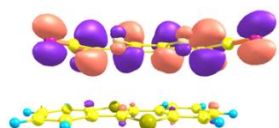
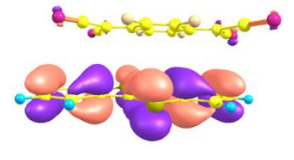
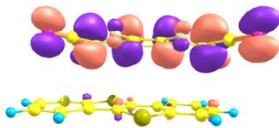
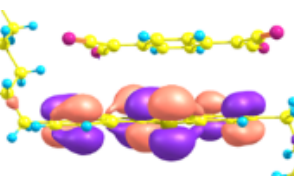
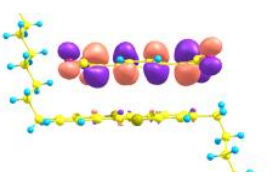
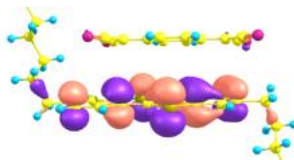
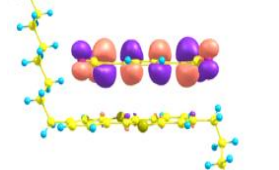
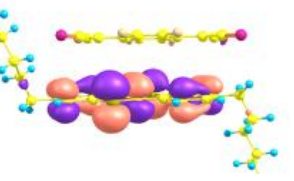
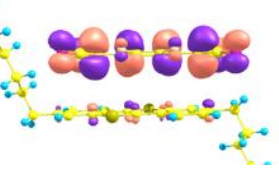
In order to investigate the nature of the lowest energy optical transitions, we performed TDDFT calculations. NTO analyses reveal that the S_0-S_1 , S_0-S_2 , and S_0-S_3 transitions are CT states (see **Table 6.5** and **Figure 6.6**). For all co-crystals, the coefficients corresponding to each transition indicate dominant contributions from $HOMO_D \Rightarrow LUMO_A$ and $HOMO-1_D \Rightarrow LUMO_A$ one-electron excitations for the S_1 and S_2 excited states, respectively. We note that Hasegawa and co-workers have also observed two peaks in the optical absorption spectra of the diC₈BTBT-F_mTCNQ (m=0, 2, 4) co-crystals and assigned the transitions to $HOMO_D \Rightarrow LUMO_A$ and $(HOMO-1)_D \Rightarrow LUMO_A$ excitations.⁹ Interestingly, a ~0.5-0.6 eV difference was observed between the two CT transitions for the diC₈BTBT-F_mTCNQ (m=0, 2, 4) co-crystals; this trend is consistent with the results of our calculations as well. Thus, the two CT bands observed experimentally and those

reproduced by our TDDFT calculations are related to the same DA coupling pathways ($\text{HOMO}_D \Rightarrow \text{LUMO}_A$ and $\text{HOMO-1}_D \Rightarrow \text{LUMO}_A$) that define the super-exchange couplings for holes, showing that in DA co-crystals there is a strong relationship between optical and charge-transport properties.

Table 6.5. Singlet excited-state energies of co-crystals calculated by TDDFT at the B3LYP/6-31G(d,p) level. The values in brackets are the oscillator strengths (f).

Co-crystals	S1 (f)	S2 (f)	S3 (f)
BTBT-TCNQ	1.19 (0.0061)	1.78 (0.0620)	2.16 (0.0098)
BTBT-F2TCNQ	1.10 (0.0106)	1.65 (0.0616)	2.05 (0.0168)
BTBT-F4TCNQ	1.06 (0.0107)	1.61 (0.0666)	2.00 (0.0131)
di-C8BTBT-TCNQ	1.16 (0.0164)	1.63 (0.0570)	2.12 (0.0092)
di-C8BTBT-F4TCNQ	1.01 (0.0198)	1.43 (0.0634)	1.95 (0.0105)
di-C12BTBT-TCNQ	1.13 (0.0171)	1.59 (0.0555)	2.10 (0.0088)
di-C12BTBT-F4TCNQ	1.05 (0.0143)	1.42 (0.0641)	1.87 (0.0118)

Co-crystal	Excited State	Hole	Electron
BTBT-TCNQ	S1		
	S2		

BTBT-F ₂ TCNQ	S1		
	S2		
BTBT-F ₄ TCNQ	S1		
	S2		
di-C ₈ BTBT-TCNQ	S1		
	S2		
di-C ₈ BTBT-F ₄ TCNQ	S1		

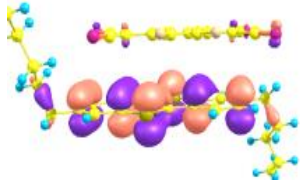
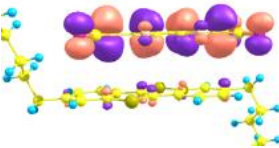
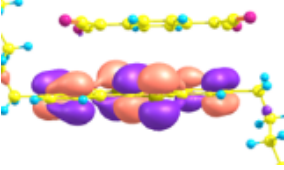
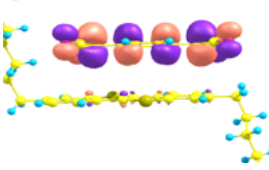
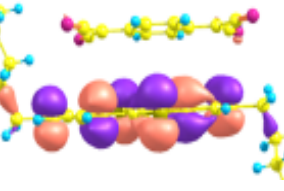
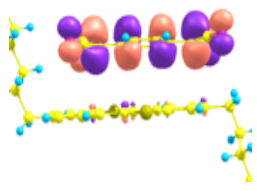
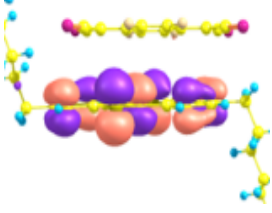
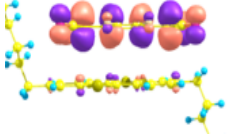
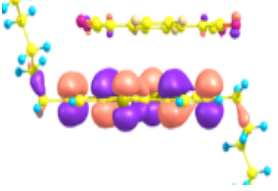
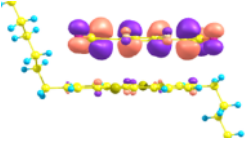
	S2		
di-C ₁₂ BTBT-TCNQ	S1		
	S2		
di-C ₁₂ BTBT-F ₄ TCNQ	S1		
	S2		

Figure 6.6. Natural Transition Orbitals for the lowest excited states calculated at the TDDFT B3LYP/6-31G (d, p) level.

6.3.4. Degree of Charge Transfer

It is also of interest to quantify the degree of charge transfer (ρ) in the co-crystals. As already mentioned in Chapter 5, vibrational spectroscopy is a common tool used to quantify ρ . We recall that the changes in vibrational frequencies when going from a single-component crystal to D-A co-crystals cannot be necessarily linked to ρ ; this is even more evident in the current systems, for which we have calculated the IR absorption spectra. Here, we focus on both C=C and the C \equiv N stretching frequencies for comparison. We note that the C=C stretching frequencies in the TCNQ, F₂TCNQ, and F₄TCNQ acceptors are found in the range of 1400-1600 cm⁻¹; however, there are several peaks of differing intensities that appear in this region. In contrast, the C \equiv N bonds exhibit only two peaks in all co-crystals. An interesting feature that emerges from the C \equiv N vibrations (see **Figure 6.7b**) is that the peaks are decreasing in intensity with an increase in the length of alkyl chains on the donor and/or increase in the number of fluorine atoms on the acceptor unit.

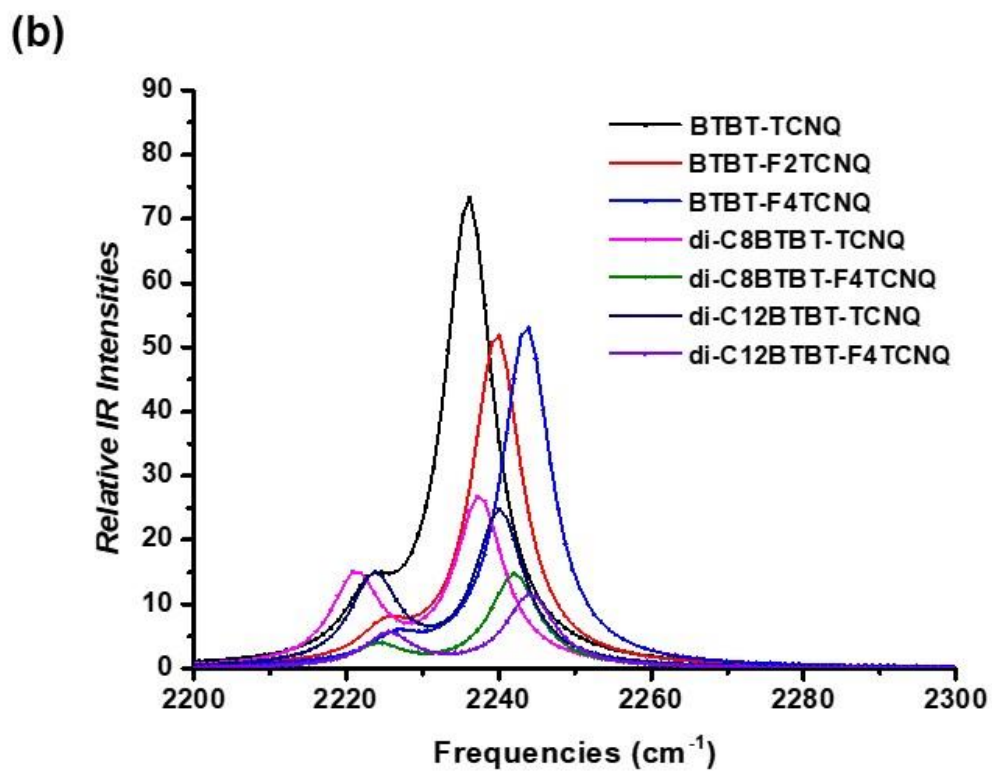
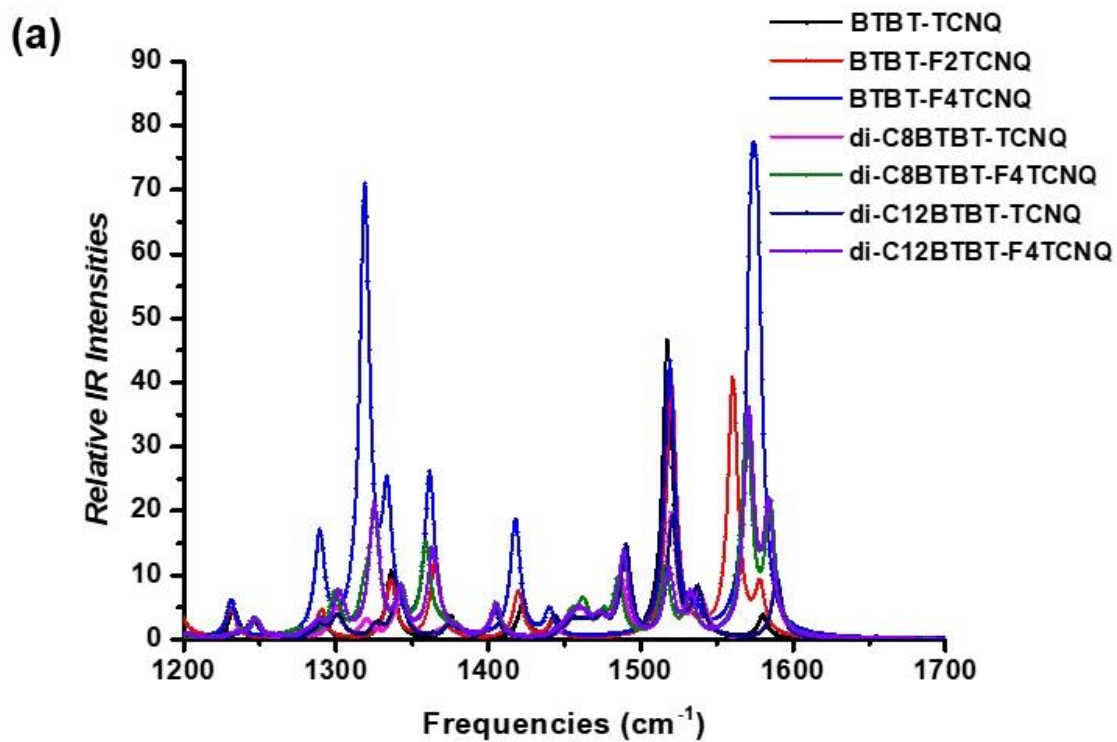


Figure 6.7. B3LYP/6-31G (d, p) IR vibrational frequencies (scaled by 0.9614) comparing: (a) the charge sensitive bands in the 1200-1700 cm^{-1} region, and, (b) the $\text{C}\equiv\text{N}$ stretching modes of F_mTCNQ ($m=0, 2, 4$) in the charge-transfer complexes.

While the presence of two sharp $\text{C}\equiv\text{N}$ peaks in the IR spectra of all co-crystals is an argument for their use in the estimation of ρ , the system-dependent nature of this method questions its general applicability. Moreover, previous works have highlighted the often overestimated nature of the degree of CT obtained from $\text{C}\equiv\text{N}$ stretching frequencies.^{21, 22} Therefore, we choose not to rely on this method for estimation of ρ here. Instead, similar to the case of the F_6TNAP co-crystals, we have applied an approach based on Mulliken charges (see **Table 6.6**). An interesting trend that emerges from the results is that the co-crystals with unsubstituted BTBT as the donor exhibit nearly similar ρ values; this trend has been previously reported by Rovira and co-workers on the same systems using IR absorption spectra.²² The co-crystals with alkyl-chain substituted BTBT, on the other hand, display overall higher ρ values. The largest ρ value is calculated for the $\text{diC}_8\text{BTBT-F}_4\text{TCNQ}$ system, which also shows one of the largest transfer integrals and conduction bandwidth along the stacking direction as well as one of the smallest effective masses for electrons. Moreover, $\text{diC}_8\text{BTBT-F}_4\text{TCNQ}$ shows the largest OFET mobility values among the co-crystals in single-crystal based devices.⁹

Table 6.6. Degree of charge transfer in the co-crystals based on Mulliken charges.

co-crystals	ρ (calculated)
BTBT-TCNQ	0.036
BTBT-F2TCNQ	0.044
BTBT-F4TCNQ	0.040
di-C8BTBT-TCNQ	0.066
di-C8BTBT-F4TCNQ	0.072
di-C12BTBT-TCNQ	0.056
di-C12BTBT-F4TCNQ	0.052

6.4. Conclusion

We have investigated the electronic structure, vibrational properties and charge-transport properties of co-crystals based on BTBT and di-C_nBTBT (n=8, 12) donors and F_mTCNQ (m=0, 2, 4) acceptors. The DFT calculations predict large conduction bandwidths and small effective masses for electrons in all co-crystals, which suggests good electron-transport properties in all these systems. Large values of the valence bandwidths and small effective masses for holes are also observed for the BTBT-F_mTCNQ (m=0, 2, 4) co-crystals, which also suggests ambipolar CT characteristics in these systems.

We also explored the electron-hole asymmetry observed in the band structures and characterized the formation of asymmetric charge-transport pathways leading to different extent of superexchange couplings for holes and electrons. The calculated lowest energy CT excitations were found to correlate well with the experimental anisotropic optical absorption spectra. Finally,

we evaluated the degree of charge transfer, which was quantified using Mulliken charges. The results are consistent with those for the electronic coupling and band structures.

6.5. References

1. Ebata, H.; Izawa, T.; Miyazaki, E.; Takimiya, K.; Ikeda, M.; Kuwabara, H.; Yui, T., Highly Soluble [1]Benzo[thieno[3,2-b]benzothiophene (BTBT) Derivatives for High-Performance, Solution-Processed Organic Field-Effect Transistors. *Journal of the American Chemical Society* **2007**, *129* (51), 15732-15733.
2. Minemawari, H.; Yamada, T.; Matsui, H.; Tsutsumi, J. y.; Haas, S.; Chiba, R.; Kumai, R.; Hasegawa, T., Inkjet printing of single-crystal films. *Nature* **2011**, *475* (7356), 364-367.
3. Nakayama, K.; Hirose, Y.; Soeda, J.; Yoshizumi, M.; Uemura, T.; Uno, M.; Li, W.; Kang, M. J.; Yamagishi, M.; Okada, Y.; Miyazaki, E.; Nakazawa, Y.; Nakao, A.; Takimiya, K.; Takeya, J., Patternable Solution-Crystallized Organic Transistors with High Charge Carrier Mobility. *Advanced Materials* **2011**, *23* (14), 1626-1629.
4. Anthony, J. E., The Larger Acenes: Versatile Organic Semiconductors. *Angewandte Chemie International Edition* **2008**, *47* (3), 452-483.
5. Sundar, V. C.; Zaumseil, J.; Podzorov, V.; Menard, E.; Willett, R. L.; Someya, T.; Gershenson, M. E.; Rogers, J. A., Elastomeric Transistor Stamps: Reversible Probing of Charge Transport in Organic Crystals. *Science* **2004**, *303* (5664), 1644.
6. Takeya, J.; Yamagishi, M.; Tominari, Y.; Hirahara, R.; Nakazawa, Y.; Nishikawa, T.; Kawase, T.; Shimoda, T.; Ogawa, S., Very high-mobility organic single-crystal transistors with in-crystal conduction channels. *Applied Physics Letters* **2007**, *90* (10), 102120.
7. Méndez, H.; Heimel, G.; Opitz, A.; Sauer, K.; Barkowski, P.; Oehzelt, M.; Soeda, J.; Okamoto, T.; Takeya, J.; Arlin, J.-B.; Balandier, J.-Y.; Geerts, Y.; Koch, N.; Salzmann, I., Doping of Organic Semiconductors: Impact of Dopant Strength and Electronic Coupling. *Angewandte Chemie International Edition* **2013**, *52* (30), 7751-7755.
8. Sato, R.; Dogishi, M.; Higashino, T.; Kadoya, T.; Kawamoto, T.; Mori, T., Charge-Transfer Complexes of Benzo[thienobenzothiophene with Tetracyanoquinodimethane and the n-Channel Organic Field-Effect Transistors. *The Journal of Physical Chemistry C* **2017**, *121* (12), 6561-6568.
9. Tsutsumi, J. y.; Matsuoka, S.; Inoue, S.; Minemawari, H.; Yamada, T.; Hasegawa, T., N-type field-effect transistors based on layered crystalline donor-acceptor semiconductors with dialkylated benzo[thienobenzothiophenes as electron donors. *Journal of Materials Chemistry C* **2015**, *3* (9), 1976-1981.
10. Martin, R. L., Natural transition orbitals. *The Journal of Chemical Physics* **2003**, *118* (11), 4775-4777.
11. Frisch, M. J.; Trucks, G. W.; Schlegel, H. B.; Scuseria, G. E.; Robb, M. A.; Cheeseman, J. R.; Scalmani, G.; Barone, V.; Mennucci, B.; Petersson, G. A.; Nakatsuji, H.; Caricato, M.; Li, X.; Hratchian, H. P.; Izmaylov, A. F.; Bloino, J.; Zheng, G.; Sonnenberg, J. L.; Hada, M.; Ehara, M.; Toyota, K.; Fukuda, R.; Hasegawa, J.; Ishida, M.; Nakajima, T.; Honda, Y.; Kitao, O.; Nakai, H.; Vreven, T.; Montgomery Jr., J. A.; Peralta, J. E.; Ogliaro, F.; Bearpark, M. J.; Heyd, J.; Brothers, E. N.; Kudin, K. N.; Staroverov, V. N.; Kobayashi, R.; Normand, J.; Raghavachari, K.; Rendell, A. P.; Burant, J. C.; Iyengar, S. S.; Tomasi, J.; Cossi, M.; Rega, N.; Millam, N. J.; Klene, M.; Knox, J. E.; Cross, J. B.; Bakken, V.; Adamo, C.; Jaramillo, J.; Gomperts, R.; Stratmann, R. E.; Yazyev, O.; Austin, A. J.; Cammi, R.; Pomelli, C.; Ochterski, J. W.; Martin, R. L.; Morokuma, K.; Zakrzewski, V. G.; Voth, G. A.; Salvador, P.; Dannenberg, J. J.; Dapprich, S.; Daniels, A. D.; Farkas,

- Ö.; Foresman, J. B.; Ortiz, J. V.; Cioslowski, J.; Fox, D. J., Gaussian 09, Revision D. 01, Gaussian. Inc.: Wallingford, CT **2009**.
12. Rérat, M.; Maschio, L.; Kirtman, B.; Civalleri, B.; Dovesi, R., Computation of Second Harmonic Generation for Crystalline Urea and KDP. An ab Initio Approach through the Coupled Perturbed Hartree–Fock/Kohn–Sham Scheme. *Journal of Chemical Theory and Computation* **2016**, *12* (1), 107-113.
 13. Dovesi, R.; Erba, A.; Orlando, R.; Zicovich-Wilson, C. M.; Civalleri, B.; Maschio, L.; Rérat, M.; Casassa, S.; Baima, J.; Salustro, S.; Kirtman, B., Quantum-mechanical condensed matter simulations with CRYSTAL. *Wiley Interdisciplinary Reviews: Computational Molecular Science* **2018**, *8* (4), e1360.
 14. Zhu, L.; Yi, Y.; Fonari, A.; Corbin, N. S.; Coropceanu, V.; Brédas, J.-L., Electronic Properties of Mixed-Stack Organic Charge-Transfer Crystals. *The Journal of Physical Chemistry C* **2014**, *118* (26), 14150-14156.
 15. Dovesi, R.; Orlando, R.; Erba, A.; Zicovich-Wilson, C. M.; Civalleri, B.; Casassa, S.; Maschio, L.; Ferrabone, M.; De La Pierre, M.; D'Arco, P.; Noël, Y.; Causà, M.; Rérat, M.; Kirtman, B., CRYSTAL14: A program for the ab initio investigation of crystalline solids. *International Journal of Quantum Chemistry* **2014**, *114* (19), 1287-1317.
 16. Coropceanu, V.; Cornil, J.; da Silva Filho, D. A.; Olivier, Y.; Silbey, R.; Brédas, J.-L., Charge Transport in Organic Semiconductors. *Chemical Reviews* **2007**, *107* (4), 926-952.
 17. Coropceanu, V.; Li, H.; Winget, P.; Zhu, L.; Brédas, J.-L., Electronic-Structure Theory of Organic Semiconductors: Charge-Transport Parameters and Metal/Organic Interfaces. *Annual Review of Materials Research* **2013**, *43* (1), 63-87.
 18. Coropceanu, V.; Li, Y.; Yi, Y.; Zhu, L.; Brédas, J.-L., Intrinsic charge transport in single crystals of organic molecular semiconductors: A theoretical perspective. *MRS Bulletin* **2013**, *38* (1), 57-64.
 19. Koopmans, T., About the assignment of wave functions and eigenvalues to the individual electrons of an atom. *Physica* **1934**, *1* (1), 104-113.
 20. Zhu, L.; Yi, Y.; Li, Y.; Kim, E.-G.; Coropceanu, V.; Brédas, J.-L., Prediction of Remarkable Ambipolar Charge-Transport Characteristics in Organic Mixed-Stack Charge-Transfer Crystals. *Journal of the American Chemical Society* **2012**, *134* (4), 2340-2347.
 21. Meneghetti, M.; Pecile, C., Charge–transfer organic crystals: Molecular vibrations and spectroscopic effects of electron–molecular vibration coupling of the strong electron acceptor TCNQF4. *The Journal of Chemical Physics* **1986**, *84* (8), 4149-4162.
 22. Castagnetti, N.; Girlando, A.; Masino, M.; Rizzoli, C.; Rovira, C., Mixed Stack Organic Semiconductors: The Anomalous Case of the BTBT-TCNQFx Series. *Crystal Growth & Design* **2017**, *17* (12), 6255-6261.

CHAPTER-7

CONCLUSIONS AND OUTLOOK

Over the past decade, the field of organic electronics has witnessed a steady growth, with the development of newer material systems and significant improvements in operational efficiencies and the expansion of the organic light-emitting diode (OLED) market. Insights on device processes obtained from fundamental studies such as those presented here offer avenues to establish reliable connections between experimental observations and theoretical predictions. However, the absence of detailed control of the morphology of the active layers in the different types of organic electronic devices, represents a limiting step for further performance improvements. Therefore, in order to obtain a comprehensive picture of device operation, a better understanding of the factors linking the nature of packing and its impact on electronic and charge-transport characteristics are necessary.

With this broad aim in mind, in this Thesis, our investigations were focused on two types of π -electron donor (D)- π -electron acceptor (A) material combinations: (1) polymer/small-molecule acceptor combinations in pure and blend phases for organic photovoltaic (OPV) device applications; and (2) charge-transfer (CT) DA co-crystals for organic field-effect transistor (OFET) applications. We applied a combined approach based on molecular dynamics (MD) simulations and density functional theory (DFT) calculations for evaluating the local morphology of OPV materials and its impact on electronic properties; to analyze the effect of crystal packing on the charge-transport behavior in the CT co-crystals, we performed a series of DFT-based calculations to evaluate the band structures, densities of states, effective masses, and electronic

couplings. Below, we briefly summarize our main findings and discuss the outlook for future work for each of these categories of materials.

7.1. Organic Photovoltaics

In Chapter 3, we investigated the effect of solution temperature-dependent aggregation on the solid-state packing and electronic properties of two representative polymer donors, PBT4T-2OD and PffBT4T-2OD, in their pure phases. Using MD simulations, we explored the disaggregation of a perfectly packed cluster of each of these polymer chains in solution at 5 different temperatures. Based on the outputs of MD simulations, DFT calculations revealed the key role of fluorination in maintaining the coplanarity of PffBT4T-2OD chain. This facilitates a longer inter-chain interaction length and larger magnitude of electronic coupling among the PffBT4T-2OD chains, which contributes to the fact that they remain well-packed in solution. Therefore, when the solvent molecules evaporate during film formation, the binding interactions between the PffBT4T-2OD chains maintain their aggregated nature, leading to appropriate domain sizes and good crystallinity for the donor phase in the active layer. Such a morphology is favorable to efficient exciton dissociation and hole transport, which leads to high power-conversion efficiencies (PCEs).

In Chapter 4, we performed MD simulations on binary combinations of the PTFB-O polymer and two SMAs, ITIC-Th and IEIC-Th. The main results from this part are: (i) The similarity in intermolecular packing density and packing patterns points to the well-mixed nature among PTFB-O, ITIC-Th, and IEIC-Th, which explains the linear evolution of V_{oc} as a function of ITIC-Th concentration in the ternary blend of PTFB-O:ITIC-Th:IEIC-Th. (ii) Higher electronic couplings among the ITIC-Th acceptors account for higher electron-transfer rates, which is consistent with

the higher J_{sc} observed in the PTFB-O:ITIC-Th blend. (3) The difference in total energetic disorder of the CT states between the PTFB-O:ITIC-Th and PTFB-O:IEIC-Th blends is mainly induced by the difference in static disorder. (4) The difference in V_{oc} values is found to arise from the different extent of total energetic disorders of the CT states; the blend that exhibits lower total energetic disorder displays a higher V_{oc} .

The results we have obtained on OPV materials have given us more insight into the factors that influence the operation of an OPV device, which depends on the formation of an optimum active-layer morphology for efficient charge transport through the mixed and pure regions. While the results discussed in Chapter 3 focused on the pure phase of polymer donors, the impact on the mixed phase of the minor structural changes to the polymer backbone has also been investigated in a separate study to which we contributed (*Adv. Funct. Mater.*, **2018**, 28, 1705868, see Appendix A). We found that upon formation of a blend with the PC₇₁BM acceptor, the structural differences in the polymer backbones play a major role in determining the energetics of the CT interfacial electronic states. The main takeaway from our work is that the morphology control in blends such as those we have investigated can be enabled by optimization of three critical aspects: (i) temperature of the blend solution as well as casting temperature; (ii) selection of suitable solvent molecules; and (iii) position and extent of fluorination of the polymer backbones. Careful selection of these three parameters is crucial, as they allow the fine-tuning of all the intermolecular interactions that impact the formation of the final film morphology.

The main message from Chapter 4 is that the open-circuit voltage, V_{oc} , is higher in the case of the blend that shows the lowest static disorder, that is, the PTFB-O: IEIC-Th blend. We note that to

achieve higher device efficiencies, it is necessary to develop materials that exhibit reduced static and dynamic energetic disorders, and at the same time maintain optimum packing characteristics. In this regard, theoretical calculations can be of valuable help for material selection and understanding of the interactions within the blends. Such studies can point to good packing properties and high electronic couplings, characteristics that can lead to larger short-circuit current density values, J_{sc} , in the blends.

While our investigations on the OPV side mainly focused on the “local” morphology, we note that it is also important to evaluate their impact on the “global” morphology. However, the inherent limitations of all-atom MD simulations in terms of system sizes (up to about 10 nm x 10 nm x 10 nm) and time-scales (up to a few hundreds of nanoseconds) restrict their applicability for this purpose. To obtain a more reliable comparison with actual device morphology, coarse-grained (CG) MD simulations, which can address system sizes some three orders of magnitude larger and timescales reaching microseconds, need to be implemented.

A follow-up to Chapter 3 would be to rationalize in more detail the origin of the solution temperature-dependent aggregation properties in the PffBT4T-2OD polymer. Via an approach combining MD simulations, DFT calculations, and symmetry adapted perturbation theory (SAPT) calculations, this could be achieved by examining specific interactions among the molecular components. As for Chapter 4, extending the current MD simulations from binary blends to ternary blends represents the clear step forward. It is important indeed to understand the factors leading to the improvement in fill factor (FF) in the ternary blends *vs.* the corresponding binary blends. Recent reports in the literature indeed predict some of the highest PCEs for ternary blend devices.

We note that such an extension to our simulations would contribute greatly to the understanding of the specific features leading to the high efficiencies of the ternary blends. In addition, the derived binary and ternary morphologies can act as inputs for Kinetic Monte Carlo (KMC) calculations to simulate device relevant properties such as hole and electron mobilities, charge injection and extraction, and charge-recombination processes. CG simulations could also be useful here to directly compare the simulated morphologies to actual experimental device configurations. In the near future, more systematic relationships between morphology and device performance will in this way be more easily extracted from computational methodologies.

7.2. Organic CT Co-crystals

In this part of our Thesis, we mainly focused on analyzing the impact of packing on the electronic and charge-transport properties, with experimentally derived crystal structures used as inputs for the DFT calculations. In Chapter 5, we investigated the CT properties of a series of co-crystals based on the F₆TNAP acceptor and correlated them with the experimental results. The main conclusions of our work indicated that: (i) Large conduction bandwidths and small effective masses for electrons were obtained for all the co-crystals, which points to good electron-transport properties. (ii) Large valence bandwidths and small effective masses for holes were also obtained for the TP:F₆TNAP, BDT:F₆TNAP, and PY:F₆TNAP co-crystals, which suggests ambipolar charge-transport in these co-crystals. We recall that experimentally ambipolar transport properties were observed only for the PY:F₆TNAP and ANT:F₆TNAP co-crystals, and the charge-carrier SCLC mobilities are in excess of $10^{-1} \text{ cm}^2\text{V}^{-1}\text{s}^{-1}$ for at least four of the six co-crystals considered (TP:F₆TNAP, BTBT:F₆TNAP, PY:F₆TNAP and CBZ:F₆TNAP). (iii) The degrees of charge

transfer calculated using Mulliken charges also correlate well with the trends observed in the experimental results.

Chapter 6 primarily aimed at understanding the impact of sequential addition of alkyl chains on the donor and fluorine atoms on the acceptor, on the charge-transport characteristics of the BTBT- F_m TCNQ ($m=0, 2, 4$) and di- C_n BTBT- F_m TCNQ ($n=8, 12; m=0, 4$) series of co-crystals. As in the case of F_6 TNAP co-crystals, we find that all the co-crystals considered here exhibit good electron-transport characteristics. However, ambipolar transport is predicted only for the BTBT- F_m TCNQ ($m=0, 2, 4$) series of co-crystals. We note that the electron-hole asymmetry found in these systems arises mainly from the presence of multiple charge-transport pathways that contribute to the overall superexchange couplings for holes and electrons along the stacks. The TDDFT calculations on the lowest energy CT excitations correlate well with the experimental observations. Again, the degree of charge transfer calculated from Mulliken charges were consistent with the available experimental data.

While the results presented in this Thesis provide a detailed characterization of the electronic structure of these co-crystals, which are found to be in line with the experimental data, there are features that need further clarification. For instance, although the impact of Hartree-Fock exchange on the electron-vibration couplings has been previously investigated, the corresponding impact of range-separated functionals not been fully explored. Another aspect of interest is to evaluate the effect of hydrogen-bond interactions and halogen interactions on the packing motifs of the co-crystals. Also, recent studies indicate that some of the donor-acceptor co-crystals display ferroelectric properties. A theoretical understanding of the nature and extent of these magnetic

properties as well as of the non-linear optical properties is crucial to investigate their potential applications as, for instance, electrically conducting hydrogels, CT sensitizers for photovoltaics, and magnetically controllable ferroelectric materials.

Extensions of the work presented in Chapters 5 and 6 would include a broader characterization of the structure-property relationships in these co-crystals, including aspects like electron-phonon coupling and impact of disorder. In this regard, it is important to evaluate the impact of electron-phonon couplings beyond the Γ point. Also, the identification of the intramolecular and intermolecular vibrational modes corresponding to CT excitations is of interest. We note that the optical properties of these co-crystals have not been very well characterized yet. While the calculations so far have been largely limited to simple DA complexes, it would be interesting to extend the current approaches to cluster-level calculations at the level of accurate methodologies such as the GW approximations in combination with Bethe-Salpeter equations. A comprehensive description of all these features would definitely help form a better understanding of the structure-property relationships and eventually contribute to improve the device performance in OFET devices based on such co-crystals.

APPENDIX A

LIST OF PUBLICATIONS

- [1]. Wang, T.; Chen, X.; **Ashokan, A.**; Zheng, Z; Ravva, M. K.; Brédas, J.-L. “Bulk Heterojunction Solar cells: Impact of minor structural modification to the polymer backbone on the polymer-fullerene mixing and packing on the fullerene-fullerene connecting network”. *Adv. Funct. Mater.*, 2018, 28(14), 1705868.
- [2]. **Ashokan, A.**; Wang, T.; Ravva, M.K.; Brédas, J.-L. “Impact of solution temperature-dependent aggregation on the solid-state packing and electronic properties of polymers for organic photovoltaics”. *J. Mater. Chem. C*, 2018, 6, 13162-13170.
- [3]. Issac, R; **Ashokan, A.**; Coropceanu, V.; McNeil, L.E. “Organic charge-transfer compounds: complex interactions at the nanoscale”. *Proceedings of SPIE*, 2019, 10926, *Quantum Sensing and Nano Electronics and Photonics XVI*; 109262C.
- [4]. Dasari, R.R; Wang, X; Wiscons, R.A.; Haneef, H.F.; **Ashokan, A.**; Zhang, Y; Fonari, M.S.; Barlow, S.; Coropceanu, V.; Timofeeva, T.V.; Jurchescu, O.D.; Brédas, J.-L.; Matzger, A.J.; Marder, S.R “Charge-Transport Properties of F6TNAP-based Charge-Transfer Co-crystals”. *Adv. Funct. Mater.* 2019, 1904858
- [5]. **Ashokan, A.**; Hanson, C.; Coropceanu, V.; Brédas, J.-L. “Electronic, vibrational and charge-transport properties of di-C_nBTBT-F_mTCNQ co-crystals: The impact of alkyl chains and fluorination”
Ready for Submission
- [6]. **Ashokan, A.**; Wang, T.; Coropceanu, V; Brédas, J.-L. “Bulk-Heterojunction solar cells: Understanding the intermolecular packing and electronic properties of polymer-SMA blends”
Ready for Submission